

Application of Materials Characterization, Efficacy Testing, and Modelling Methods on Copper Cold
Spray Coatings for Optimized Antimicrobial Properties

A Dissertation

Submitted to the Faculty

of the

WORCESTER POLYTECHNIC INSTITUTE

in fulfillment of the requirement of

Degree of Doctor of Philosophy

in

Materials Science and Engineering

by

Kristin Sundberg

May 2019

Approved by:

Professor Danielle L. Cote, Advisor

and

Professor Richard D. Sisson, Department Head Material Engineering



Application of Materials Characterization, Efficacy Testing, and Modelling Methods on Copper Cold Spray Coatings for Optimized Antimicrobial Properties

Kristin Sundberg

April 08, 2019

Abstract

The Copper Development Association (CDA) has identified over 450 copper alloys registered with the U.S. Environmental Protection Agency (EPA) as antimicrobial. With growing antibiotic resistance, there is a need for copper coatings with increased antimicrobial capability. Cold spray is a high velocity, high deposition rate process that forms dense coatings with little to no oxides or inclusions. It is possible that this process contributes to the increased antimicrobial capability of copper cold spray coatings as compared to other additive processes.

The focus of this effort is to understand the effects of powder production and cold spray process parameters on copper cold spray coatings in order to optimize antimicrobial properties. Specifically, this work looks at the differences in conventional and nanomaterial copper cold spray coatings. Materials characterization and test methods show differences in adhesion, microstructure, corrosion, mechanical properties, and surface topography. Materials data is compared against Abaqus FEA software model outputs, and antimicrobial efficacy test data, based on the EPA approved procedure, is used to support materials observations and modelling outputs.

Executive Summary

Optimizing the Cold Spray Process for Antimicrobial Coatings

Recently in the cold spray community, more emphasis has been placed on through process modelling and the effects of powder quality on product outputs. Powder production, material type, size, storage, and distribution method are all considered factors affecting consolidated material properties. Similar considerations can be applied when looking at the optimization of copper cold spray coatings for antimicrobial applications.

This thesis focuses on the effects of powder in relation to end material properties, where gas atomized conventional copper powder is compared to spray dried nano-agglomerate copper powder. The nano-agglomerates are comprised of pure Cu nanoparticles encapsulated in a pure Cu binder. Precursor comparison of these consolidated powders is described in the paper “Effectiveness of Nanomaterial Copper Cold Spray Surfaces on Inactivation of Influenza A Virus”, included in the ‘supplemental paper A’ section. That paper provides a baseline for antimicrobial properties of nanomaterial copper coatings, showing their increased effectiveness in the contact-killing of Influenza A Virus as compared to conventional copper.

The second paper in the thesis, “Modeling Copper Cold Spray Single-Particle Impact for Optimized Antimicrobial Coatings”, looks at modelling of the powder type and cold spray parameters, including temperature, pressure, and spray velocity, on particle impact and post-impact geometry. This can be used as a tool to understand why nanomaterial copper performs better than conventional copper in relation to the initial powder and spray parameters. In future, improved models may be used to predict the best initial parameters for optimized antimicrobial properties of copper cold spray coatings.

Material Characterization- A Missing Link in Understanding Copper Kill-Mechanism

Beyond the CDA’s determination that materials with 60% copper or greater can be considered antimicrobial, the CDA has not formally linked other material properties as affecting copper’s antimicrobial capability. A paper included in the ‘supplemental paper B’ section titled, “Anti-bacterial and anti-viral performance of kinetically deposited copper surfaces”, compares differences in end material properties between cold spray and other additive methods, showing greater antimicrobial efficiency in cold spray coatings. But more work is needed to look beyond the efficacy test data and into the material differences between conventional and nanomaterial Cu cold spray to understand why the latter performs better in the contact-killing of Influenza A Virus.

Factors like surface roughness and microstructure are explored in the first paper, “The Effect of Nano-Scale Surface Roughness on Copper Cold Spray Inactivation of Influenza A Virus” and third paper, “Microstructural Characterization of Conventional and Nanomaterial Copper Cold Spray Coatings” of the thesis, respectively.

Antimicrobial Efficacy of Cu and Cu Ion Release

Researchers in the biology field have been able to isolate copper's antimicrobial properties to its ability to release copper ions to microbes via surface contact. There is still heavy debate as to the exact copper kill-mechanism once the ions are released to the microbe with much of the discussion around Cu-uptake and its intra-cellular effects. There are also discrepancies in efficacy data depending on the test method, microbe type, and material used. As there are many bio-factors affecting copper antimicrobial effectiveness, it is important to perform more efficacy tests under different conditions with various microbes and substrates to add as many datapoints as possible to the knowledge bank. It is also important to fully understand how the Cu ions are being released from the metal into the environment. To better understand Cu ion release, corrosion differences between nanomaterial and conventional Cu cold spray are studied in the forth paper of the thesis titled, "The Effect of Corrosion on Conventional and Nanomaterial Copper Cold Spray Surfaces for Antimicrobial Applications".

Contents

| | |
|--|----|
| Abstract..... | 1 |
| Executive Summary..... | 2 |
| 1. Introduction..... | 5 |
| 1.1 Project Need | 5 |
| 1.2 Project Scope and Approach..... | 5 |
| 2. Background | 6 |
| 2.1 Review of Theory Behind Copper’s Antimicrobial Properties..... | 6 |
| 2.1.1 Copper Uptake + Utilization by Microorganisms..... | 6 |
| 2.1.2 Principles Governing Metal reactivity in Living Cells..... | 7 |
| 2.1.2.1 Donor Atom Selectivity..... | 7 |
| 2.1.2.1.1 Determining Favorability of Cu Oxidation State..... | 8 |
| 2.1.2.1.2 Relationship between Donor Atom Selectivity and Copper Uptake..... | 10 |
| 2.1.2.2 Reduction Potential..... | 11 |
| 2.1.2.3 Speciation..... | 12 |
| 2.1.3 Copper Toxicity and Tolerance by Microorganisms..... | 13 |
| 2.1.4 Contact-Killing Mechanism..... | 15 |
| 2.1.5 Relationship between Antimicrobial and Material Properties..... | 16 |
| 2.1.6 References..... | 17 |
| 3. Paper #1: <i>The Effect of Nano-Scale Surface Roughness on Copper Cold Spray Inactivation of Influenza A Virus</i> | 19 |
| 4. Paper #2: <i>Modeling Copper Cold Spray Single-Particle Impact for Optimized Antimicrobial Coatings</i> | 30 |
| 5. Paper #3: <i>Microstructural Characterization of Conventional and Nanomaterial Copper Cold Spray Coatings</i> | 45 |
| 6. Paper #4: <i>The Effect of Corrosion on Conventional and Nanomaterial Copper Cold Spray Surfaces for Antimicrobial Applications</i> | 61 |
| 7. Conclusion..... | 85 |
| Supplemental Paper A: <i>Effectiveness of Nanomaterial Copper Cold Spray Surfaces on Inactivation of Influenza A Virus</i> | 86 |
| Supplemental Paper B: <i>Anti-bacterial and anti-viral performance of kinetically deposited copper surfaces</i> | 91 |

1. Introduction

1.1 Project Need

In 2006, there were ~720,000 healthcare associated infections, costing over \$125 billion and causing over 74,000 deaths in the U.S. [1,4]. With the growing resistance of microbes to antibiotics, it is important now more than ever to look at alternative methods for reduction of the harmful growth of microbes and spread of disease. The Copper Development Association lists 450+ copper alloys registered with the U.S. Environmental Protection Agency as antimicrobial [3]. There is a need to continue to optimize copper surfaces through the use of novel powder in the cold spray system. The cold spray process, Figure 1, is a high velocity, high deposition rate process that forms dense coatings with little to no oxides and inclusions.

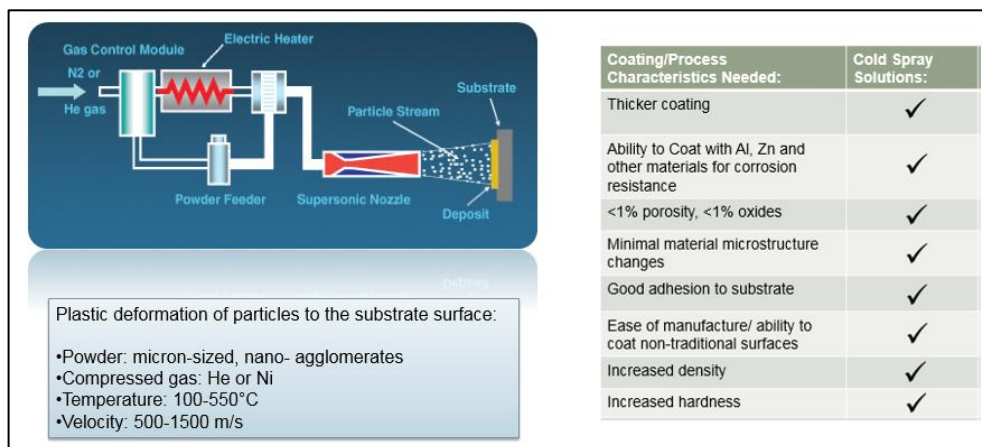


Figure 1. The Cold Spray Process

1.2 Project Scope

The goal is to decrease microbe survivability through the use of optimized Cu cold spray coatings. This thesis scope looks at the differences in material properties between nanomaterial and conventional Cu cold spray coatings, in order to better understand why nanomaterial Cu performs better than conventional Cu in the contact-killing of Influenza A Virus.

The thesis scope can be further explored through the bio-material interface, seen in Figure 2, where areas of interest include: 1) the microbe, 2) the environment, 3) the material surface, 4) on top of the material, and 5) inside the material.

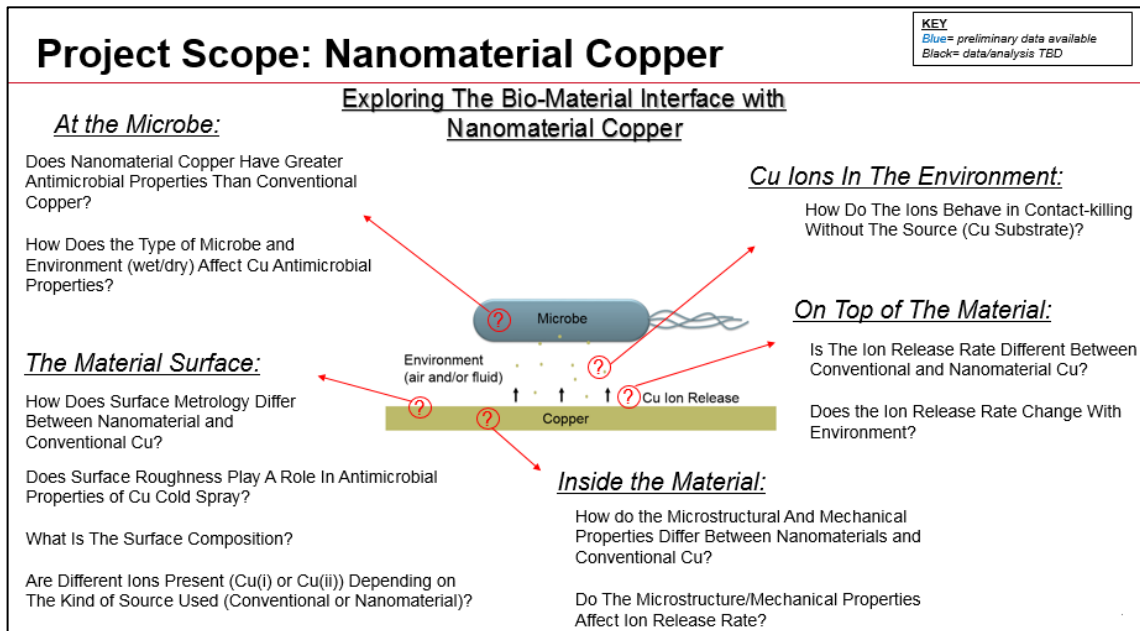


Figure 2. Thesis Scope- looking at the bio-material interface in relation to nanomaterial Cu

The questions detailed in Figure 2 can be answered using a 3-pronged approach of 1) Material Characterization, 2) Antimicrobial Efficacy Testing, 3) and Modelling, with results broken into four papers included in sections 3-6.

2. Background

2.1 Review of Theory Behind Copper's Antimicrobial Properties

There are many factors affecting Cu Antimicrobial Properties across the chemistry, biology, and material science fields. There is a need to understand Cu uptake and utilization, metal reactivity, and Cu tolerance in microorganisms to see the full scope of the Cu contact-killing mechanism.

2.1.1 Copper Uptake + Utilization by Microorganisms

Microorganisms need metals, including copper, to maintain proper physiology. Understanding how microorganisms find, bring into the cell, and use copper ions is crucial to understanding copper kill mechanisms. Since there are many different pathways for uptake and utilization and even more are being discovered every day, it is most effective to illustrate the need to understand these mechanisms with an example in Figure 3. Methanotrophs are gram-negative bacteria that use methane as a carbon energy source, but Methanotrophs can only make the energy they need if they have a certain enzyme, methane monooxygenase (MMO). MMO can only be turned on by copper.

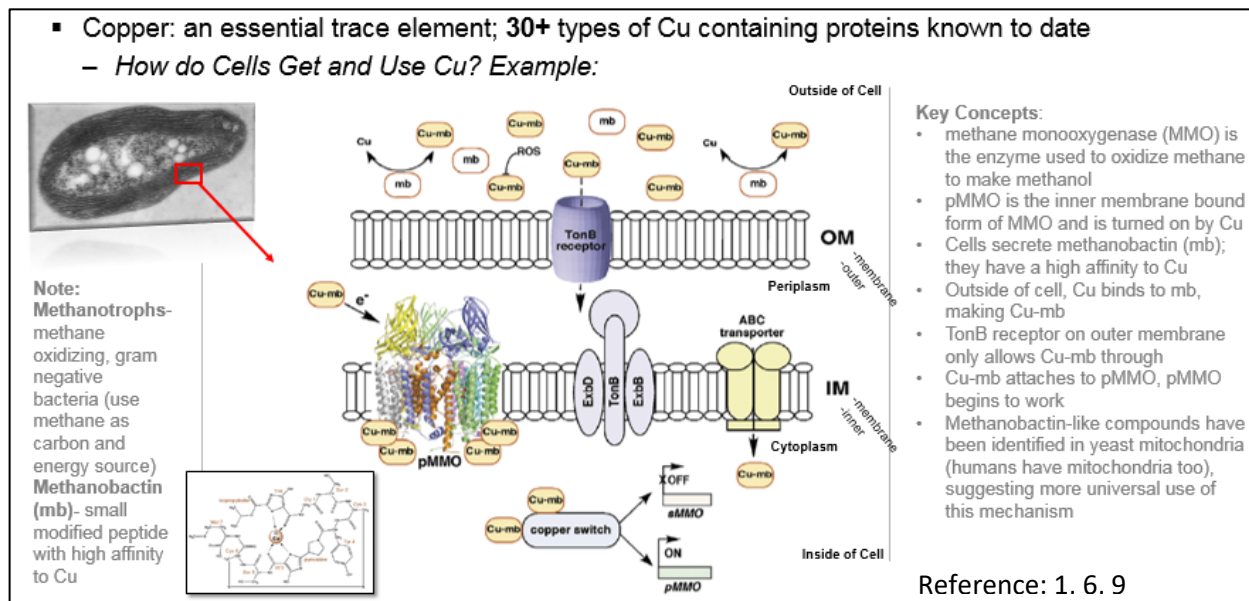


Figure 3. Example copper uptake and utilization mechanisms using methanobactin described.

Methanobactin (mb) reside in Methanotrophs and are peptides modified to have a high affinity for copper. In order for the methanotroph cell to capture the copper ions in its environment it uses these methanobactin to bond to the ions, making Cu-mb. The TonB Receptor, embedded in the outer cell membrane, is coded to accept mb peptides allowing the Cu-mb to pass through the outer membrane into the periplasm (space between outer and inner cell membranes). The Cu-mb then attaches to the inner membrane receptor, pMMO, switching it on to MMO allowing the cell to oxidize the methane to methanol for energy. Depending on the microorganism and environment, the kind of uptake and utilization mechanisms may change. However, similar methanobactin compounds have been identified in the mitochondria of yeast suggesting that this mechanism may be more widely applicable to other organisms, including humans.^{1, 6, 9}

Understanding uptake mechanisms give scientists a better foundation to understand how the copper ions get into the cell and if the copper killing mechanism starts prior to entering the cell. Following copper utilization may provide clues to where in the cell copper ions are first attacking and if there are secondary and tertiary effects that may cause additional damage to the cell based on copper ion location.

2.1.2 Principles Governing Metal reactivity in Living Cells

There are three principles governing metal reactivity in living cells: 1) donor atom selectivity, 2) reduction potential, and 3) speciation.

2.1.2.1 Donor Atom Selectivity

Donor atom selectivity looks at the coordination chemistry of metals. A subset of this field is Ligand Field Theory, which looks at how different transition metal electron arrangements affect the metal's affinity to bond with ligands. An example of a ligand would be mb, from the above section. A copper ion may be more or less likely to bond to mb to form Cu-mb than another metal ions depending on its electron configuration. Fortunately, there is a universal order of preference for divalent transition metals, called the Irving-Williams Series, shown in Figure 4. Copper happens to be at the top of this series. The right hand side of Figure 4 provides graphs from a study by P. Varadwaj that proves out this theory.²³

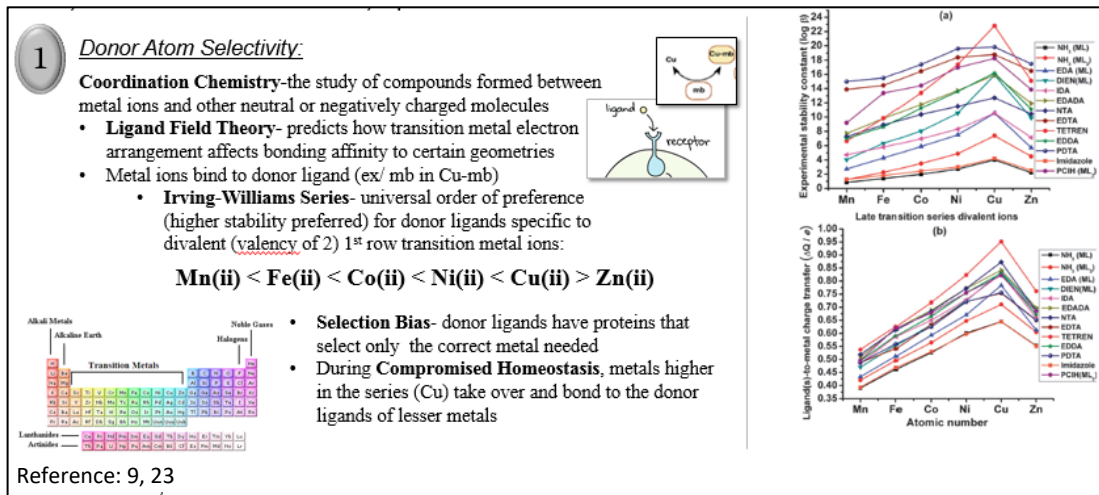


Figure 4. Donor Atom Selectivity described. This is one principle governing metal reactivity in living cells.

The y-axis of the graphs are the stability constants symbolically represented by logB (top) and the ligand-to-metal charge transfer values (bottom). The x-axis are the metals tested (top) and the atomic number (bottom). Each line on the graph is representative of a 'ligand' that the metal was tested against. The experimental logB values were taken from the NIST database and the ligand-to-metal charge values were calculated using Density Functional Theory. Both graphs show Cu as having the highest values. The metal with the higher preference has a higher stability and is the metal that will be most likely to fill donor ligand sites when cellular homeostasis is compromised. Compromised homeostasis can degrade the cellular system in such a way that it can no longer code for certain metals in its ligands or select for specific metal-ligand complex uptake at its membrane receptors. This is relevant to copper kill mechanisms because an influx in copper ions in the cell may lead to the damaging of structures within the cell.^{9,23}

2.1.2.1.1 Determining Favorability of Cu Oxidation State

There are two kinds of copper, Cu(i) and Cu(ii), having one and two valence electrons respectively. Figure 5 details the full electron configuration for copper. The stability of Cu(i) and Cu(ii) is dependent on their oxidation state; even though Cu(i) has completely filled orbitals it is not always more stable than Cu(ii). Sometimes the system favors an oxidation state for Cu(i), as is typical in non-aqueous environments, and sometimes it favors an oxidation state for Cu(ii), as is typical in aqueous environments.

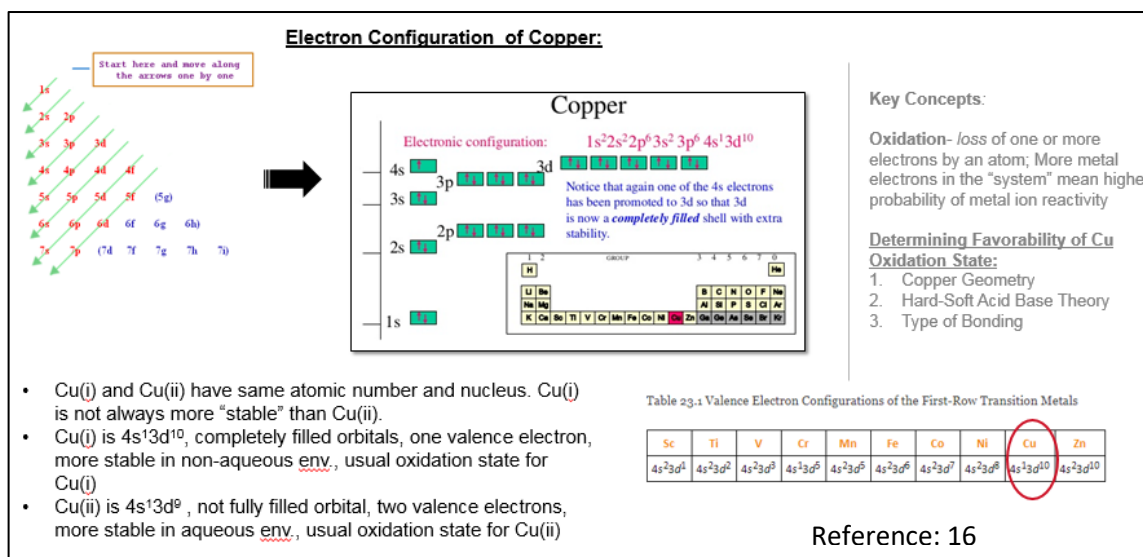


Figure 5. Transition Metals: Chemistry of Copper. The relationship between Cu(i) and Cu(ii) electron configuration and oxidation state.

Knowing the copper oxidation state matters for Cu kill mechanisms because knowing whether Cu(i) or Cu(ii) is dominant or more stable provides an indicator for which ion is being linked to the ligand and taken up by the cell. It is possible that different mechanisms may be used for different ions; isolating these specific mechanisms may provide clues for if the copper kill mechanisms differ between Cu(i) and Cu(ii) and if the environment (wet or dry) affects copper's kill rate due to the differences in ions present.¹⁶

It is not a guarantee that microorganisms will take up the more stable copper ion, but the environment will behave in such a way as to increase stability of the system, thereby making the concentration of a specific copper ion higher than the other and increasing its probability of uptake. Conversely, microorganisms may be able to code for the uptake of the lesser ion or may take on the dominant ion and transition it to the less stable ion within the cell. There are many options for ion uptake and manipulation, this is just one factor to consider when looking at the properties of antimicrobial copper. The favorability of copper oxidation state can be broken into three categories including geometry, bonding, and hard-soft acid base theory.

Cu(i) prefers a tetrahedral geometry and Cu(ii) prefers a distorted octahedral, see Figure 6 for images. For the tetrahedral geometry Cu(i) is more stable than Cu(ii) largely due to its electron configuration and ability to excite an electron from the 's' to the 'p' orbital forming a blended sp^3 orbital. For the octahedral geometry Cu(ii) is more stable than Cu(i) and it distorts to reduce energy further forming either an elongated or compressed octahedral.^{16, 17}

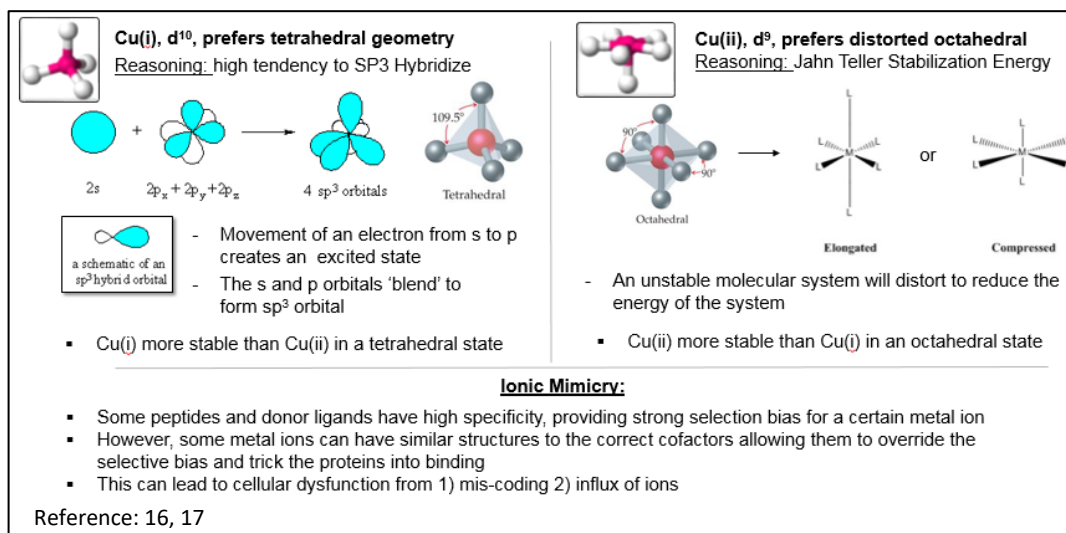


Figure 6. Determining favorability of copper oxidation state by looking at the geometry of Cu(i) (left) and Cu(ii) (right). Ionic Mimicry (bottom) is discussed as an example of how copper geometry may affect copper kill mechanisms.

Geometry affects the kind of bonding of copper ions to ligands. It also affects the ability for copper to bond to non-copper coded ligand donors. If those donors are looking for a geometry different from copper then it may be tougher for copper ions to bond. If the ligand codes for a geometry similar to copper but not for copper itself, it is possible that the copper ion may still bond to the ligand in place of another similar ion, also known as ion mimicry. This is one way that an influx of copper may be able to trick the cell and get into through the cell wall.⁹

Cu(i) favors back-bonding and Cu(ii) does not. An explanation of back-bonding, given in Figure 7, shows that it is a two-step process. The first step is that the donor ligand supplies electrons to the vacant d-orbital. In the second step the metal 'backshares' its pi bond with the ligand because the metal is trying to compensate for the increased electron density from step one. Step one is best characterized as sigma bonding and is much stronger than that the pi bonds seen in step two.^{18, 23}

- Cu(i), favors back-bonding to ligand
- Back-bonding:
 - The ligand donates sigma electrons into a vacant metal d-orbital
 - The metal must compensate for the increased electron density
 - The filled metal d-orbital shares with the pi* orbital on the ligand (pi- backbonding)

Step 1:

σ bond:

Step 2:

π backbond:

- Cu(ii) has a low degree of back donation and does not favor back-bonding
- Tougher for Cu(ii) to form pi acceptor ligand type bonds
- In general, pi bonds are weaker than sigma bonds
- This can be attributed to a greater amount of overlap with sigma bonds than that of pi bonds

Reference: 18, 23

Reference: 26, 30, 34

Figure 7. Determining favorability of copper oxidation state by looking at the bonding state of copper with relation to both Cu(i) (left) and Cu(ii) (right).

Since it is tougher for Cu(ii) to form pi acceptor ligand type bonds, it follows that they would be less likely to bond to ligands preferring this bonding structure. Similar to ion mimicry, if there is a preferred bonding type on a ligand that is not coded for copper, the copper ions may still be able to bond to that site if it has the same preferred bonding structure.

Hard-Soft Acid Base (HSAB) Theory looks at the metal's affinity towards donor ligands from a pH perspective. The idea being that hard acids associate with hard bases, and soft acids associate with soft bases. Figure 8 provides a diagram showing the differences between hard and soft acids, as well as a chart detailing bases and their structures.

Key Concepts:

Electronegativity- atom's tendency to attract electrons

Polarizability- an electron's tendency to be distorted around an atom (usually the electrons distort towards a more electronegative atom)

- HSAB Theory- predicts affinity of metal ions towards donor ligands
 - Hard acids associate with hard bases and soft acids associate with soft bases

| Hard Acid | | Soft Acid |
|-----------|-----------------|-----------|
| Small | Ionic radius | Large |
| High | Oxidation state | Low |
| Weak | Polarizability | Strong |
| Ionic | Acid-base bond | Covalent |

- Acids and bases that have an intermediate character between hard and soft are classified as borderline

| | Hard | Borderline | Soft |
|--------------|--|--|---|
| Acids | Na ⁺ , K ⁺ , Mg ²⁺ , Ca ²⁺ , Cr ³⁺ , Al ³⁺ , Ga ³⁺ , Co ³⁺ , Fe ³⁺ | Cu ²⁺ , Zn ²⁺ , Pb ²⁺ , Bi ³⁺ , Ni ²⁺ , Co ²⁺ , Fe ²⁺ | Cu ⁺ , Au ⁺ , Ag ⁺ , Hg ²⁺ , Hg ⁺ , Cd ²⁺ |
| Bases | Carbonate Sulphate Carboxylates R-OH Alcohols Phosphate R-O-R Ethers Also: H ₂ O, OH ⁻ , NH ₃ , hydrazine | Aniline Pyridine Nitrite R-N=N=N-R Azides Also: N ₂ | Phenyl groups R-SH Thiols R-S-R Thioethers ≡N ⁻ Cyanide Also: H ₂ S, H ₂ ⁻ |

Oxidation state

Ionic or atomic radius

Electronegativity (bases)

Polarizability

Mostly ionic bonding Mostly covalent bonding

Reference: 2, 9

Figure 8. Determining favorability of copper oxidation state by looking at Hard-Soft Acid Base Theory.

Hard acids and bases tend to have higher oxidation states, smaller ionic radiuses, weaker polarizability, and higher electronegativity. Cu(i) is a soft acid and Cu(ii) is in the borderline category, which means Cu(i) is more likely to bond to a soft base and Cu(ii) to a borderline base [2,9].

Metal ion toxicity is proportional to affinity. If more ions make it into the cell, there is a higher chance of cellular damage. In order to make it into the cell in higher quantities, the ligand-donor needs to be receptive and copper ions needs to want to bond to it. For example, a ligand that has a sulfhydryl group will be more likely to attract a Cu(i) ion than another ion because the sulfhydryl group is a soft base. So by increasing Cu(i) affinity, the ligand is directly increasing copper toxicity.

2.1.2.1.2 Relationship between Donor Atom Selectivity and Copper Uptake

In the prior section, methanobactin (mb) is introduced as a ligand donor in methanotrophs with a high affinity to bond to copper. Mb can be used as an example again here to describe how understanding the factors affecting oxidation state can help in determining what type of copper ion is present at the environment-microbe interface. The geometry of mb can be found in Figure 9 as a pyramid-like geometry. It's more of a distorted tetrahedral with the copper ion resting at the base. While the tetrahedral structure favors Cu(i), the structure contains both sulfur and nitrogen complexes which favor Cu(i) and Cu(ii), respectively. Research has shown through x-ray photoelectron spectroscopy that the favored ion in this case is in Cu(i)²². It is suspected that geometry plays a larger role than HSAB for this specific example, but additional research is needed to confirm the hypothesis.

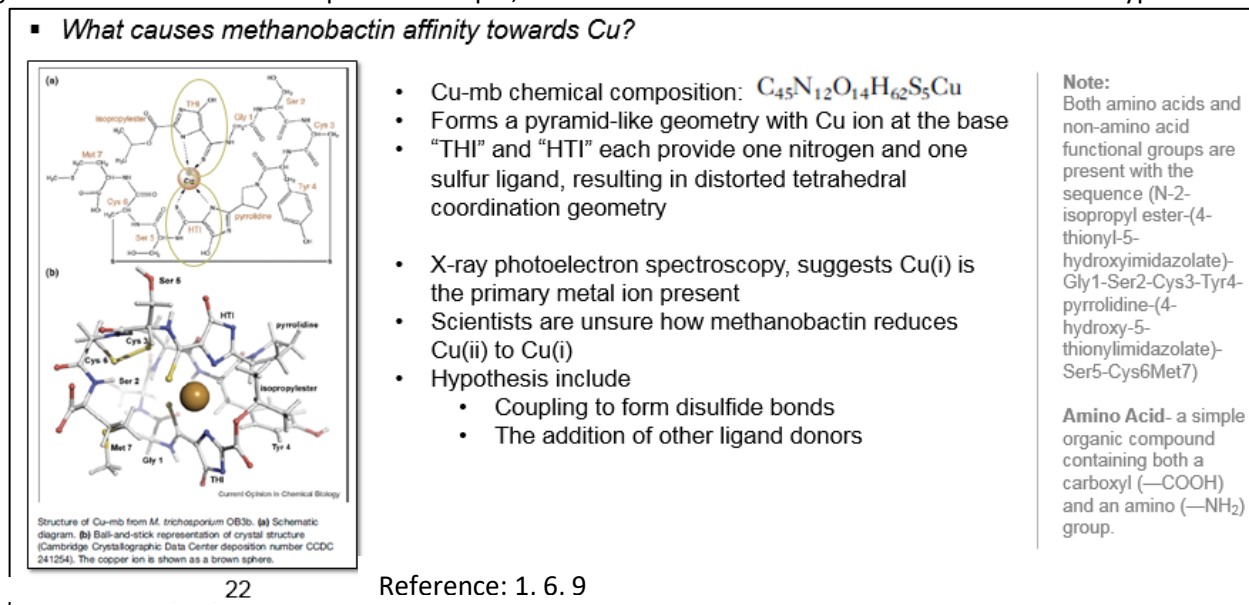


Figure 9. An example of the relationship between donor atom selectivity and copper uptake. Specifically looking at methanobactin affinity towards copper.

Methanotrophs tend to live in soils and areas with high methane, both Cu(i) and Cu(ii) would be present in this environment. Depending on if the environment is wet/dry and if the pH is acidic, a different copper ion will be favored by the system. Scientists are still trying to figure out how Cu(ii) is transitioned to Cu(i) by mb. It is hypothesized that coupling of disulfide bonds and the addition of other donor ligands may play a role in this conversion process, but more research is needed to confirm. Mb is just one example of how donor atom selectivity and specifically oxidation state play a key role in copper ion metal uptake and increased reactivity/toxicity within the cell.

2.1.2.2 Reduction Potential

Another principle governing metal ion reactivity is reduction potential. Reduction potential looks at a metal's tendency to acquire electrons; metals having higher standard electrode potentials have a higher tendency to acquire electrons. Redox-active metals can be used for physiological functions as the 'key' to unlock enzymes, otherwise known as catalytic cofactors. An example of this would be Cu-mb from the prior section. Where Cu is the metal ion that binds to the ligand donor mb. Cu-mb then gets brought into the body and the copper is used as a cofactor to turn on MMO which allows for the production of methanol.

Redox-active metals can also be toxic, the reasons for this will be discussed in the following section. It is shown that there is a direct correlation between standard electron potential and a metal's toxicity^{9, 16}. Copper is about mid-range on standard electrode potential at, +0.34. Other metals higher and lower in standard electrode potential are shown in Figure 10. Higher metals that have antimicrobial properties in use today include silver at, +0.80, and gold at, +1.52. While gold and silver are more toxic, availability and cost make the use of these metals for antimicrobial properties less common.

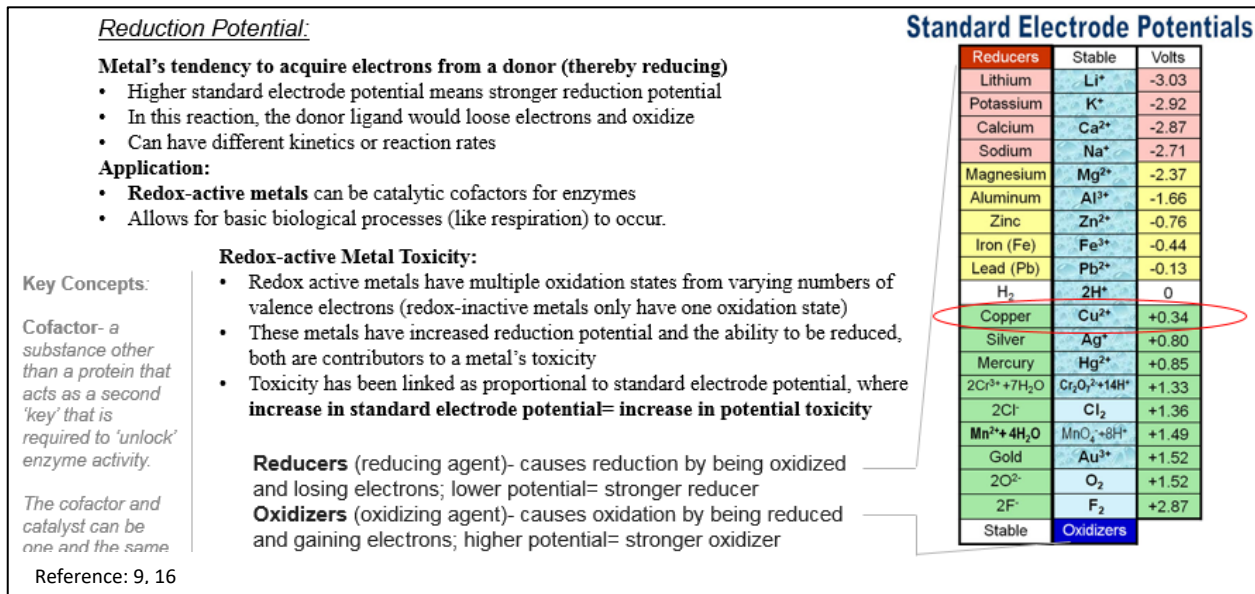


Figure 10. Reduction potential described. This is one principle governing metal reactivity in living cells.

2.1.2.3 Speciation

The last principle governing metal ion reactivity is speciation. Speciation looks at the different species of the metal that exist. Examples of species that exist for copper would include CuO, Cu(I), and Cu(II). Other species of copper may exist in different structures, as the metal will bind to different parts of the cell, all having varying compositions, geometries, and binding preferences, leading to a wide range of Cu-complexes. Factors affecting speciation may include pH, ionic strength, and temperature. Two examples of this are provided in Figure 11, which looks at gram-negative bacteria and zeolite.

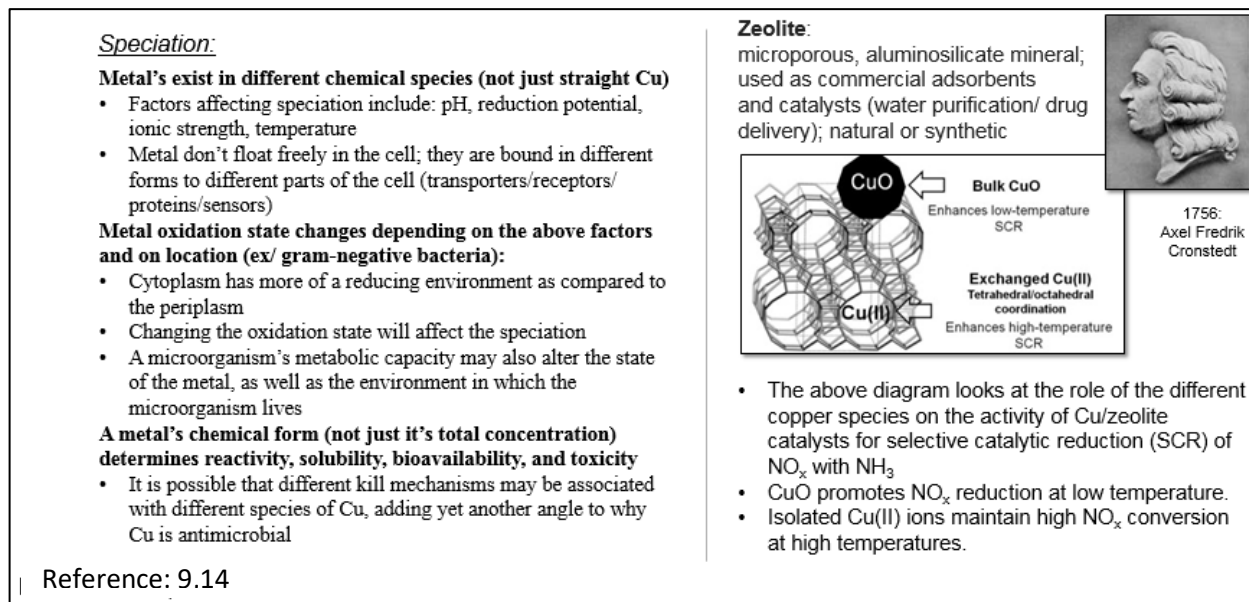


Figure 11. Speciation described. This is one principle governing metal reactivity in living cells.

In gram-negative bacteria, the cytoplasm (space inside cell) of the cell is more of a reducing environment than the periplasm (space between outer and inner membrane). Having a cytoplasm with more of a reducing environment allows the cell the ability to change the species of copper. This may be useful in reducing copper's toxicity or could have the opposite effect depending on environmental factors and if the cell is in homeostasis.⁹ Zeolite provides an example of how environmental change, specifically temperature, may have differing effects of species of copper. Zeolite is an aluminosilicate mineral containing NO_x complexes. When CuO bonds to NO_x it enhances the reduction

of NO_x at low temperatures. But if Cu(ii) were to bond to this same complex, it would only support reduction of NO_x at high temperatures.¹⁴ Temperature, pH, and other factors may serve as catalysts in eliciting toxic responses from various copper species.

2.1.3 Copper Toxicity and Tolerance by Microorganisms

Redox potential is a vital principle in cell physiology, but may also be toxic to the cell if the range grows too high or there is an influx of production of damaging species, as seen in Figure 12.

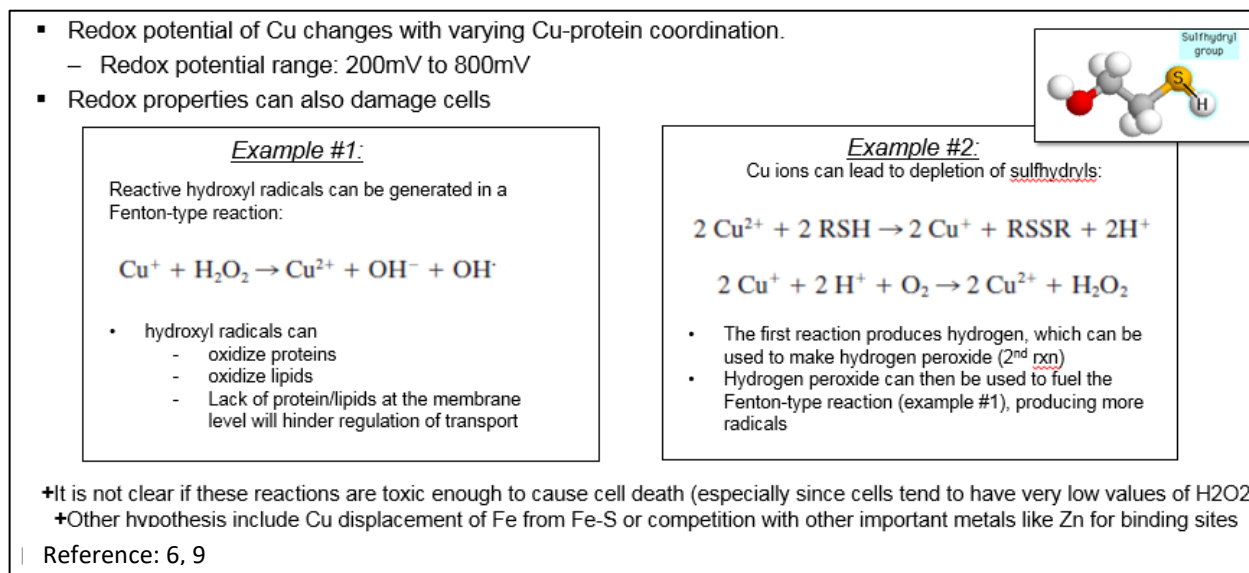


Figure 12. The Toxicity of Copper in Microorganisms

Acceptable Cu-protein redox potential is 200-800mV, if the voltage were to exceed this range it may damage the cell⁹. Additionally, the development of Hydroxyl radicals and the depletion of sulfhydryls may oxidize important proteins, lipids, and other building blocks that are needed by the cell. The formation of hydroxyl radicals is also known as the Fenton type reaction, where Cu(i) reacts with hydrogen peroxide to form hydroxyl radicals. The depletion of sulfhydryls occurs when Cu(ii) reacts with sulfhydryls breaking them up, with one of the byproducts being hydrogen. The hydrogen can then go into a second reaction with Cu(i) resulting in formation of hydrogen peroxide, which may be used to fuel more of the Fenton-type reactions. While this cycle is a promising argument for toxicity, there is skepticism amongst scientist that it is enough to cause cell death, especially since cells have many built-in mechanisms to reduce and maintain low levels of hydrogen peroxide.⁶

Many microorganisms have built-in copper tolerance mechanisms, some of which are detailed in Figure 13. Protective barriers on the outside of the cell exists to trap harmful metal ions, known as extracellular sequestration. This can be seen in the form of loose or anchored polymers that trap or encapsulate the toxic ions. A similar process may occur inside the cell, termed intracellular sequestration.

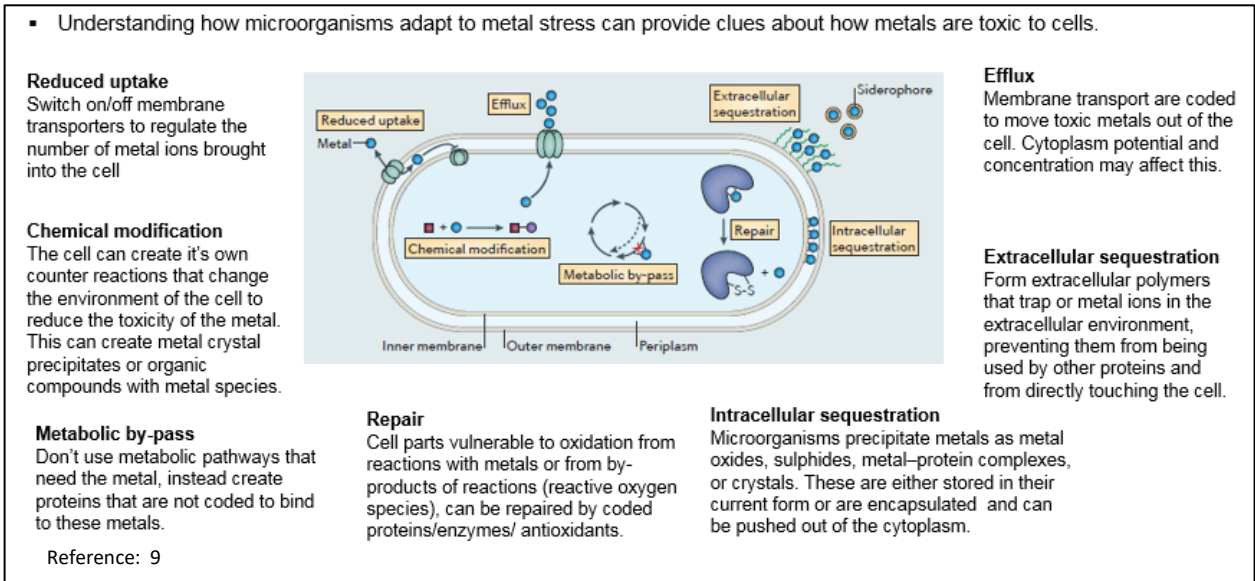


Figure 13. The Tolerance of Microorganisms to Antimicrobial Properties of Copper

At the cell membrane level, there is the ability to reduce uptake by turning membrane transporters off or having membrane transporters coded to move the toxic ions out of the cell. Inside the cell, the microorganisms may be able to change their chemical state, changing toxic ion species into non-toxic substances or reversing redox reactions. And for cell's that need a certain ion to run physiological pathways, it may develop alternative pathways that do not need the toxic ion. There is also the option of repair, but this can be limited by energy, resources, and time. Many of these mechanisms are effected by the rate of influx of toxic metals and the persistence of attack. Eventually cellular systems and protective barriers are overcome and the cell succumbs to the invasion of toxic ions.⁹

Four main bio-factors affecting antimicrobial copper efficacy are: size, morphology, physical structure, and coded structure; see Figure 14 for more details.

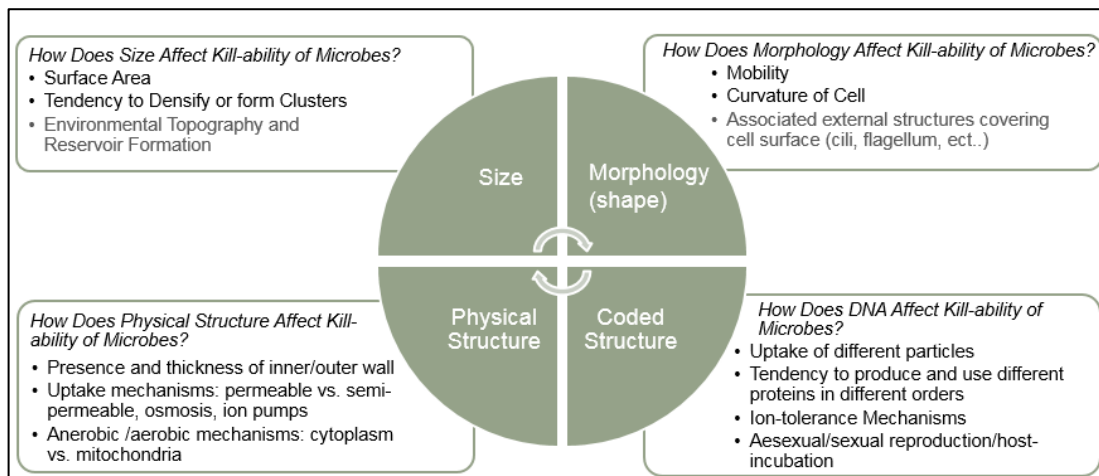


Figure 14. Summary of 'BioFactors' affecting efficacy testing of antimicrobial copper.

These factors may work individually or in combination to either increase or decrease the effects of antimicrobial copper. A cell with a certain morphology may have external structures that have a tendency to form clusters with surrounding cells, but if the size of each cell is too large in comparison to the surface topography, then there may be densification with no reservoir formation. One such situation may occur where there is nano-roughness, but

the cell is microns wide in size. Or the opposite may occur where the cells are small enough and reservoirs form between nano peaks and valleys.

Physical structure, like selective proteins on the cell membrane, may allow for only semi-permeability which can regulate initial uptake of ions. If the influx of ions increases, breaking through a section of the membrane, then larger cells may stand more of a chance of repair and survival. Also, cells with the ability to code for various changes to proteins, cell pH, and secondary pathways will have a higher chance of survival against toxic copper ions.

These factors hold different significances within each microorganism. There is much for scientists to continue to characterize by way of physical, chemical, and environmental factors affecting cellular defense mechanisms against copper ions.

2.1.4 Contact-Killing Mechanism

The main mechanisms for contact killing of copper are detailed in Figure 15. The copper kill mechanism is broken into four stages: 1) Copper dissolving, 2) cell membrane rupture, 3) copper induced reactive oxygen species (ROS), and 4) DNA degradation. These stages have been identified through observation of commonalities in efficacy testing of microorganisms in combination with the laboratory testing done on chemical and biological pathways of the cell.

▪ *What is the mechanism of contact killing?*

– There is still no clear answer, however, 4 contact killing stages have been identified:

1. Cu Dissolves

- Cu ions release from surface into environment
- This can happen in both a wet and dry environment

3. Cu induces ROS

- Inside cell, the Cu content remains high
- Redox reactions occur between different Cu species (Cu(i) and (ii))

2. Cell Membrane Ruptures

- Cell's resistance mechanisms hold out for as long as possible
- Cu ions break through cell membrane
- Releasing cytoplasm

4. DNA Degrades

- This is 2ndary damage
- Occurs from Cu Ion DNA fragmentation

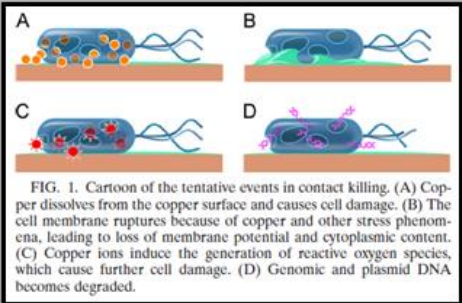


FIG. 1. Cartoon of the tentative events in contact killing. (A) Copper dissolves from the copper surface and causes cell damage. (B) The cell membrane ruptures because of copper and other stress phenomena, leading to loss of membrane potential and cytoplasmic content. (C) Copper ions induce the generation of reactive oxygen species, which cause further cell damage. (D) Genomic and plasmid DNA becomes degraded.

Reference: 6

Figure 15. Copper kill mechanisms described and conclusions drawn based on the lessons learned from the laboratory and hospital testing compiled in the results section.

In Stage 1, copper dissolves to form copper ions which are then released into the environment. The copper ions make their way to the cell using donor ligand receptors, or directly adhering to the external cellular membrane. The cell may use some of the copper for its physiological function, but when the concentration of copper becomes too great, both inside and outside the cell, preventative mechanisms are turned on to try and prevent rupture of the cell membrane and its internal structures. These preventative mechanisms may include backwards ion pumps, isolation and extrusion of ions from the matrix, and preventative use of external proteins to trap harmful ions that may try to land on the surface. In Stage 2, the cell's resistance mechanism give way and copper ions break through the cell releasing the cytoplasm. In Stage 3, the buildup of such a high copper ion concentration within the cell leads to the formation of damaging reactive oxygen species through redox reactions and the continued destruction of the cell's internal structures. As the copper makes its way through the cell, it reaches the DNA. If the DNA is not encased, the ROS react to degrade it in Stage 4. If a nuclear membrane is present it may take more time to reach the DNA, but eventually the influx of copper ions will break through as they did with the cellular membrane.

These four stages comprise the modern view of the copper kill mechanism. The specific pathways for copper entry into the cell and the order in which internal cellular structures are attacked by copper ions are still being researched. Much more research is needed to understand the variation in copper kill rate between microorganisms and the external factors affecting this range in antimicrobial effectiveness. In the meantime, a general baseline for effectiveness has been set by the CDC and supported by the EPA that, surfaces containing 60% or higher copper are antimicrobial and that surface toxicity increases with increasing copper content. Figure 16 lists some of the common myths and facts for Copper.

| Myths and Facts of Antimicrobial Cu: Reference: 11, 12, 19 | |
|--|--|
| %Cu | 60% or higher considered antimicrobial |
| Patinas | No Impact |
| Thin Oxide Layer | No Impact |
| Dry vs. Moist Cu | Dry>Moist for Contact Killing |
| Cleaning | Increased Effectiveness |

Figure 16. Facts and myths about Cu

In addition to 60% +Cu being antimicrobial, patinas and thin oxide layers do not appear to affect the antimicrobial properties. In dry environments the Cu can perform better than in moist environments and cleaning does not mitigate the properties of the Cu surface. ^{11, 12, 19}

2.1.5 Relationship between Antimicrobial and Material Properties

The prior sections have discussed factors affecting Cu contact-killing from a bio and chemistry perspective. It is important to look at prior research to also determine the effects of manufacturing processes on end material properties and how this may play a role in changing antimicrobial properties of Cu. The work discussed in Figure 17 comes from the Army Research Labs Cold Spray division.

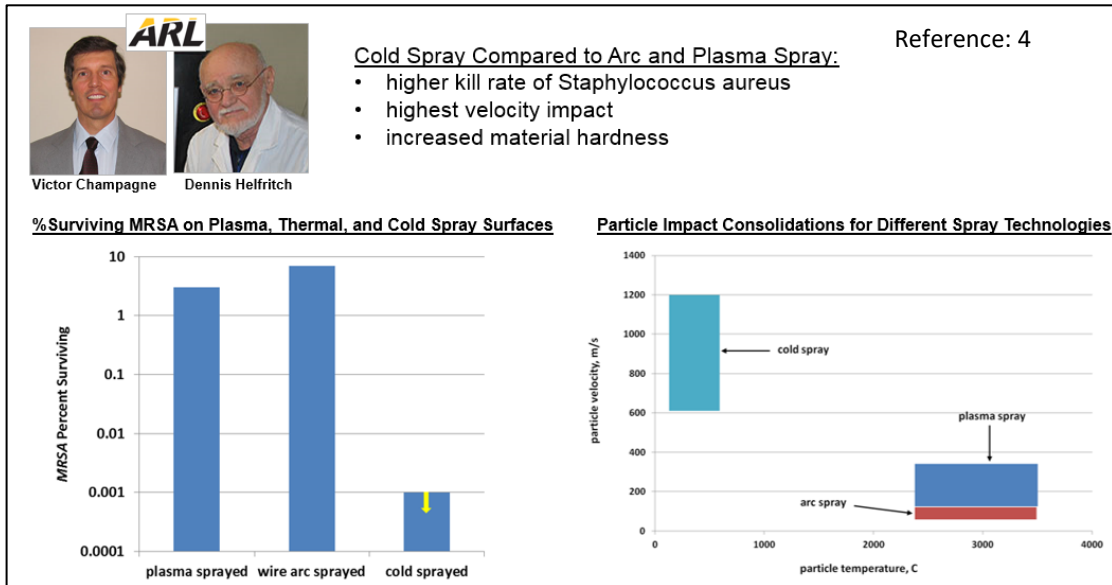


Figure 17. Relationship between Manufacturing, End Material Properties, and Antimicrobial Effectiveness

The works shows that as the velocity of powder deposition increases, this changes the material properties of the end sample resulting in increased antimicrobial effectiveness. More work is needed to determine exactly what material and mechanical property changes occur that affect the antimicrobial properties. The ARL group has hypothesized that the high velocity of cold spray allows for increased dislocation density and that with more dislocations there are more opportunities for ions to flow via pipe diffusion from the bulk material to the surface

and into the environment. Dislocations can be measured through hardness testing where there is a proportional relationship. The same group has shown that hardness is much greater for the cold spray than other additive manufacturing processes. More work may be needed to determine if pipe diffusion is the main factor affecting the change in antimicrobial properties.⁴

The scope of this project does include work to analyze microstructure, surface roughness, surface composition, and ion release for both nanomaterial and conventional Cu cold spray coatings to better understand Cu-ion movement in relation to Cu-kill mechanisms.

2.1.6 References

- [1] Balasubramanian, R., and A. C. Rosenzweig. 2008. Copper methanobactin: a molecule whose time has come. *Curr. Opin. Chem. Biol.* 12:245–249. (F3) Banerjee I. , Pangule R., and Kane R. 2011. Antifouling Coatings: Recent Developments in the Design of Surfaces That Prevent Fouling by Proteins, Bacteria, and Marine Organisms. *Advanced Materials.* 23: 690–718
- [2] Bott R., Bowmaker G., and Davis C..1997. Crystal Structure of $[Cu_4(tu)_7](SO_4)_2 \cdot H_2O$ and Vibrational Spectroscopic Studies of Some Copper(I) Thiourea Complexes. *Inorg. Chem.* 37: 651-657
- [3] Casey, A. L., et al. 2010. Role of copper in reducing hospital environment contamination. *J. Hosp. Infect.* 74:72–77.
- [4] Champagne, V.; Helfritsch, D. A demonstration of the antimicrobial effectiveness of various copper surfaces, *Journal of Biological Engineering* 2013, 7:8 <https://doi.org/10.1186/1754-1611-7-8>
- [5] Copper Development Association (2015) Properties of Wrought and Cast Copper Alloys.
- [6] Grass G., Rensing C., and Solioz M. 2011. Metallic Copper as an Antimicrobial Surface. *Applied and Environmental Microbiology.* 77: 1541–1547.
- [7] Vucko, M.J., et al. Cold spray metal embedment: an innovative antifouling technology. *Biofouling.* 2012;28(3):239-48.
- [8] Johnson G., Cook W., FRACTURE CHARACTERISTICS OF THREE METALS SUBJECTED TO VARIOUS STRAINS, STRAIN RATES, TEMPERATURES AND PRESSURES. *Engineering Fracture Mechanics* Vol. 21, No. 1, pp. 3148. 1985
- [9] Lemire J., Harrison J., and Turner R.. 2013. Antimicrobial activity of metals: mechanisms, molecular targets and applications. *Microbiology.* 11:371-384
- [10] Liu J (2006) Cold spray formation of thin metal coatings. US Patent Application US 2006/0090593.
- [11] Michels H.T., Noyce J.O., Keevil C.W., Effects of temperature and humidity on the efficacy of Methicillin-resistant *Staphylococcus aureus* challenged antimicrobial materials containing silver and copper. *Applied Microbiology.* 49 (2009) 191-195.
- [12] Mikolay A., et al. Survival of bacteria on metallic copper surfaces in a hospital trial. *Appl Microbiol Biotechnol* (2010) 87:1875-1879.
- [13] Moore E., Abel E., and Janes R. 2004. Metal-Ligand Bonding. Royal Society Of Chemistry.
- [14] Pereda-Ayo B., Torre U. , and Josellian-Gomez M. 2013. Role of the different copper species on the activity of Cu/zeolite catalysts for SCR of NO_x with NH_3 . *Applied Catalysis B: Environmental.* 147(5): 420-428.
- [15] Preston D., Tonks D., Wallace D., Model of plastic deformation for extreme loading conditions. *J. Appl. Phys., Vol.* 93, No. 1, 1 January 2003
- [16] Principles of General Chemistry. Chapter 23: “The d-Block Elements”. 2012. [online]. Available: <https://2012books.lardbucket.org/books/principles-of-general-chemistry-v1.0/s27-the-d-block-elements.html>. Assessed October 2017.
- [17] Rizvi M., Akhoun S., Maqsood S. 2013. Synergistic Effect of Perchlorate Ions and Acetonitrile Medium Explored for Extension in Copper Redoximetry. *Journal of Analytical Chemistry.* 70(5):633–638.
- [18] Rizvi M. Complexation Modulated Redox Behavior of Transition Metal Systems (Review). *Russian Journal of General Chemistry.* 85(4):959–973
- [19] Z. Santo, C.; Lam, E.; Elowsky, C.; Quaranta, D.; Domaille, D.; Chang, C.; Grass, G. Bacterial killing by dry metallic copper surfaces. *Appl. Environ. Microbiol.* 2011, 77, pp. 794–802.
- [20] Schmidt T., et al. Development of a generalized parameter window for cold spray deposition. *Acta Materialia* 54 (2006) 729–742.
- [21] Schultz, M. P. , Bendick, J. A. , Holm, E. R. and Hertel, W. M. (2011) 'Economic impact of biofouling on a naval surface ship', *Biofouling*, 27: 1, 87 — 98, First published on: 14 December 2010 (iFirst)

- [22] Sundberg K, Champagne V, McNally B, Helfrich D, Sisson R (2015) Effectiveness of Nanomaterial Copper Cold Spray Surfaces on Inactivation of Influenza A Virus. *J Biotechnol Biomater* 5: 205.
- [23] Varadwaj P., Varadwaj A., and Jin B. 2015. Ligand(s)-to-metal charge transfer as a factor controlling the equilibrium constants of late first-row transition metal complexes: revealing the Irving–Williams thermodynamical series. *Phys.Chem.Chem.Phys.* 17: 805-811.
- [24] Wiegand, Irith, Kai Hilpert, and Robert EW Hancock. "Agar and broth dilution methods to determine the minimal inhibitory concentration (MIC) of antimicrobial substances." *Nature protocols* 3.2 (2008): 163.

3. Paper #1: The Effect of Nano-Scale Surface Roughness on Copper Cold Spray Inactivation of Influenza A Virus

The Effect of Nano-Scale Surface Roughness on Copper Cold Spray Inactivation of Influenza A Virus

Kristin Sundberg^{1,*}, Matt Gleason², Baillie Haddad³, Victor Champagne, Chris Brown, Richard Sisson, and Danielle Cote

^{1,2,3} Materials Science and Engineering, Worcester Polytechnic Institute, Worcester, MA, USA

*Corresponding author: kristinsundberg7@yahoo.com

Abstract Copper has been identified as an antimicrobial material, with over 450 copper alloys approved by the EPA [8]. Previous work with conventional and nanomaterial copper cold spray surfaces has demonstrated efficacy in percent reduction of both MRSA and Influenza A Virus, with nanomaterial copper having better results for virus efficacy than conventional copper [1]. The main mechanism of copper contact killing is believed to be Cu ion release [12]. The surface roughness of the conventional and nanomaterial copper cold spray surfaces was examined in order to further explain the mechanisms that caused the observed difference in Influenza A virus efficacy testing. Results showed that both the percentage of grain boundaries and surface roughness may be contributing factors in copper's kill-mechanism at the nano-scale. The surface roughness below 0.1 μm^2 and above 1000 μm^2 was much greater for nanomaterial copper surfaces than conventional copper, however the opposite was true between these values. It was determined that there appeared to be a localized relationship at the nano-scale between increased surface roughness and percent Cu ion diffusion, similar to the relationship of ion diffusion to the percentage of grain boundaries [1]. However, further research is needed to uncouple the individual contribution of surface roughness and grain boundaries to copper kill rate.

Keywords: *Surface Roughness, Relative Area, Cold Spray, Nanomaterial Copper*

1. Background

The Center for Disease Control (CDC) states that the number of deaths per year due to Influenza and Pneumonia related illnesses has reached up to 55,227 in select years [7]. Additionally, MRSA causes approximately 14,000 deaths and 250,000 hospitalizations per year [5]. Self-cleaning surfaces, such as copper, are being used in hospitals to prevent the spread of infectious diseases across medical equipment and work surfaces [20, 14]. It is believed that the contact killing mechanism for microbes is copper ion diffusion, indicating that with increases in Cu concentration there is an increased kill rate [12]. Cold spray is an additive manufacturing method used to coat surfaces with Cu and other metals. Cold spray propels metal powder particles at a high velocity (600-1000 m/s) and relatively low temperature (100-500°C) at a substrate to form low porosity and low oxide coatings. The high hardness and density of the coating from the cold spray process results in an increased kill rate as compared to other additive methods using lower-velocity processes [9].

This is a follow-on study to the paper "Effectiveness of Nanomaterial Copper Cold Spray Surfaces on Inactivation of Influenza A Virus" [19]. This paper explores the relationship between work hardening, grain boundaries and ion diffusion. Where, the velocity of the cold spray process coupled with the unique grain structure of the nanomaterial Cu allows for increased kill rate of Influenza A Virus. Cold sprayed nanomaterial Cu coating was compared to cold sprayed conventional Cu coating, which contained larger particles with fewer grain boundaries. The results from testing are shown in Figure 1. [19]

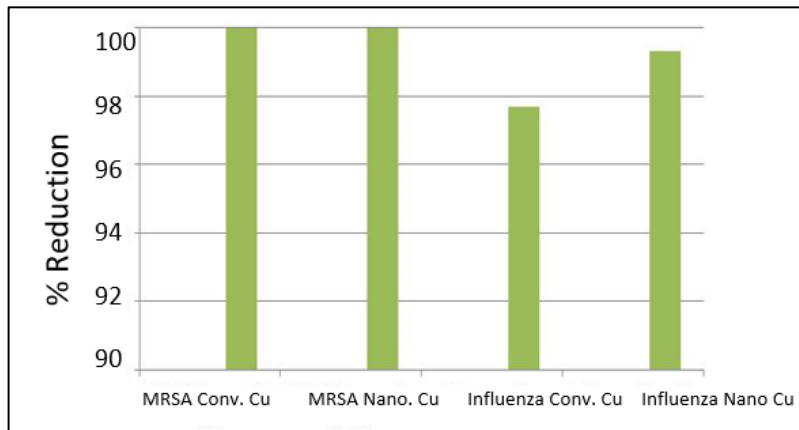


Figure 1: Percent reduction of MRSA and influenza A virus after 2 hour exposure to various copper deposits. [19]

In the above graph, it is shown that copper surfaces have a higher kill rate for MRSA than for Influenza A. It is hypothesized that surface roughness at the MRSA (0.5- 1.0 μm) and Influenza A (80-120 nm) scales are a leading factor in percent reduction [17, 6]. A mismatch in size between the surface roughness and the scale of the microbe leaves large surface pockets available which increases the likelihood of microbe congregation to form reservoirs of thriving bio organisms [21]. Additionally, the mismatch in roughness can contribute to the ability of microbes to adhere to a surface [13]. Roughness may cause destabilization of cell membranes and viral capsids through both increased toxic Cu ion transfer and puncture of the cell wall [11].

Topography also results in greater contact area and may significantly influence the transfer or dissolution of ions from the material [22]. The roughness of the cold sprayed nanomaterial copper on the nanoscale could be providing a greater advantage for microbe reduction than that of conventional copper. Similarly, the relationship between surface roughness and conventional copper on the micron scale could provide a greater advantage than that of nanomaterial copper at that level. In order to measure at both the micro- and nanoscales, this paper uses 3D confocal microscopy and atomic force microscopy, respectively.

Current research on contact killing of bacteria on copper shows that the suppression of bacteria-metal contact prevents killing [13]. Less work has been done quantitatively for topology, with most surface assessments relying on conventional roughness parameters such as Ra, which lack spatial specificity and fine scale sensitivity [4]. Microbes of different sizes interact with a surface at different length-scales, thus it is important to characterize the surface topography with a scale sensitive technique. This paper focuses on multiscale analysis, using the fractal tiling method developed by Brown et al which simulates the effect of different observational scales on surface area [2]. Unlike many multiscale methods, this technique has a clear physical interpretation, and surface area has a direct effect on a wide range of surface phenomena [4].

Through multiscale analysis, area scale, complexity, and volume scale plots can be formed. Area scale is a fractal tiling method where the surface is tessellated with triangles of the same size in order to determine the observable area at the scale of those tiles. Large-scale features affect relative area values at finer scales. Large-scale features are still contributing to the total area regardless of the observable scale. Complexity removes the influence of large-scale features at the scale of observation, whereas relative area is dependent on all the features that are larger than it. Complexity is the first derivative of the area scale plot, which shows the roughness at a particular scale. Volume scale analysis looks at how volume varies at different scales of observation or the fraction of space that can be filled. [2]

The aim of this research is to provide further analysis of surface metrology on the micro- and nanoscales to better understand the reason why consolidated nanomaterial Cu performs better than conventional Cu in percent

reduction of Influenza A Virus and to relate findings to why the coating did not perform as well as in percent reduction of MRSA. Characterizing the factors affecting Cu antimicrobial efficiency will help in better understanding the kill mechanism and in future optimization of the Cu coatings for healthcare applications.

2. Test Procedure

2.1. Cold Spray

Cold spray samples from the prior paper, “Effectiveness of Nanomaterial Copper Cold Spray Surfaces on Inactivation of Influenza A Virus” [19], were used. The pure Cu cold spray coatings on aluminum substrates are approximately 0.05 mm thick. The nano-agglomerate copper (Eltron) and conventional copper (Praxair Cu-159) powders are produced through spray drying and gas atomization, respectively. Due to the low mass of the nanoparticles, they are bound into agglomerates using conventional Cu as the binder and spray dried [16, 18]. For more information on the materials and cold spray process parameters see reference 19.

2.2. Visual and Microstructural Analysis

The interior of the coatings was studied through microscopy to illustrate the difference in grain size and number of grain boundaries between the nano and conventional copper coatings. The conventional Cu coating was cross sectioned in a Helios NanoLab G3 UC DualBeam scanning electron microscope/focused ion beam (SEM/FIB) and imaged with the ion beam. A thin film of the nano Cu coating was prepared in the same SEM/FIB and imaged in an FEI Talos F200X scanning/transmission electron microscope (STEM).

2.2.1. Measurement Analysis

The grain sizes of the conventional and nanomaterial Cu cold spray deposits were measured in an Olympus Stream Image Analysis Software. More than 50 grains were measured per category. Grain outliers were removed with Dixon’s Q-test, and the range and average are reported for each category.

2.3. Surface Roughness Measurement

Topographic measurements at micrometer length scales were taken with an Olympus Lext OLS4100 scanning laser confocal microscope. Imaging was performed with the 50x objective providing magnifications at 1080x.

To investigate the topography at nanometer length scales, measurements were taken with a Nanosurf Naio AFM operating in contact mode. The cantilevers used were MikroMasch HQ:CSC17 cantilevers and the image resolution was 1024x1024.

2.3.1. Measurement Analysis

The confocal measurements were filtered to remove spurious points using the outlier filter in software MountainsMap by Digital Surf. The points removed comprised <0.01% of the total surface. The AFM images were not filtered. Area-scale fractal analysis was performed with Sfrac by Surfract with the Four Corners Full Overlap tiling algorithm. Sfrac was used to analyze the surface data for volume scale where the volume-ratio was used with the ratio being one [3].

3. Results and Discussion

3.1. Microstructure

The cross-sectional FIB image of the conventional Cu coating cold sprayed with gas-atomized particles is shown in Figure 2. The lens-shaped deformed particles are evident, as well as highly plastically deformed particle boundaries. A large particle with several larger grains is found in this cross section. A higher magnification image of the largest grains and a particle-particle interface is shown in Figure 3. This region at the particle-particle

interface, where the most plastic deformation occurred, contains bands that formed during the cold spray process with smaller grains than in the interior of the particles [15].

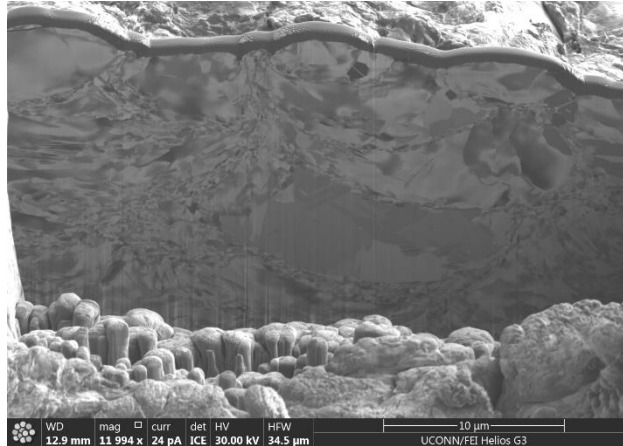


Figure 2: Cross-sectional focused ion beam image of the conventional copper coating

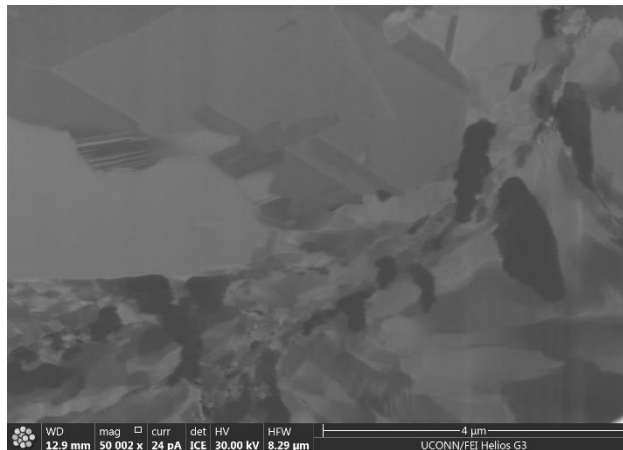


Figure 3: Higher magnification cross-sectional focused ion beam image of the conventional copper coating

A STEM image of the nanomaterial Cu coating cold sprayed with spray dried nanoparticle agglomerates is shown in Figure 4. The different contrasting stripes are an artifact from sample preparation. In order to understand the different regions of this sample, it is important to know the material inputs. During fabrication, micron-sized particles are formed by spray-drying nano particles that were agglomerated with a pure copper binder [18]. As a result, this sample includes regions of conventional copper with micron-sized grains, as well as areas of nanostructured copper. The lighter regions that are swirled with the micron-sized grains contain the nanostructure. A higher magnification image of the nanostructure copper is shown in Figure 5.

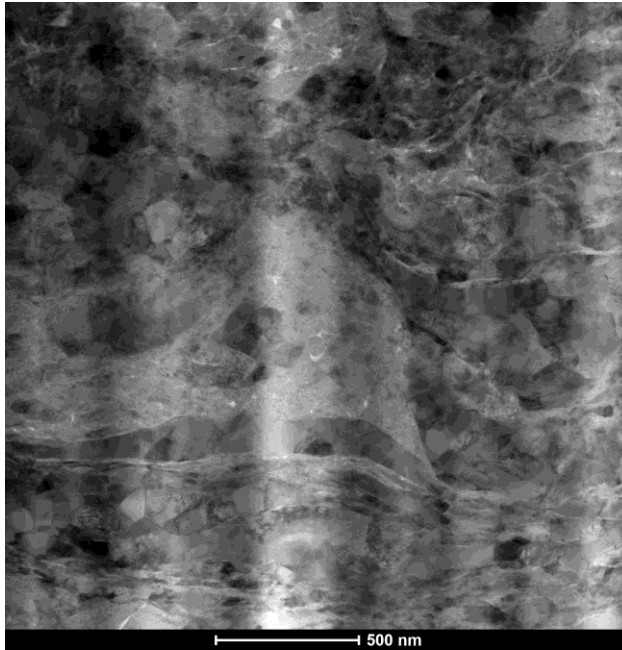


Figure 4: STEM image of nano copper coating

The nano-sized grains of the nanomaterial Cu are shown clearly in Figure 5. The particle in the middle that is surrounded by a hole in the sample that formed during sample preparation is hypothesized to be one of the agglomerated particles that contains nanoparticles. It is known that an increase in grain boundaries and dislocations increases ion diffusion, which is believed to be the main mechanism for contact killing of microbes [12]. The nano-grains in the nanomaterial Cu allow for increased kill rate of the Influenza A virus.



Figure 5: STEM image of the nano copper coating showing the nanostructured particles

Grain size measurements were made of the nanomaterial and conventional Cu and a summary of the results is reported in Table 1. For the cold sprayed conventional Cu, the average size of the majority of the grains was 0.2 ± 0.2 microns, while the largest of the grains in the sample were 2.2 ± 1.5 microns with the largest being almost 5 microns in diameter. The cold sprayed nanomaterial Cu contained nano-sized grains as well as micron-sized grains, measuring an average 10.6 ± 2 nm and 0.4 ± 0.1 microns, respectively. The size of the nano-grains is the

clear difference between the samples and must be one of the factors affecting the higher virus kill rate in the nanomaterial Cu.

Table 1: Grain size measurements

| | Conventional Coating | | Nanostructured Coating | |
|----------|-------------------------------|--------------------------------|------------------------|-------------------------------|
| | Conv grains (μm) | Large grains (μm) | Nano grains (nm) | Conv grains (μm) |
| Min | 0.1 | 1.0 | 7.3 | 0.2 |
| Max | 1.0 | 4.9 | 15.1 | 0.7 |
| Ave. | 0.2 | 2.2 | 10.6 | 0.4 |
| σ | 0.2 | 1.5 | 2.0 | 0.1 |

3.2. Surface Roughness

The results of the area-scale analyses are displayed in Figures 6, 7, and 8. Area scale analysis looks at how area varies at different scales of observation [2]. In this case, the below figures detail changes in surface roughness on the micro- to nanoscales representative of the size scales for MRSA (0.5-1 μm) and Influenza A virus (80-120nm) [17, 6].

The cold sprayed conventional and nanomaterial copper surfaces are shown at the 50X objective in Figures 6. Less of a change in slope is seen between the large-scale measurements taken with the 3D confocal microscope as compared to the smaller-scale measurements taken with AFM.

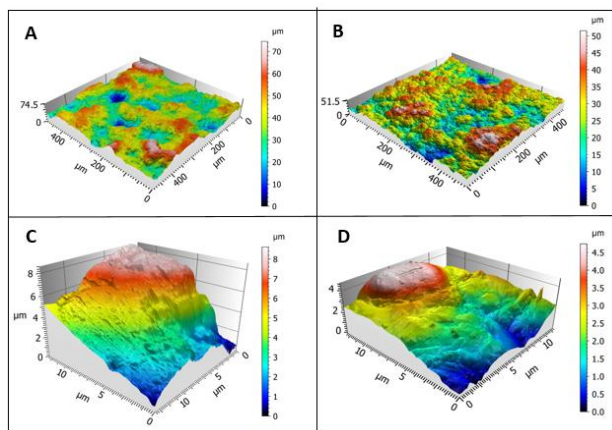


Figure 6: 3D confocal Images at 50X A) conventional Cu B) nanomaterial Cu. AFM images at 15x15 μm^2 C) conventional Cu D) nanomaterial Cu.

Visual inspection of the 3D confocal measurements between the conventional and nanomaterial Cu shows what appears to be greater roughness in the latter sample. The relative area and complexity plots confirm the visual assessment made above. Plots based off the 3D confocal measurements are shown in Figure 7. The yellow line in both the relative area and complexity plots indicates the scale at which MRSA is present, 0.5-1 μm [6]. The green line in the plots is an indicator for 3D confocal optical resolution limit.

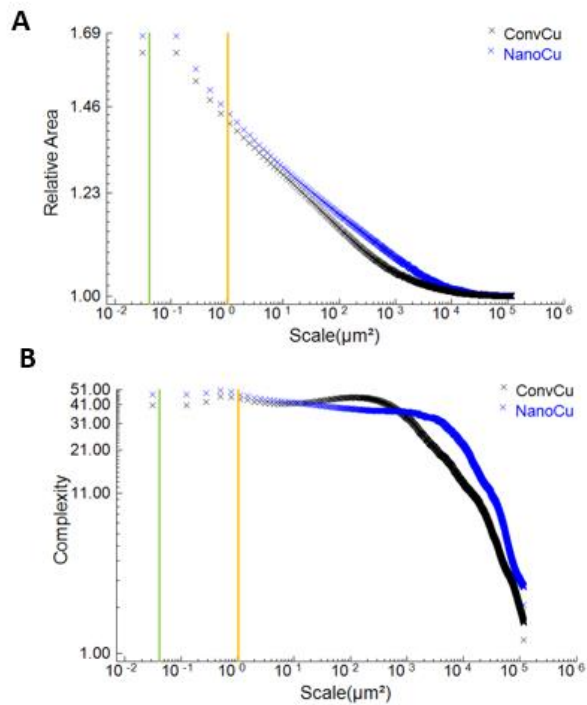


Figure 7: From 3D Confocal data- A) Relative Area Plot at 50X, and B) Complexity Plot at 50X

Quantification of the relative surface area of the 3D confocal measurements in Figure 7A shows that above $1000\mu\text{m}^2$, nanomaterial Cu surface area is greater than that of conventional Cu. Again, below $10\mu\text{m}^2$, nanomaterial Cu has the greater surface area. The complexity plot in Figure 7B allows for a clearer image of the transition in surface roughness at $10\mu\text{m}^2$, as complexity removes the influence of large-scale features at the scale of observation.

Despite nanomaterial copper's greater surface roughness, it does not seem to have an impact on the kill rate of MRSA at the 2-hour mark, as both the nanomaterial and conventional surfaces show 99% reduction of MRSA at that timepoint [19].

The relative area and complexity plots based on AFM measurements are shown in Figure 8. The yellow line in both the relative area and complexity plots indicates the scale at which MRSA is present, $0.5\text{-}1\mu\text{m}$ [17]. And the red line indicates the scale at which Influenza A Virus is present, $80\text{-}120\text{nm}$ [6]. Note that while the green line indicating 3D confocal optical resolution limit is not present, the value falls between the red and yellow lines.

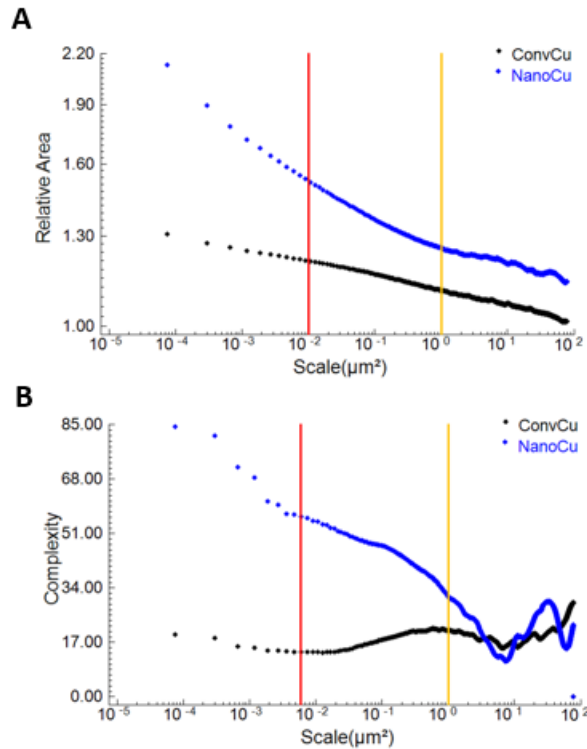


Figure 8: From AFM data- A) Relative Area Plot at 50X, and B) Complexity Plot at 50X

The relative area plot of the AFM data shows an increase in nanomaterial Cu surface roughness with decreasing scale. The complexity diagram in Figure 8B shows a relationship between decreasing scale and increasing difference in surface roughness between the nanomaterial and conventional Cu, where nanomaterial Cu continues to increase in surface area and conventional Cu stagnates.

Greater surface roughness may impact antimicrobial effectiveness of cold sprayed nanomaterial Cu against Influenza A Virus, as the nanomaterial Cu surface shows greater percent reduction of the virus over a 2-hour period compared to conventional copper [19].

Volume scale analysis looks at how volume varies at different scales of observation [3]. Volume scale comparison at the micro- and nanoscale is presented in Figure 9. The y-axis of the graphs is a measurement of fraction volume filled, which shows at a given scale how much of the surface is filled in. Nanomaterial Cu has much greater fraction volume filled at both the nano-scale in Figure 9B and micron-scale in Figure 9A than conventional Cu. Viewing the volume scale graphs at the MRSA scale, 0.5-1 μm , and Influenza A Virus scale, 80-120nm, the same observation holds true. This indicates that the nanomaterial Cu has greater pockets and reservoir formation than conventional Cu. While the exact diameter of the pockets/reservoirs is not able to be determined from the volume scale data provided, the starting size can be estimated at $\sim 10^2 \mu\text{m}^2$ as seen from the confocal measurement in Figure 9A.

Fraction volume filled is a good determination of the amount of volume held by the sample in relation to itself, but it does not normalize the effect of minimum and maximum points on the surface, where nanomaterial Cu has a much wider range than that of conventional Cu, as previously shown in surface roughness Figures 7 and 8. While fraction volume filled shows the structural difference between the two samples, it does not allow for a direct comparison between the two; total volume measurement is needed for that.

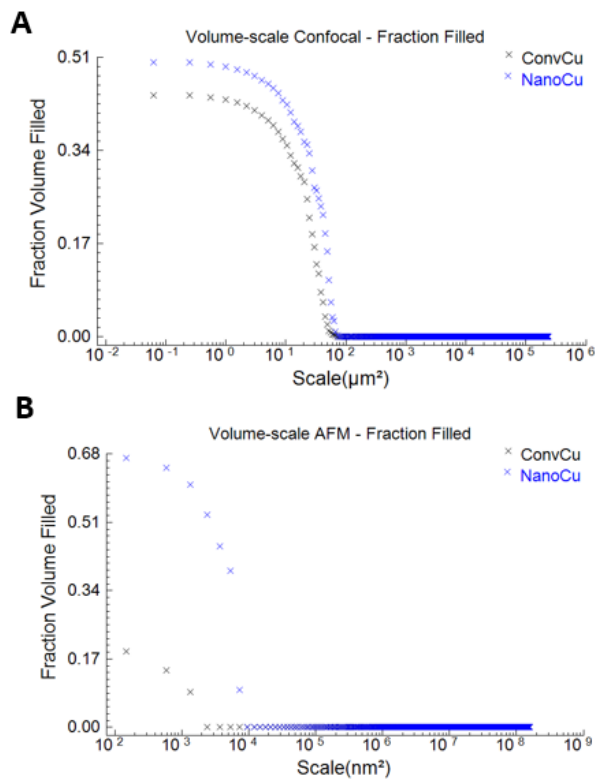


Figure 9: Volume scale A) Confocal B) AFM

Complexity, the slope of the fraction volume filled, is shown in Figure 10.

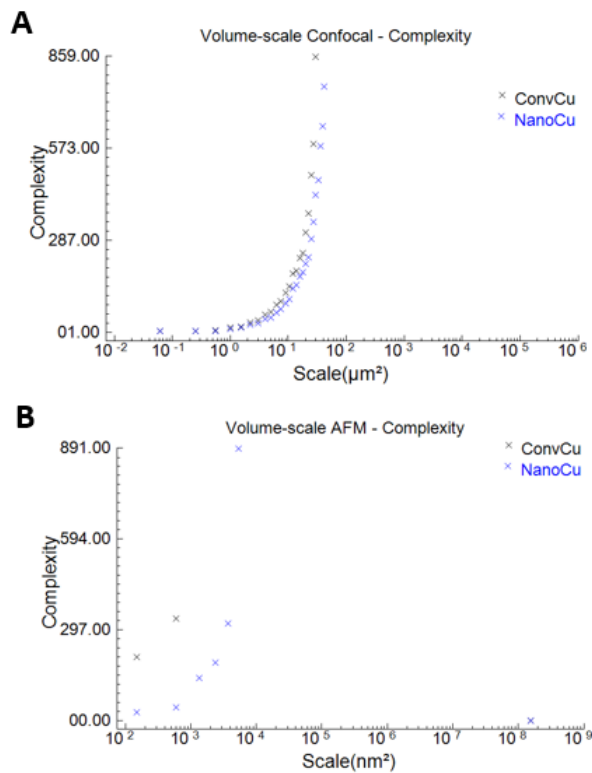


Figure 10: Volume scale Complexity A) Confocal, B) AFM

Volume scale complexity indicates how quickly the surface jumps from small to large pockets/holes. High complexity values indicate a short gradient between small and larger holes, indicative of a bi-modal distribution

with very small and very large holes but minimal medium-sized ones. Whereas low complexity values indicate longer, more gradual or gaussian-like gradients with a wider range of sizes between the small and large holes. Cold sprayed conventional Cu has slightly higher complexity values than nanomaterial Cu showing a quicker change in pore size. The nanomaterial has a more gradual change in pore size, most likely due to the powder containing both nanoparticles and conventional Cu binder.

4. Conclusion

Two factors affecting copper kill mechanisms include the percentage of grain boundaries and surface area. An increase in grain boundaries allows for increased Cu ion diffusion [10]. Surface roughness is proportional to surface area [22]. Depending on the powder particles used in the cold spray process, increased surface area could be an indicator of an increased number of grain boundaries. However, greater surface roughness can also mean more area for reservoir development [13].

As seen in the micrographs and measurement of grains, cold sprayed nanomaterial Cu has much smaller grains than cold sprayed conventional Cu. This supports the efficacy testing data showing nanomaterial copper with greater percent reduction of Influenza A Virus than conventional copper. However, both the nanomaterial and conventional copper surfaces appear to have the same percent reduction on MRSA after 2 hours.

Surface roughness may also contribute to copper kill-rate at the nanoscale, as seen in the 50X relative area scale plot in Figure 8. The surface roughness of nanomaterial Cu is much greater than conventional Cu at the scale of Influenza A and supports the efficacy testing that showed greater percent reduction of Influenza A by nanomaterial Cu than conventional Cu. The surface roughness of nanomaterial and conventional Cu is much closer for the MRSA scale, with nanomaterial Cu having slightly greater values. Surface roughness does not seem to affect the efficacy testing of MRSA as the percent reduction results at 2 hours are the same for both materials [19].

Volume scale data supports the area scale results with cold sprayed nanomaterial Cu having much greater fraction volume filled than conventional Cu at both the micro- and nanoscales. Interestingly, complexity values show steeper gradient for conventional Cu than nanomaterial Cu, indicating a greater pore size variation for the latter, most likely due to the differences in powder production.

At larger scales (0.1 μm^2 and above) surface roughness seems to have less of an effect on kill-rate than at the nanoscale. Follow-on research is needed to determine to what extent the variables of percent grain boundaries and surface roughness are coupled. Performing regression testing to determine optimal material surface roughness for fastest kill-rate may provide further insight [2]. Additional testing is also needed to determine if the kill-rate between the two surfaces varies prior to the 2-hour exposure time. And quantification of the percent of grain boundaries on both the conventional and nanomaterial copper surfaces at the micro- and nanoscale is needed to confirm that proportionality between surface roughness and percent grain boundaries.

References

- [1] Askeland, D., Fulay, P., Wright, W.. The Science and Engineering of Materials. USA, Cengage Learning, 2011.
- [2] Brown, C.A., Charles, P.D., Johnsen, W.A., Chesters, S., 1993, Fractal analysis of topographic data by the patchwork method, *Wear*, 161/1-2:.61-67
- [3] Brown CA, Hahn RS St, Gelais RM, Powers B, Geiger DJ (2007) Grinding Wheel Texture and Diamond Roll Plunge Dressing Feed-Rates. ISAAT 2007/SME International Grinding Conference, Society of Manufacturing Engineers, Dear-born, MI.
- [4] Brown, C., Hansen, H., Jiang, X., Blateyron, F., Berglund, J., Senin, N., Zahouani, H. (2018). Multiscale analyses and characterizations of surface topographies. *CIRP Annals*, 67(2), 839–862

- [5] Center for Disease Control and Prevention. CDC Newsroom.<http://www.cdc.gov/media/releases/2013/p1212-mrsa-cdifficile.html>
- [6] Center for Disease Control Prevention. Electron Micrograph of Methicillin-Resistant *Staphylococcus aureus*(MRSA).http://faculty.ccbcmd.edu/courses/bio141/lecguide/unit1/shape/EM_MRSA_staph.html
- [7] Center for Disease Control and Prevention. National Center for Health Statistics.
<http://www.cdc.gov/nchs/fastats/deaths.htm>
- [8] Copper Development Association.(2015).Properties of Wrought and Cast Copper Alloys.
- [9] Champagne V, Helfritsch D (2013) A demonstration of the antimicrobial effectiveness of various copper surfaces. *Journal of Biological Engineering* 7:8.
- [10] Champagne V, Helfritsch D, Trexler M (2007) Some Material Characteristics of Cold-Sprayed Structures. *Res Lett Mater Sci*.
- [11] Grass G., Rensing C., and Solioz M. 2011. Metallic Copper as an Antimicrobial Surface. *Applied and Environmental Microbiology*. 77: 1541–1547.
- [12] Lee F, Wang D, Chen L, Kung C, Wu Y, et al. (2013) Antibacterial nanostructured composite films for biomedical applications: microstructural characteristics, biocompatibility, and antibacterial mechanisms. *Biofouling* 29: 295–305.
- [13] Mathews, S., Hans, M., Mücklich, F., & Solioz, M. (2013). Contact Killing of Bacteria on Copper Is Suppressed if Bacterial-Metal Contact Is Prevented and Is Induced on Iron by Copper Ions. *Applied and Environmental Microbiology*, 79(8), 2605–2611. <http://doi.org/10.1128/AEM.03608-12>
- [14] Michels H, Wilks S, Noyce J, Keevil C (2005) Copper Alloys for Human Infectious Disease Control. Proceedings of the Materials Science and Technology Conference, September 25-28, 2005, Pittsburgh, PA Copper for the 21st Century Symposium.
- [15] M.R. Rokni, S.R. Nutt, C.A. Widener, V.K. Champagne, and R.H. Hrabe, “Review of Relationship Between Particle Deformation-Coating Microstructure and Properties in High Pressure Cold Spray,” *Journal of Thermal Spray Technology* (2017) 1-40. DOI: 10.1007/s11666-017-0575-0
- [16] Praxair: surface technologies. Powder Solutions: product brochure. www.praxairsurfacetechologies.com.
- [17] Rapid reference to influenza. The influenza virus: structure and replication. Elsevier Ltd. <http://www.rapidreferenceinfluenza.com/chapter/B978-0-7234-3433-7.50009-8/aim/influenza-virus-structure>
- [18] Rolfe S, (2014) email conversation and Phase I SBIR Final Report, “Advanced Nanostructured Powders for Cold Spray Applications”, Eltron Research and Development Inc., 4600 Nautilus Court South Boulder, CO 80301-3241.
- [19] Sundberg, K., Champagne, V., McNally, B., Helfritsch, B., Sisson, R., “Effectiveness of Nanomaterial Copper Cold Spray Surfaces on Inactivation of Influenza A Virus,” *J Biotechnology and Biomaterials*, 5 (4). 2015.
- [20] Tamimi A, Carlino S, Gerba C (2014) Long-term efficacy of a self-disinfecting coating in an intensive care unit. *American Journal of Infection Control* 42: 1178-81.
- [21] Verran J, Boyd R (2000) The Relationship Between Substratum Surface Roughness and Microbiological and Organic Soiling: a Review. *Biofouling* 17: 59-71.
- [22] Whitehouse DJ (2010) *Handbook of Surface and Nanometrology*, CRC Press, Boca Raton, FL.

4. Paper #2: Modeling Copper Cold Spray Single-Particle Impact for Optimized Antimicrobial Coatings

Modeling Copper Cold Spray Single-Particle Impact for Optimized Antimicrobial Coatings

Kristin Sundberg^{1*}, Bryer Sousa², Jeremy Schreiber³, Tim Eden, Caitlin Walde, Richard Sisson, Danielle Cote

^{1,2} Materials Science and Engineering, Worcester Polytechnic Institute, Worcester, MA, USA

³ Applied Research Laboratory, The Pennsylvania State University, University Park, PA, USA

*Corresponding author: kristinsundberg7@yahoo.com

Abstract Copper cold spray coatings have greater success at contact-killing of microbes than other additively manufactured copper coatings^[7]. While work has been done to increase antimicrobial properties through the use of nano-agglomerate Cu powder, it is possible to further optimize copper cold spray antimicrobial properties with an improved through process model^[34]. Conventional copper cold spray single particle impact is modelled using Johnson-Cook (JC) and Preston-Tonks-Wallace (PTW) in Abaqus finite element (FE) software to determine von Mises flow stress and particle morphology. Results show the von Mises flow stress for JC at 367MPa and PTW at 394MPa, with discrepancies largely due to the different initial assumptions/inputs made. Model outputs are compared to microstructure, static nanoindentation of powder/single-splat/consolidated Cu, and novel dynamic nanomechanical testing of consolidated coatings. Results from JC and PTW show similar morphology to the single-splat micrograph, with PTW having more accurate results for jetting and particle-impact geometry. Calculated flow stress values derived from static and dynamic nanoindentation test data show some discrepancies as compared to the model values, which may be due to assumptions made in the empirical formulas and differences in initial feedstock used. Additional work is needed to perfect the current models and to modify them for nano-agglomerate Cu powder single and multi-particle impact. Continued work with the model may afford the ability to pinpoint the best cold spray parameters for use in optimization of antimicrobial properties while still maintaining the structural integrity of the material.

Keywords: *Antimicrobial Copper, Cold Spray, Johnson-Cook, Preston-Tonks-Wallace, Nanoindentation*

1. Background

Copper cold spray coatings have been identified as having greater antimicrobial effectiveness than other additive methods, with the high impact velocity of the cold spray process (600-1000 m/s) being the main contributing factor^[7]. This paper builds off of prior work from the paper “Effectiveness of Nanomaterial Copper Cold Spray Surfaces on Inactivation of Influenza A Virus”, where copper cold spray antimicrobial properties are improved with the use of nano-agglomerate Cu powder^[34].

Continued optimization of surfaces is important for combating growing antibiotic resistance^[7,8]. Models can be used to determine the best cold spray parameters to use for optimization of antimicrobial properties, while still maintaining the structural integrity of the material, and may help understand Cu kill-mechanisms^[22,24]. This work aims to set a baseline for modelling of copper cold spray by first looking at single-particle impact of conventional Cu.

Two models based in Abaqus FE software are considered: 1) Johnson-Cook (JC), and 2) Preston-Tonks-Wallace (PTW). Both are high-strain-rate plasticity models that take inputs from cold spray process parameters and can output impact temperature, velocity, von Mises flow stress, plastic equivalent strain, and morphology data. von Mises flow stress is the average between yield stress (YS) and ultimate tensile stress (UTS), which is the flow stress required to allow elasto-plastic deformation to continue to plastically deform the material^[9].

The JC model, in use since the 1980's, breaks down above 10^5 /s strain rate. PTW is a newer model that does not rely on empirical materials models, but rather on thermodynamics and can provide accurate plasticity behavior from 10^{-3} – 10^{13} /s strain rate. However, the same meshing constraints apply for both models, making it difficult to model nanomaterials. This paper looks at the single particle impact for conventional copper powder with both JC and PTW.^[31, 16, 28]

To validate the modelled flow stress output, modelled strain values can be used in Hollomon's (power) Law equation to determine the output stress for Cu in its annealed state ^[2, 32], with the equation as follows:

$$(4) \quad \sigma = K \varepsilon^n$$

Where K is the strength coefficient for annealed Cu (315 MPa), ε is the modelled strain, and n is the strain hardening exponent for Cu (0.54) ^[6]. The power law does not account for strain rate, making it a tool to estimate the general magnitude of the modelled flow stress outputs. Further materials microstructure and hardness testing is needed to understand model validity and impact.

For the impact of a single copper particle, there are morphologies/microstructures specific to the cold spray process including particle deformation, jetting, and substrate-particle interlocking. Particle deformation occurs from high particle velocity on impact. For Cu powder propelled in a carrier gas towards a static Al substrate, the Cu powder momentum is transferred on impact in the form of kinetic energy to the surrounding Al substrate causing deformation. Jetting occurs from severe plastic deformation at the particle/substrate interface where material from both the particle and substrate push up along the interface edge. The particle still has downward momentum as the 'jet' material continues to flow out/up, this downward pressure allows for the mixing of the particle and substrate to form a strong bond. ^[11, 31, 18]

Nanoindentation can be used alongside microstructural examination to capture nanohardness and mechanical data to validate JC and PTW models. Static nanoindentation test data using a Berkovich tip can be converted to Vickers Hardness Number (VHN) through a geometrical relationship where the projected Berkovich tip cross-sectional area at a given depth matches the area of a Vickers indenter tip at the same depth. The derived equation is as follows ^[26, 13, 25]:

$$1) \quad \text{VHN} = 0.0945 * \text{NI (MPa)}$$

VHN can then be converted to YS. An empirical relationship has been developed for bulk cold-worked Cu alloys for both YS and UTS that takes into account the effects of cold working and strain hardening on yield strength of the material ^[20]:

$$2) \quad \text{UTS} = 3.353 * \text{VHN (MPa)}$$

$$3) \quad \text{YS} = 2.874 * \text{VHN (MPa)}$$

The flow stress can then be determined by taking the average between the YS and UTS values.

The change in tip geometry from a sharp Berkovitch tip to a spherical tip allows for the continued measurement between elastic, elasto-plastic, and plastic conditions along the indentation curve. Measurements can be converted to stress/strain values and plotted to find YS and UTS using prior work from Pathak, Kailidini, and Leitner ^[27,23].

Hardness measurement can also be used to predict cold spray microstructural properties in powder and consolidated coating using the Hall-Petch relationship, which states that grain-boundary strengthening, and subsequent material yield strength, increases with decreasing grain size ^[5].

This work uses JC and PTW models for single-particle impact of conventional copper powder on an aluminum substrate. Model outputs of flow stress and morphology are compared to measured microstructure and hardness values. Follow-on work is needed to model the single-particle impact of nano-agglomerate copper powder and the effects of multi-particle impact. Creating a relationship between cold spray parameters and end material properties will allow for future optimization of copper cold spray coatings, including improvement of copper antimicrobial properties.

2. Test Procedure

2.1. Consolidated Cold Spray

Cold spray samples of conventional and nanomaterial copper (0.5mm thick) on aluminum substrates are used from the paper, "Effectiveness of Nanomaterial Copper Cold Spray Surfaces on Inactivation of Influenza A Virus"

[34]. The conventional Cu powder (Praxair) is made through gas atomization of pure Cu. The nano-agglomerate Cu powder (Eltron) is made from spray drying, where nano particles ranging 60-80nm in size are encapsulated in a pure Cu binder. The particle size of the nano-agglomerate Cu powder is an average of 25um, and the conventional Cu powder is a range of -31/+5 microns in size; both powders are shown in Figure 1.

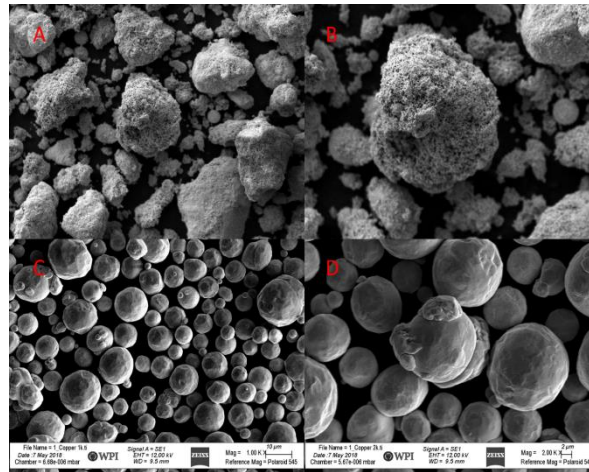


Figure 1: SEM images of Nano-agglomerate (A+B) and Conventional (C+D) Cu Powder

2.2. Fast-Raster Single Particle Splats

The VRC Gen III MAX cold spray system at the Pennsylvania State University (PSU) Applied Research Lab was used to deposit individual particles on four 1.00 in x 6.00 in x 1/8-in thick Al 6061 substrates. This single-splat fabrication via “fast-raster” cold spray resulted in single particle deposits for experimental analysis in support of the FEA work. The powder used from PSU was gas atomized pure Cu, 20um in size. While the conventional Cu powder used for the consolidated samples was not the same as the “fast-raster” powder, it resembled the powder closely. Due to availability and cost, the nano-agglomerate Cu powder was not used in the “fast-raster”.

2.3 Mechanical Properties

Static nanoindentation is performed with the Keysight G200 Nanoindentation System on powder, single-splats, and consolidated cross-sections samples for conventional and nanomaterial copper. Dynamic nanoindentation is performed with an iNano (Nanomechanics Inc) on the consolidated cross-sections for both conventional and nanomaterial copper. For static testing, the machines are equipped with a Berkovich-shaped diamond indenter tip (Micro Star Technologies) and the pre-defined “Express Test for Thin Films Large Table – Batch” was used. For dynamic testing, a spherical diamond based indenter tip (Synton-MDP LTD) with a desired spherical radius of 2.1 um was used with the continuous measurement of stiffness (CSM) option provided by default on all Nanomechanics IIT systems.

All of the nanoindentation samples were mounted prior to testing (see section 2.4). The hardness of the powder was determined after testing 30 different particle cross sections. A 5 x 5 indent array was defined for each of the powder particles and for the consolidated samples. For the static measurement of the conventional Cu single splat and both the static and dynamic measurement of the consolidated conventional and nanomaterial Cu, the coatings were oriented such that the indenter tip was normal to the coating-substrate interface, as seen in Figure 2.

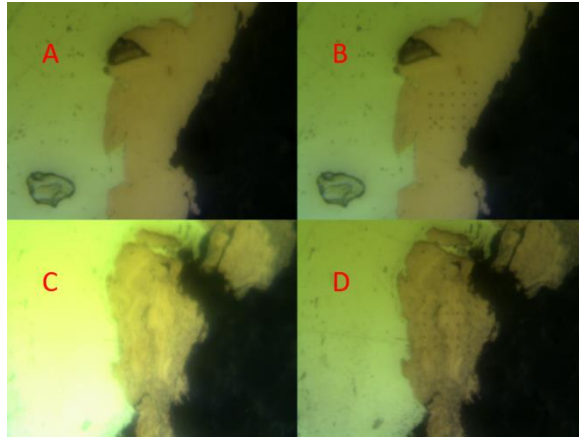


Figure 2: Nanoindentation of A+B) conventional Cu, C+D) nanomaterial Cu

2.4 Microstructural Analysis

For mounted powder and consolidated cross-sections, the Buehler Simplimet 4000 Mounting System was used with phenolic powder (Buehler 20-3200-080) and powdered mold release (Buehler 20-3048). The standard procedure as defined by Buehler was used with heat time of 4 minutes, cool time of 3.5 minutes, pressure of 4400psi, and temperature of 360F. Prior to mounting, consolidated samples were cut using a band saw followed by Worcester Polytechnic Institute's Buehler Center of Excellence IsoMet High-Speed Pro Precision Cutter for a cleaner cut; only the latter was used for the single splat sample. For both the powders and the coatings a 0.05 micron surface finish was achieved using a Struers made Tegramin-20 auto polisher with pads of 1200grit, 3um, and 1um with DP-Suspension-A, followed by colloidal silica suspension (OP-S) used with a MD Chem Polishing Pad. In between each polishing step, the samples were ultrasonically cleaned in ethanol and dried using compressed air.

SEM micrographs were taken of both powder and consolidated cross-sections in a W-source SEM (Zeiss EVO-MA10) at an accelerating voltage of 10 and 15 kV. SEM images of powder were taken from both mounted powder cross-sections and loosely sprinkled powder on double-sided SEM mounting tape. Consolidated samples were cross-sectioned and mounted. Both secondary electron (SE) images and backscattered electron (BSE) images were taken. After initial imaging, samples were etched to reveal the grain structure using a 25% nitric acid-75% DI water solution, then re-imaged. Optical single-splat cross-section images were taken with a Olympus Gx71 Stereoscope. The images were captured using the Stream Essentials image analysis software by Olympus.

2.5 Modelling

The finite element models were developed using Abaqus CAE 2017 (Dassault Systemes). The substrate size was assumed to be 1000x1000x250um to allow modelled stress to propagate freely through without having to modify boundary conditions. Other assumptions include the particle and contact distance, which are placed nearly in contact with the substrate being fixed in the X,Y, and Z directions. The particle was given a predefined velocity and temperature prior to impact. The predefined inputs can be seen in Figure 3 and originate from Penn State University (PSU) simulation software.

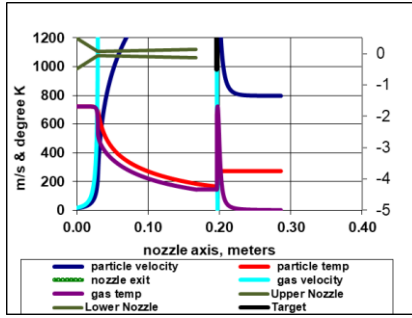


Figure 3: Predefined Model Inputs

For a 25 micron particle sprayed with nitrogen at 450 C and 500 psi (34.47 bar), the estimated particle temperature at impact was 210 C and the estimated velocity at impact was 575 m/sec. These parameters were based on a spray with a VRC Gen3 MAX cold spray system. Model simulation time was set to 1×10^{-7} sec. in order to capture the initial impact and rebound of the particle. Impact data was output at 1×10^{-9} sec for good temporal resolution.

Contact definitions between the particle and the substrate are very important to properly simulate the deformation. The kinematic contact method was used with the finite sliding formulation in Abaqus. The normal impact behavior was set to hard contact, while allowing separation after contact. Both the particle and the substrate are meshed with hexahedral elements, type C3D8RT. Significant partitioning was required in order to mesh the particle with hexahedral elements. The particle contains 896 elements, while the substrate contains 10,404 elements. Figure 4 shows the meshed particle and substrate prior to impact.

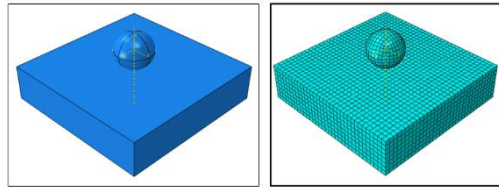


Figure 4: FE Orientation (left) and mesh (right) of particle prior to impact

2.5.1 Johnson Cook

The software used for the JC modeling was Abaqus CAE 2017. The JC equation is shown as Equation 4:

$$(5) \quad \sigma_y = [A + B \varepsilon_p^n][1 + C \ln \dot{\varepsilon}_p][1 - T_H^m]$$

where ε_p is the amount of effective plastic strain in the system and $\dot{\varepsilon}_p$ is the normalized effective plastic strain rate. A, B, and C are experimentally determined material constants, where A is the quasi-steady-state yield stress, B is the power law pre-exponential factor, C is the strain rate pre-exponential factor, n is the strain hardening exponent, and m is the thermal softening exponent. T_H is a normalized temperature, shown as Equation 2:

$$(6) \quad T_H = \frac{(T - T_{room})}{(T_{melt} - T_{room})}$$

Material constants are defined by JC and are shown in Table 1 [15].

Table 1: Johnson Cook Constants

| Young's Modulus | Poisson's Ratio | A | B | C | n | m | Tm | Tref |
|-----------------|-----------------|-------|--------|-------|------|------|-------|------|
| 110GPa | 0.34 | 90MPa | 292MPa | 0.025 | 0.31 | 1.09 | 1356K | 294K |

2.6 PTW Model

The software used for the PTW model is the same as the JC model. The PTW model was implemented into Abaqus using a Fortran VUHARD Subroutine that overrides the standard plasticity models. The PTW equation is shown as Equation 3:

$$(7) \quad \hat{t} = \hat{t}_s + \frac{1}{p} (s_0 - \hat{t}_y) \ln \left[1 - \left[1 - \exp \left(-p \frac{\hat{t}_s - \hat{t}_y}{s_0 - \hat{t}_y} \right) \right] * \exp \left\{ - \frac{p \theta \psi}{(s_0 - \hat{t}_y) \left[\exp \left(p \frac{\hat{t}_s - \hat{t}_y}{s_0 - \hat{t}_y} \right) - 1 \right]} \right\} \right]$$

Material properties were defined by PTW for copper [28]. Each material constant for copper is described in Table 2.

Table 2: Preston-Tonks-Wallace Constants

| θ | p | S_0 | s_∞ | κ | γ | Y_0 | Y_∞ |
|----------|----------|------------|------------|-------------------------------|---|----------|-------------------|
| 0.025 | 2.0 | 0.0085 | 0.00055 | 0.11 | 0.00001 | 0.0001 | 0.0001 |
| Y_1 | Y_2 | β | G_0 | α | α_p | M (na) | C (cm/ μ s) |
| 0.094 | 0.575 | 0.25 | 510 | 0.20 | 0.43 | 63.54 | 0.3933 |
| s | ρ_s | γa | G/B | ρ_0 (g/cm ³) | Γ (10 ⁻⁴ cal/mol K ²) | g | k (cal/s cm K) |
| 1.50 | 8.933 | 2.0 | 0.35 | 9.02 | 1.6 | 2/3 | 1.8 |

3. Results and Discussion

3.1. Modelling

JC and PTW are used to model single particle impact of conventional Cu cold spray powder. The Johnson Cook model outputs a graph of velocity and temperature with respect to time of impact as seen in Figure 5. Initial particle impact starts 3-4ns into each graph and is most easily seen in the velocity graph (5A) as the point at which velocity begins to decrease steadily. The initial impact follows through to the ~45ns mark, at which point the particle becomes fully compressed. A slight increase in velocity after this point indicates some elastic rebound on the nodal level. The temperature graph (5B), shows that there is a continuous temperature increase upon impact due to particle heating from deformation. The temperature band widens over time due to noise attributed to nodal oscillation. In general, as particle velocity decreases on impact, temperature increases.

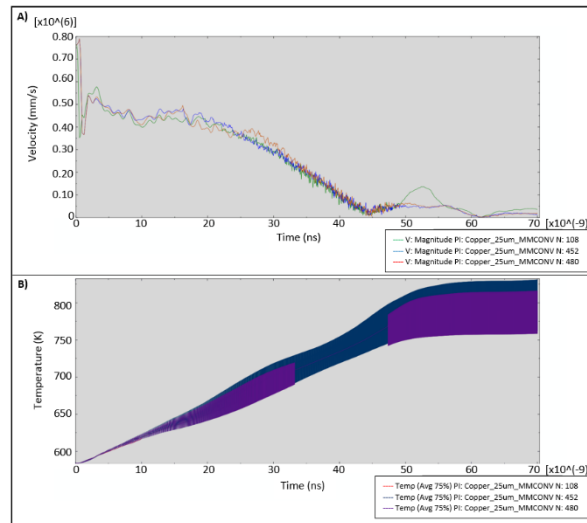


Figure 5: A) Particle Velocity with Respect to Time of Impact, B) Particle Temperature with Respect to Time of Impact

A JC temperature plot of the cross-section of a fully impacted conventional copper particle is modelled in Figure 6.

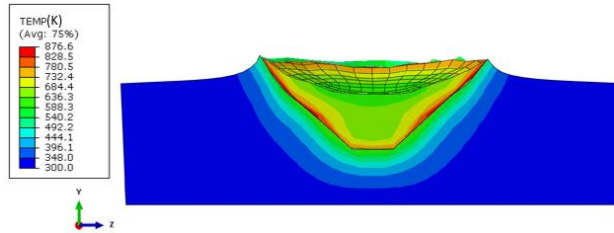


Figure 6: Johnson-Cook, Particle Fully Impacted, Temperature Distribution Plot

This is the temperature profile of the particle at maximum displacement prior to rebound; maximum contact pressure and peak temperature are given at this time. The temperature profile shows significantly higher temperature at the particle/substrate interface than inside the particle. This is supported by the von Mises stress profile following particle impact, shown in Figure 7, where the von Mises stress is highest at the particle/substrate interface. The increase in stress and temperature at the edges of the particle can be attributed to localized plastic deformation due to the high velocity of the particle on impact [38, 18]. This increase in flow at the particle/substrate interface can contribute to jetting, which is shown later on in this section.

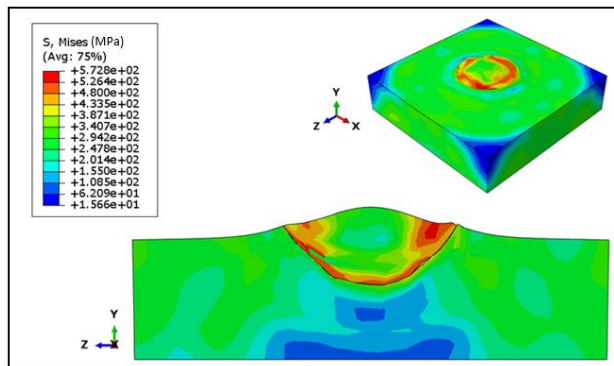


Figure 7: Johnson-Cook, Particle Fully Impacted, von Mises Distribution Plot

JC temperature and stress profiles help pinpoint the conditions needed for metallurgical bonding/melting and subsequent adhesion of the particle to the substrate. Additional work is needed for PTW profiles.

The plastic equivalent strain (PEEQ) profiles at final particle impact for both JC and PTWare shown in Figure 8.

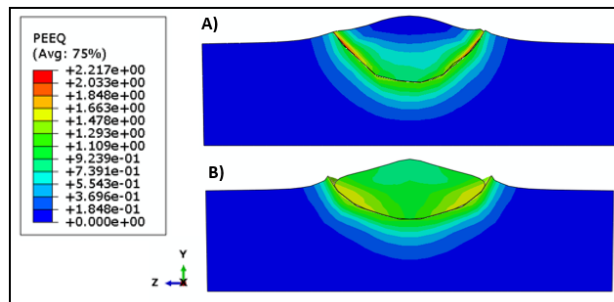


Figure 8: Plastic Equivalent Strain (PEEQ) profile at final particle impact a) JC, B) PTW

Both diagrams show that the residual stress at the particle/substrate interface is larger than in the center of the particle [38]. Since strain shows how much work is put into the particle, PEEQ has a direct relationship to hardness. PEEQ values can be used to calculate flow stress by applying the values to the JC and PTW equations. The Von Mises flow stress values for a fully impacted conventional copper powder particle are 367 MPa and 394 MPa for JC and PTW, respectively. The larger PTW flow stress model correlates well with the PEEQ diagram showing PTW to have greater strain than JC.

The general magnitude of the flow stress values can be validated by applying the modelled PTW strain rate of 1.109 to Hollomon's (power) Law to get a flow stress output of 332MPa. The powder law value is within the same

magnitude of both the PTW and JC values. All three values are close to the values for flow stress of cold worked Cu found in industry [17]. Compared to JC, PTW produces more accurate results. This is because JC is based on a ‘curve fit’ of experimental data from prior work with bulk Al6061 and has homologous input of temperature. Whereas PTW doesn’t rely on experimental data, but does use values based on bulk Cu as the experimental data for single splat Cu is not yet available.

Morphology comparison between JC and PTW is seen in Figures 9 and 10, respectively.

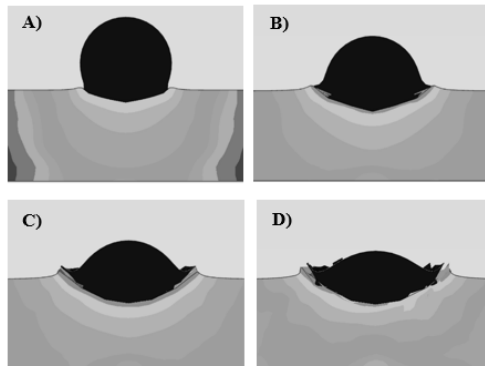


Figure 9: Johnson-Cook Impact Morphology at A) 10ns, B) 20ns, C) 30ns, D) 40ns

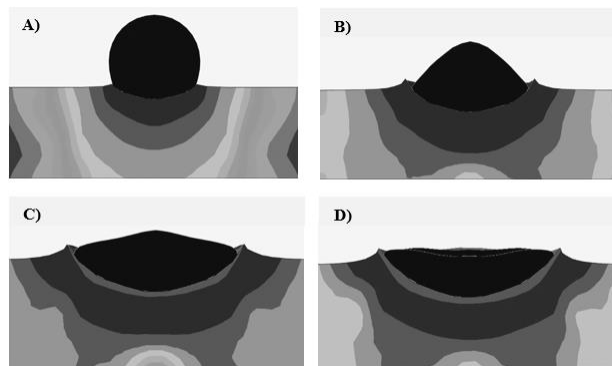


Figure 10: PTW Impact Morphology at A) 10ns, B) 20ns, C) 30ns, D) 40ns

The JC model from A-D shows: A) initial particle impact, B) plastic deformation at the particle/substrate interface, C) The zone of high strain at the particle/substrate interface is plastically extruded to form a jet, D) the continued downward momentum of the particle propels the jet up along the edges of the particle/substrate interface. [10,19, 38]

By frame D the jet edges get sharp and begin to dissipate. This is a reflection on the limits of the Johnson-Cook model. PTW shows similar morphology but has more degrees of freedom to overcome the resolution issues faced in JC. However, both are mesh-based-constant volume models and more development is needed to model more complex powder structures like the nano-agglomerate Cu powder.

3.2. Mechanical Data

Static and dynamic nanoindentation test data for powder, single-splats, and consolidated conventional and nanomaterial copper are listed in Table 3.

Table 3: Static Nanoindentation Hardness Measurements and Flow Stress Calculations

| | Measured Static NI Hardness (GPa) | Calculated VHN (MPa) | Calculated YS (MPa) | Calculated UTS (MPa) | Calculated Flow Stress (MPa) |
|------------------------------|-----------------------------------|-------------------------------|------------------------------|-------------------------------|---------------------------------|
| | - | $VHN = 0.0945 \cdot NI$ (MPa) | $YS = 2.874 \cdot VHN$ (MPa) | $UTS = 3.353 \cdot VHN$ (MPa) | $Flow\ stress = (YS + UTS) / 2$ |
| Cu Single-Splat | 2.03 | 191 | 548 | 640 | 594 |
| Conventional Cu Powder | 1.31 | 123 | 353 | 412 | 382 |
| Nano-agglomerate Cu Powder | 1.21 | 114 | 327 | 382 | 354 |
| Consolidated Conventional Cu | 1.75 | 165 | 474 | 553 | 513 |
| Consolidated Nanomaterial Cu | 2.41 | 226 | 649 | 757 | 703 |

The nano-hardness value for the single splat is greater than that of the powder and consolidated conventional Cu values. This may be due to the use of different powder in the single-splat experiment. While the powder was made of pure Cu and gas atomized, it is possible that the gas used in the process affected the end powder microstructure, making the powder harder [1,35]. In Figure 5 there is a notable increase in temperature from particle friction and impact with the substrate. This increase in temperature coupled with the mechanical stress on impact can affect recrystallization and subsequent hardness values [37]. It is possible that recrystallization from plastic deformation would have a greater effect on a single particle than a coating due to the effects of thermal softening from multi-particle impacts [29,39]. The effect of oxides, vacancies, and jetting can also be considered when comparing the lower nano-hardness value of the consolidated material to that of the single-splat.

The nano-hardness value for the nano-agglomerate Cu powder is less than the conventional Cu powder. This is from the difference in powder processing, where the nano-agglomerate is spray-dried and the conventional Cu powder is gas atomized. For the spray dried powder it is possible that the nano particles encapsulated by a Cu binder are not bonded as well and that there is greater porosity as compared to the conventional Cu powder.

The nano-hardness of the consolidated nanomaterial Cu is much greater than the consolidated conventional Cu. The cold spray process can cause powders to compress on impact, creating denser coating than the initial powder. This densification is largely due to the effects of work hardening from the tampering or shot peening effect of high velocity powder particles on impact as they build up on each other [14].

The calculated flow stress from the nano-hardness measurements for the single splat is much greater than the modelled values. As mentioned in the above paragraphs, this is most likely due to the difference in powder used for the single splat as compared to the model inputs. In addition, the empirical formula used is based on bulk cold worked Cu and is likely a contributing factor to the high powder and single-splat calculated flow stress values [20].

The consolidated values are much higher than the model as well, however this is to be expected considering the above mentioned factors. When comparing consolidated conventional Cu to nanomaterial Cu, the latter has a greater hardness and subsequent flow stress values. The same relationship is true for the dynamic nanoindentation results, seen in Table 4.

Table 4: Dynamic Nanoindentation Hardness and Mechanical Measurement

| | Measured Dynamic NI Hardness (GPa) | Modulus (GPa) |
|------------------------------|------------------------------------|---------------|
| Consolidated Conventional Cu | 1.79 | 62.92 |
| Consolidated Nanomaterial Cu | 2.48 | 61.3 |

The nanomaterial Cu has greater hardness than conventional Cu due to its smaller grain size as supported by the Hall-Petch relationship, which states that grain-boundary strengthening, and subsequent material yield strength, increases with decreasing grain size [5].

In accordance with the developments made by Pathak, Shaffer, and Kalidind [27], representative indentation stress-strain curves can be developed using the measured modulus from dynamic nanoindentation; results are shown in Figure 11.

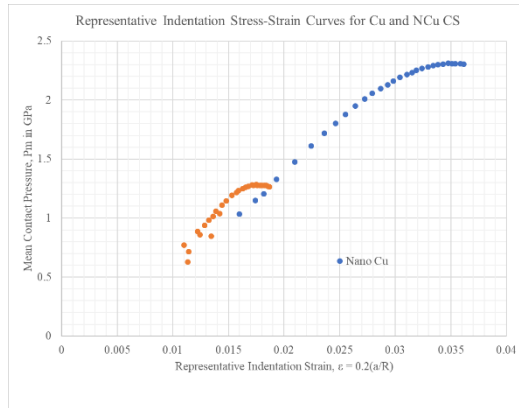


Figure 11: Calculated stress-strain curves for consolidated nanomaterial and conventional Cu from dynamic nanoindentation data.

The data shows an increase in YS and UTS for the nanomaterial Cu as compared to conventional Cu. Further calculations provide a flow curve for the nanomaterial and conventional Cu data set in Figure 12. Calculations were modified from Leitner [23] with additional information on calculations found in the APS March 2019 proceedings [33]. Note that the beginning of the conventional Cu graph has some noise due to strain hardening and the dip towards the end is analogous to the trend known as necking in tensile testing.

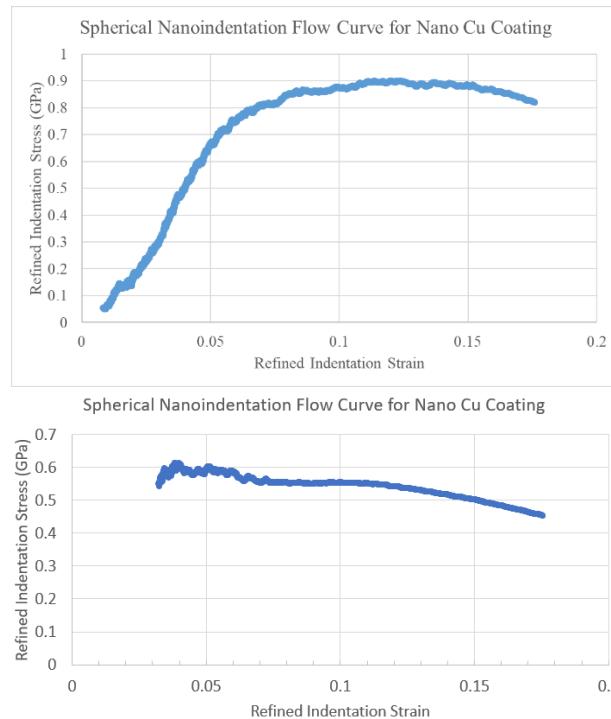


Figure 12: Calculated flow stress for consolidated nanomaterial Cu (top) and conventional Cu (bottom) from dynamic nanoindentation data.

Considering the 2% offset, the yield strength is measured from Figure 12 as 850 MPa and 590MPa for nanomaterial and conventional Cu, respectively. The nanomaterial and conventional copper flow stresses derived from dynamic nanoindentation data are significantly higher than that of the static nanoindentation measurement and subsequent calculations for conventional Cu flow stress. The difference in values is most likely due to 1) the nanoparticles present in the nanomaterial Cu and 2) because the static nanoindentation work looked at just the single-splat particle whereas the dynamic nanoindentation and flow stress calculation were based on a cross-section or multi-particle impact. Despite the difference in magnitude between the static and dynamic flow stress calculations, the data is consistent in showing nanomaterial Cu to have a greater flow stress than conventional Cu. Additional work is needed to model both the nanomaterial copper and multi-particle impact scenarios.

3.3 Microstructure

Microstructural analysis is used to validate the measured hardness values, as well as the impact morphologies from the models. A cross-section of both the conventional and nanoagglomerate powder is shown in Figure 13.

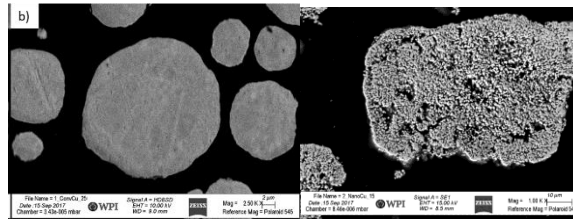


Figure 13: A) Conventional Cu Powder B) Nanomaterial Cu Powder

There is a clear difference in microstructure between the two powders, specifically with the nano-agglomerate powder showing much smaller particles within the powder structure. The consolidated conventional and nanomaterial copper powder can be seen in Figure 14.

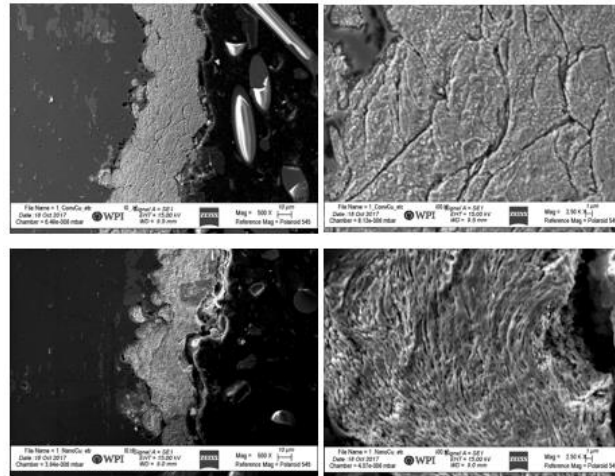


Figure 14: Top- etched consolidated conventional Cu cross-section, Bottom- etched consolidated nanomaterial Cu cross-section

The conventional copper shows much larger grains than the nanomaterial copper. The decrease in grain size of the nanomaterial Cu allows for validation of the higher hardness values through the Hall-Petch relationship, where smaller grains are linked to increases in material strength. [12]

To appreciate the complimentary nature between the modeled impact and produced single-splat, Figure 15 couples the FE simulation output impact morphology for conventional Cu powder with the experimentally obtained single particle impact morphology.

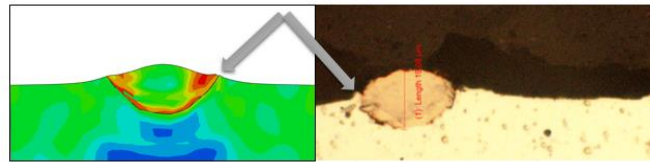


Figure 15: model (left) and single splat (right) of conventional Cu powder particle impact

This shows the once spherical powder particle has elongated perpendicular to the direction of impact [17]. The two arrows in Figure 15 highlight the comparable jetting observed computationally and experimentally.

Magnification of the coating/substrate interface in Figure 16 allows for comparison of the jetting phenomena between the copper cold spray coating, single splat, and particle impact model.

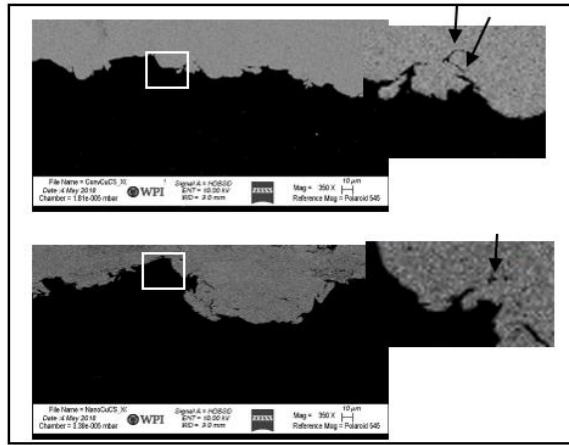


Figure 16: Top- Conventional Copper with zoom to show jetting as indicated by the arrow, Bottom- same but for nanomaterial Cu

In both Figure 16 and 17 it can be seen that the particles are no longer spherical and are compressed parallel to the substrate. At the particle/substrate interface the characteristic mixing of the cold spray process is evident. It is more difficult to see jetting in consolidated coatings due to the high degree of plastic deformation and particle impact which often degrades the jet structure. Magnifying that interface, one can see folded particles and in some cases the darker thicker lines around those particles as remnants of jetting, indicated by the arrows in Figure 16. [21, 3, 36]

Knowing the grain structure of copper cold spray coatings not only allows for validation of the model and hardness measurements, but also provides a stepping stone for future modelling of nanomaterial copper [30].

4. Conclusion

JC and PTW models were used to determine morphology and flow stress outputs for single-splat conventional Cu powder. Hardness values and microstructure images were taken to validate the model. The conclusions of this work are as follows:

[1]The JC and PTW model outputs for flow stress are of the same order of magnitude as Holoman’s (power) law calculation and industry measurements for cold worked Cu.

[2] The JC and PTW model morphology is consistent with that of the optical images of the single-splat particle. Jetting can be seen in both the single-splat and consolidated micrographs.

[3] PTW is more accurate than JC for both flow stress and morphology outputs, as it is based on thermodynamics and uses inputs from bulk Cu standards as opposed to experimental data.

[4] Static and dynamic nanoindentation show consolidated nanomaterial Cu hardness to be greater than conventional Cu, as supported by Hall-Petch and micrographs.

[5] Calculated consolidated flow stress values from nanoindentation data are much greater than powder and single-splat values. Powder and single-splat flow stress values are greater than expected and do not correlate directly to the modelled values. This is largely due to the assumptions made in the empiric formula.

[6] From prior work [34], there is a relationship between hardness values and antimicrobial properties. This paper supports the results from efficacy testing showing nanomaterial Cu to have greater antimicrobial effectiveness than conventional Cu.

This work sets a baseline for optimization of the cold spray process for improvement of antimicrobial copper coatings. Further work is needed to perfect dynamic nanoindentation testing to take measurements of single-particle impact and of the powder, which can then be used as inputs in PTW for a more accurate model of conventional Cu powder impact. Additional work is also needed to develop the PTW model for single-particle impact of nano-agglomerate Cu powder and for multi-particle impacts.

Acknowledgement

Thank you to Chris Massar for the insightful comments in review of this paper.

References

- [1] Antipas G. "Gas Atomization of Aluminium Melts: Comparison of Analytical Models". *Metals* 2012, 2, 202-210
- [2] Askeland D, Fulay P, Wright W. "The Science and Engineering of Materials". (6th ed), USA: Cengage Learning, p. 293, 2011.
- [3] Borchers C, et al., "Microstructural and macroscopic properties of cold sprayed copper coatings". *Journal of Applied Physics*. 93 (2003) 10064-10074.
- [4] Callister, Jr., William D (2005), *Fundamentals of Materials Science and Engineering* (2nd ed.), United States of America: John Wiley & Sons, p. 199, ISBN 978-0-471-47014-4
- [5] Callister, Jr., William D. *Materials Science and Engineering: An Introduction*, Publisher: Wiley , Print ISBN: 9781119278566, 1119278562, Edition: 10th , Copyright year: 2018
- [6] Casey, A. L., et al. 2010. Role of copper in reducing hospital environment contamination. *J. Hosp. Infect.* 74:72–77.
- [7] Champagne, V.; Helfritsch, D. A Demonstration of the Antimicrobial Effectiveness of Various Copper Surfaces, *Journal of Biological Engineering* 2013, 7:8 <https://doi.org/10.1186/1754-1611-7-8>
- [8] Courtney, Thomas. *Materials Science and Engineering: Mechanical Behavior of Materials*. New York: Waveland Pr Inc, 2nd ed, 2000 [LIT] Copper Cold Drawn. MATWEB. Feb 16, 2019. <http://matweb.com/search/datasheet.aspx?MatGUID=1980eb23287a4408adc404dd39293942>
- [9] Espirito Santo, C., N. Taudte, D. H. Nies, and G. Grass. 2008. Contribution of copper ion resistance to survival of *Escherichia coli* on metallic copper surfaces. *Appl. Environ. Microbiol.* 74:977–986.
- [10] Grujicic M, et al., "Adiabatic shear instability based mechanism for particle/substrate bonding in the cold-gas dynamic-spray process". *Materials and Design*. 25 (2004) 681-688.
- [11] Grujicic M, et al. "Computational analysis of the interfacial bonding between feed-powder particles and the substrate in the cold-gas dynamic-spray process". *Applied Surface Science*. 219 (2003) 211-227.
- [12] Hansen, Niels. Hall-Petch Relation and Boundary Strengthening. *Scripta Materialia* 51 (2004) 801–806.
- [13] Hay J. "Introduction to Instrumentation Testing". Society for Experimental Mechanics. *EXPERIMENTAL TECHNIQUES* November/December 2009
- [14] Jenkins R, et al, "New insights into the in-process densification mechanism of cold spray Al coatings: Low deposition efficiency induced densification". *Journal of Materials Science & Technology* 35 (2019) 427–431

- [15] Johnson, G.R. and Cook, W.H. (1983) A Constitutive Model and Data for Metals Subjected to Large Strains, High Strain Rates, and High Temperatures. Proceedings 7th International Symposium on Ballistics, The Hague, 19-21 April 1983, 541-547.
- [16] Johnson G., Cook W., "Fracture Characteristics of Three Metals Subjected to Various Strains, strain rates, temperatures and pressures". Engineering Fracture Mechanics Vol. 21, No. 1, pp. 3148. 1985
- [17] Kim Y, et al., "Microstructure and room temperature compressive deformation behavior of cold-sprayed high strength Cu bulk material". Journal of Thermal Spray Technology. 26 (2017) 1498-1508
- [18] King P, et al., "An experimental and finite element study of cold spray impact onto Two aluminum substrates". Journal of Thermal Spray Technology. 19 (2009) 620-634
- [19] King P, Zahiri S, Jahedi M. "Microstructural Refinement within a Cold Sprayed Copper Particle". The Minerals, Metals, and Materials Society. 40A (2009) 2115-2020
- [20] Krishna S, et al., "On the Prediction of Strength from Hardness for Copper Alloys". Journal of Materials. 2013.
- [21] Lee C, Kim J, "Microstructure of Kinetic Spray Coatings: A review". Journal of Thermal Spray Technology. 24 (2014) 592-610.
- [22] Lee F, Wang D, Chen L, Kung C, Wu Y, et al. (2013) Antibacterial nanostructured composite films for biomedical applications: microstructural characteristics, biocompatibility, and antibacterial mechanisms. Biofouling 29: 295-305.
- [23] Leitner A, Maier-Kiener V, Kiener D. (2018) Essential refinements of spherical nanoindentation protocols for the reliable determination of mechanical flow curves. Materials and Design 146: 69-80
- [24] Noyce JO, Michels H, Keevil CW (2007) Inactivation of influenza A virus on copper versus stainless steel surfaces. Appl Environ Microbiol 73: 2748-2750.
- [25] Oliver W, Pharr G. "An improved technique for determining hardness and elastic modulus using load and displacement sensing indentation experiments". Journal of materials research 7 (6), 1564-1583
- [26] Broitman E. "Indentation Hardness Measurements at Macro-, Micro-and Nanoscale: A Critical Overview". Tribol Lett (2017) 65:23
- [27] Pathak S, Kalidinidi S, (2015) Spherical nanoindentation stress-strain curves. Materials Science and Engineering 91: 1-36
- [28] Preston D, et al., "Model of Plastic Deformation for Extreme Loading Conditions", Journal of Applied Physics. 93 (2003)
- [29] Rokni M, Widener C, Champagne V. "Microstructural Evolution of 6061 Aluminum Gas-Atomized Powder and High-Pressure Cold-Sprayed Deposition". Journal of Thermal Spray Technology.(2013) 23:514–524
- [30] Schmitt M, et al., "Development and Optimization of Tailored Composite TBC Design Architectures for Improved Erosion Durability". Journal of Thermal Spray Technology. 26 (2017) 1062-1075.
- [31] Schreiber J, "Finite Element Implementation of the Preston-Tonks-Wallace Plasticity Model and Energy Based Bonding Parameter for the Cold Spray Process". Pennsylvania State University. 2016.
- [32] Sever N, et al., "Determining flow stress curve with yield and ultimate tensile strengths". Stamping journal. July/August 2011.
- [33] Sousa, Bryer, et al., *Proceedings of the American Physical Society Boston Chapter Meeting, March 4-8 2019*: Abstract: R04.00014: Spherical Nanomechanical Characterization of Novel Nanocrystalline Cu Cold Spray Manufactured Materials. APS, 2019.
- [34] Sundberg K, Champagne V, McNally B, Helfritsch D, Sisson R (2015) Effectiveness of Nanomaterial Copper Cold Spray Surfaces on Inactivation of Influenza A Virus. J Biotechnol Biomater 5: 205.

- [35] Unal A. "Effect of processing variables on particle size in gas atomization of rapidly solidified aluminium powders". Materials Science and Technology 3(12):1029-1039
- [36] Venkatesh L, Chvan N, Sundararajan G, "The Influence of Powder Particle Velocity and Microstructure on the Properties of Cold Sprayed Copper Coatings". Journal of Thermal Spray Technology. 20 (2010) 1009-1021.
- [37] Villafuerte J. "Modern Cold Spray: Materials, Processes, Applications". Springer: Ontario, Canada. 2015.
- [38] Wenya L, et al., "Residual stress analysis of cold-sprayed copper coatings by numerical simulation". Journal of Thermal Spray Technology. 15 (2015) 31-142.
- [39] Yin S, et al. "Deposition behavior of thermally softened copper particles in cold spraying". Acta Materialia 61 (2013) 5105–5118.

5. Paper #3: Microstructural Characterization of Conventional and Nanomaterial Copper Cold Spray Coatings

Microstructural Characterization of Conventional and Nanomaterial Copper Cold Spray Coatings

Kristin Sundberg^{1*}, Caitlin Walde², Bryer Sousa³, Swetaparna Mohanty, Jae-Hwang Lee, Richard Sisson, and Danielle Cote

^{1,2,3} Materials Science and Engineering, Worcester Polytechnic Institute, Worcester, MA, USA

*Corresponding author: kristinsundberg7@yahoo.com

Abstract The microstructure of conventional and nanomaterial Cu cold spray coatings is explored to understand why nanomaterial Cu cold spray performs better than conventional Cu cold spray in the contact killing of Influenza A Virus ^[19]. Powder, single-splats from laser induced projectile impact testing (LIPIT), and consolidated cold spray coatings are imaged using Scanning Electron Microscopy (SEM). Sample composition is confirmed using Energy Dispersive X-Ray Spectroscopy (EDS) and X-ray Diffraction (XRD). Results show nanomaterial Cu to have a much smaller grain size than conventional Cu. Nanoindentation is used to confirm microstructural differences, showing nanomaterial Cu to have greater hardness. LIPIT and consolidated cross-sections identified grain refinement at the particle-substrate interface for both nanomaterial and conventional Cu. Follow-on work with corrosion testing will be performed to better understand Cu ion release rate in relation to the differing material microstructures for antimicrobial applications.

Keywords: *cold spray, nanomaterial, copper, antimicrobial, grain refinement, work hardening*

1. Background

Microstructural characterization of conventional and nanomaterial Cu coatings is done in support of prior work in the paper, “Effectiveness of Nanomaterial Copper Cold Spray Surfaces on Inactivation of Influenza A Virus”, where it was found that nanomaterial Cu had greater antimicrobial effectiveness than conventional Cu ^[19]. Understanding microstructural changes in powder, single-splat, and consolidated Cu cold spray will help to better determine Cu kill mechanisms and to further optimize Cu antimicrobial properties for future coatings.

Cold spray coatings have a distinct bonding at the particle/substrate interface, which contributes to its strong adhesive properties ^[7]. For a strong bond to occur in a single-splat, the particle impact velocity must exceed a critical value and the particle cooling rate should be low enough for shear instability/localized deformation, but also high enough for cooling of the bond to occur ^[18,24]. Factors affecting this include the material, powder quality, size, shape, impact temperature, and velocity ^[16]. One of the reasons why nano-agglomerate copper powder is used instead of nano particles is because nano particle diameters are too small for shear instabilities as their thermal gradient/cooling rate is too high ^[19]. For copper cold spray, the critical diameter, or minimum diameter for particle/substrate adhesion is 10 μm 's ^[16]. For this work, the average particle size of conventional and nano-agglomerate Cu powder is -31/+5 and 25 μm 's, respectively ^[19].

The critical impact velocity (V_c) for a given particle size can be predicted using modelling techniques ^[21] or with trial and error, as is the case of the Laser Induced Projectile Impact Testing (LIPIT) performed in this paper. LIPIT is able to impact individual powder particles on a substrate at varying velocities to determine the ideal velocity for increased adhesion and reduced particle rebounding. LIPIT can provide information on impact mechanics, showing the strong dependence of compressive shock on the characteristic cold spray ‘mixing’ at the interface and ‘jetting’ at the particle-substrate surface. ^[MIT]

Due to the relatively low temperatures of cold spray (100-600°C), a high impact velocity (600-1000 m/s) is needed for good adhesion. This increase in velocity results in high plastic deformation which can cause dynamic recrystallization, producing ultra-fine-grain (UFG) structures at particle-particle and particle-substrate interfaces. Dynamic recrystallization occurs from high shear due to plastic deformation or from mechanical stress where rotational dynamic recrystallization may occur. Material properties can affect UFG development through

recrystallization, where a decrease in thermal conductivity increases heat retention, increasing the potential for recrystallization. [10, 12, 16, 13, 23]

Upon impact, interface mixing is dependent on substrate and powder hardness and density. A hard metal impacting a softer metal would have a deeper imprint with less spreading than a soft metal on a hard substrate. In the case of Cu and Al, both are soft metals, with Cu having slightly higher density. The depth of impact is amplified by the copper particle being heavier and having a larger amount of kinetic energy than that of the Al substrate. Also, soft metals have a greater temperature region from high ductility and thermal softening, which contributes to the spreading of the particle on impact. [24, 7]

The same characteristic mixing discussed above applies to cold sprayed nanomaterial Cu coatings [19]. In some cases, nano-particles can have partial devitrification of their amorphous phase, but in most cases the nano structure is retained [16].

Cold spray is known to have very few oxides/impurities/inclusions in the bulk coating, this is due to the quality of the powder, but also to the peening effect. When the particles are sprayed, the impact against the substrate breaks up oxides, which are then carried up the surface with the interfacial jet [24]. Work with EDS and XRD can confirm powder and coating purity.

Hardness measurement can be used to predict cold spray microstructural properties in powder and consolidated coating using the Hall-Petch relationship, which states that grain-boundary strengthening, and subsequent material yield strength, increases with decreasing grain size [2]. Hall-Petch is commonly used in the micrometer range but has also been demonstrated for nanocrystalline metals ranging 20-100nm [8]. It appears that the relation holds true for consolidated nanomaterial Cu cold spray, which has much greater hardness values and much smaller grains than that of conventional Cu cold spray [19]. There is a direct relationship between Cu material hardness and antimicrobial properties [19]. The effect of microstructure on end material properties is key in understanding why nanomaterial Cu is more effective at contact killing of Influenza A virus than conventional Cu.

2. Test Procedure

2.1. Cold Spray

Cold spray samples from the first paper, "Effectiveness of Nanomaterial Copper Cold Spray Surfaces on Inactivation of Influenza A Virus" [19], were used. The pure Cu cold spray coatings on aluminum substrates are approximately 0.05 mm thick. The nano copper (Eltron) was produced by spray drying and the conventional copper (Praxair Cu-159) through gas atomization. Due to the low mass of the nano-particles, they are bound into agglomerates using conventional Cu as the binder and spray dried [15, 19]. For more information on the materials and cold spray process parameters see reference 19.

2.2. Laser Induced Projectile Impact Testing

2.2.1. μ -Projectile and Target Substrate Preparation

PDMS (Sylgard 184, Dow Chemical) with a mixing weight ratio of 1:10 was spin coated onto an ~80 nm thick Au coated glass substrate (Fisherbrand™ Cover Glasses No. 2) [1]. They were further cured at 200°C for 1 hr. Nano-agglomerate Cu powder and conventional Cu powder with particle diameter of approximately 15-20 μ m were used for the experiments. The particles were applied to the surface of the PDMS/Au coated glass substrate using a brush. High purity Al target substrates (5mm x 5mm) were electropolished and used for the experiments. The electrolyte solution used was a mixture of Perchloric acid (70% Perchloric acid Sigma-Aldrich) and Ethanol (Sigma-Aldrich) in volume ratio of 1:5. During the process, the electrolyte bath temperature range was maintained in between 5 °C to 8 °C and the electropolishing was carried out at 15V for a duration of 10 minutes.

2.2.2. High Strain Rate Single Particle Experiments

Acceleration of the micron scale particles to supersonic velocities was achieved by using Laser-induced projectile impact test (LIPIT) technique^[25,4]. Briefly described, a Nd:YAG laser (Quanta-Ray INDI-40-10-HG, Spectra-Physics) was used to create an ablation laser pulse (5-8 ns pulse duration; 1064 nm)^[25]. Following the laser ablation of the Au film after trigger, the PDMS film expands and the selected particle that was positioned at the focus point of the ablation laser accelerates towards the target (Fig 1). Simultaneously for illumination, a Ti:Sapphire oscillator (Mai Tai HP, Spectra-Physics) provided continuous laser pulses of pulse duration <100 fs ($\lambda=750$ nm). A 500MHz oscilloscope (GDS-3504, Instek) was used to measure the pulse repetition rate (79.56 MHz). The laser pulses were gated by electro-optical modulators, and converted to white light by a photonic crystal fiber (SCG-800, Newport) to capture diffraction-suppressed ultrafast micrographs^[25]. The real time pre and post impact events were captured using a low-noise and high-quantum-yield digital camera (C11440-22C, Hamamatsu Photonics). Impact (V_i) and rebound (V_r) velocities were calculated by measuring the distance covered by the particle in the given period (images interframe time). The microparticles adhere to the target substrate after crossing the threshold velocity named as critical impact velocity. The critical velocity was also determined for each type of Cu powder ($V_r=0$).

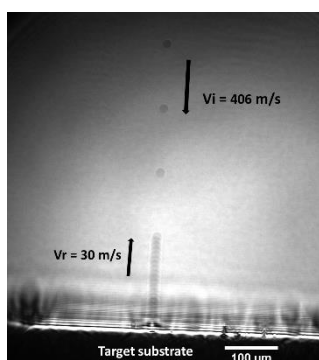


Fig 1. The collision and rebound of a Praxar Cu particle with the HP- Al target substrate.

2.2.3. Characterization

The analysis of the cross section and high-resolution SEM of the sample was performed by a Dualbeam FIB^[14] (Thermo Fisher Scientific Strata 400S). A $\sim 2\mu\text{m}$ layer of Platinum was deposited on the surface of the sample prior to FIB. After a fine milled surface was achieved following cross sectioning, the immersion mode SEM images were taken at a tilt angle of 52° .

2.3 Microstructural + Composition Analysis

2.3.1. SEM

SEM was used to analyze the microstructure of both loose powders as well as the cold sprayed parts. Samples were mounted in metallurgical epoxy mounts, then mechanically polished to a $0.05\mu\text{m}$ finish for analysis. Two orientations were studied – cross-section as well as top-down. SEM analysis was performed in a Zeiss EVO MA-10 and in the Joel JSM-7000F FE SEM at an accelerating voltage of 10 and 15 kV with both backscatter (BSE) and secondary (SE) electron detectors. Samples were then etched in 50/50 Ni/DI H₂O for 15 seconds and 25/75 Ni/DI H₂O for 5 seconds for conventional and nanomaterial Cu respectively, and re-imaged.

2.3.2. EDS

EDS was performed using BrukerNano GmbH with the Zeiss SEM for cross-sectioned powder. Oxford Instruments X-Max^N was used with the JEOL 7000 FE SEM for cross-sectioned consolidated samples. Software ran for 5minutes prior to data collection, and dead time ranged from 2-5%. A rate of 20 kilocounts was used for the SEM and ~ 3000 counts per second for the FE SEM.

2.3.3. EBSD

EBSD analysis was performed at 25 kV in a FE-SEM (JEOL 7000F) with an NordlysMax² detector (Oxford). Data was collected for cross-sections of powder, consolidated, and top-down polished consolidated samples. Step sizes used were 0.1 μ m and 0.316 μ m for nano-agglomerate and conventional Cu powder, respectively. Since the step size for the nano-agglomerate powder was so small, data was collected for only part of the grain. Consolidated nanomaterial Cu ran an area of 6 μ m \times 4 μ m with a step size of 0.1 μ m for 1h and 20min. Consolidated conventional Cu ran an area of 10.5 μ m \times 2 μ m with a step size of 0.1 μ m for 1h 20min, but this data was too charged and the beam was rastering empty space. Data was collected again using a 0.316 μ m step size for 20min; this data is present in the paper.

Consolidated samples were prepped the same as for SEM, then a final polish using an Ar-ion mill at 6kV was performed to remove any surface stresses. Powder was mounted on carbon paint on a silicon wafer and then cut down in half using a JEOL argon cross-section polisher at 6kV for 2 hours. Mounted powder was flipped sideways in the cross-section polisher to cut powder in half.

2.3.4. XRD

WPI's PANalytical Empyrean X-ray Diffraction machine was used with a Cu tube and Ni filter from 20 to 140 2theta at 45Kv and 40Ma, with a 1/2 degree divergence slit, 1 degree anti-scatter slit, 0.04 radian soller slit, 10mm mask, and a time per step of 10. Prior to running, the depth was checked with a goniometer and a depth of 1 was confirmed.

Results were collected and analyzed using DataViewer and HighScore Plus software. Results were compared against reference PDF4database, with PDFs 00-004-0836, 00-005-0061, 00-005-0667 for Cu, CuO, and Cu₂O, respectively.

2.4 Mechanical Analysis

Static nanoindentation is performed using iMicro by Nanomechanics Inc. Consolidated top-down nanoindents are made for both conventional and nanomaterial Cu CS. A Berkovich-shaped diamond indenter tip (Micro Star Technologies) and pre-defined "Express Test for Thin Films Large Table – Batch" was used. All of the nanoindentation samples were mounted prior to testing (see section 2.3.1). 5 x 5 indent array was defined for each of the samples.

3. Results and Discussion

3.1. Powder Microstructure

SEM images of conventional and nano-agglomerate Cu powder are shown in Figure 2.

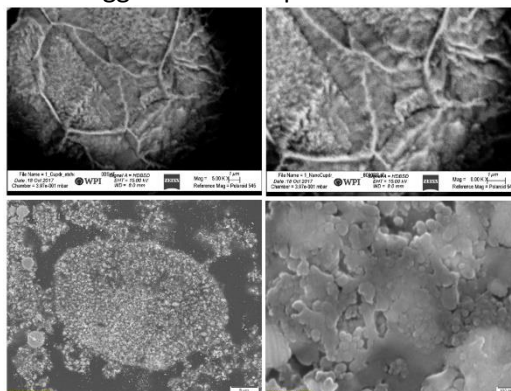


Figure 2: SEM backscatter micrographs of etched conventional Cu powder particle (top). FE SEM micrographs of etched nano-agglomerate Cu powder (bottom)

The conventional powder has much larger, micron-scale grains as compared to the nano-agglomerate powder. The nano particles present in the nano-agglomerate powder range from 60-80nm and are amorphous. A

micrograph of the nano particles can be found in supplemental section C. EBSD analysis in Figure 3 supports the above observations.

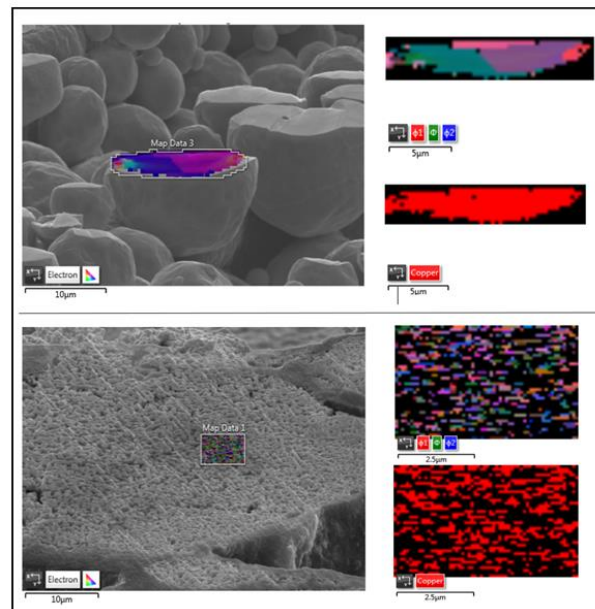


Figure 3: EBSD cross-sections of Conventional Cu powder (top) and Nanomaterial Cu powder (bottom)

EBSD shows a difference between the conventional and nano-agglomerate powder where the latter has much finer microstructure and greater porosity. Due to the porosity of the sample, it is difficult for EBSD to provide a clear image for grain size of the nano-agglomerate powder. Percent porosity of the powder is further detailed in the pre-impact micrograph in section 3.2.

The nano-agglomerate powder grains are smaller and have more changes in orientation than the conventional Cu powder. For conventional Cu there is a range of powder sizes made evident by the different phase orientations, where grains range from below 1µm to above 10µm.

When looking at the etched conventional Cu powder samples, it appears that the grains are well defined in the 5-10µm range. However, based on the range of grain sizes shown in EBSD, it is possible that only the high angle grain boundaries are visible in the etched sample [26].

3.2. Laser Induced Projectile Impact Test

A pre-impact micrograph of the nano-agglomerate powder is shown in Figure 4. The powder is fabricated by spray drying nano-agglomerates of nano Cu particles held together by a pure Cu binder. The spray drying process in combination with the use of nano particles produces significant powder porosity as compared to the gas atomization process for conventional Cu powder.

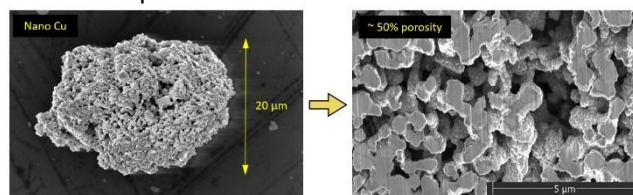


Figure 4: Micrograph of nano-agglomerate Cu powder porosity.

Varying the particle size during Laser Induced Projectile Impact Testing (LIPIT) allows for a determination of the critical velocity. A breakdown of the dependence of particle size on velocity for both conventional and nano-agglomerate Cu powder impacting an Al substrate is detailed in Figure 5.

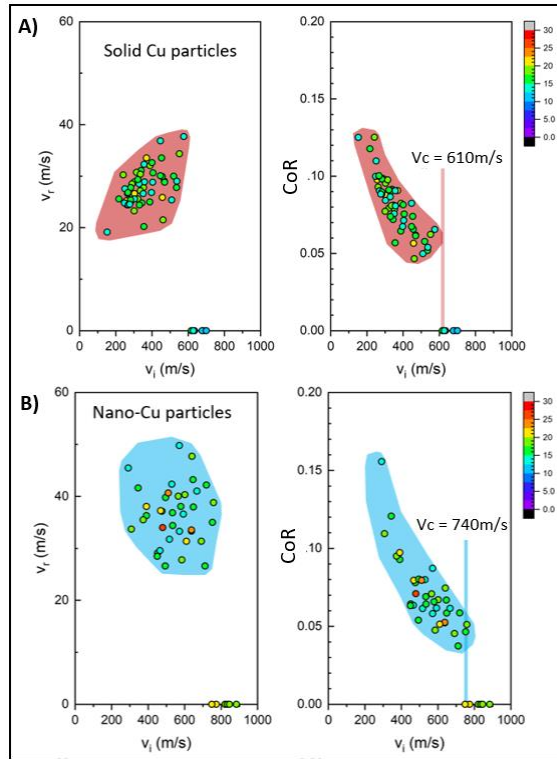


Figure 5: Rebound Velocity and COR vs. Impact Velocity for A) Conventional (Solid Cu), B) Nano-agglomerate Cu (Nano Cu) powder

Where, V_i is impact velocity, V_r is rebound velocity, V_c is critical velocity, and CoR is impact speed/rebound speed. V_c serves as the point at which initial velocity increase causes no particle rebound [9]. V_c for nano-agglomerate and conventional Cu powder with a size of 15-20 μ m is 740m/s and 610m/s, respectively. Critical velocity of the conventional Cu powder correlates well to similar work done in the field [9]. Nano-agglomerate Cu powder has a greater critical velocity from the contribution of increased porosity to particle density. The differences between the two samples can be seen in Figure 6, where data from Figure 5 was taken and combined onto the same graph.

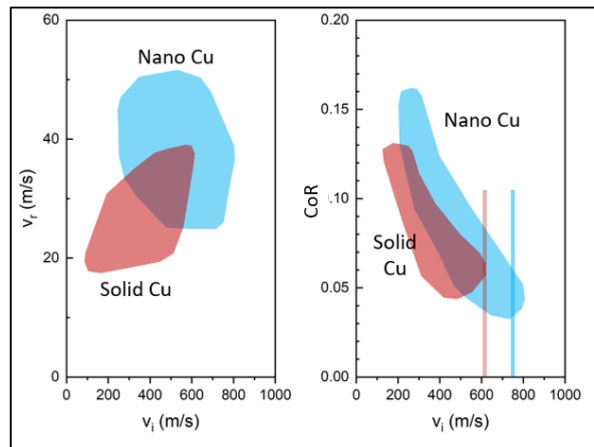


Figure 6: Rebound Velocity and COR vs. Impact Velocity for Conventional (solid Cu) and Nano-agglomerate Cu (Nano Cu) powder

Once a minimum V_c is determined, the 15-20 μ m powder particles are selected and sprayed at 701m/s for conventional Cu, and 770 m/s and 884 m/s for nano-agglomerate Cu powder. Micrographs of the particle impacts are shown in Figure 7. In all cases, the once spherical powder grains appear to be refined into smaller grains at the particle/substrate interface. This is characteristic of the cold spray process where the mechanical stress and

thermal energy transfer from the high impact velocity induces grain refinement [24]. In the middle region of the samples, the grains are deformed into longer, thinner splats. This is followed by a more preserved grain structure at the top of the particle. [12]

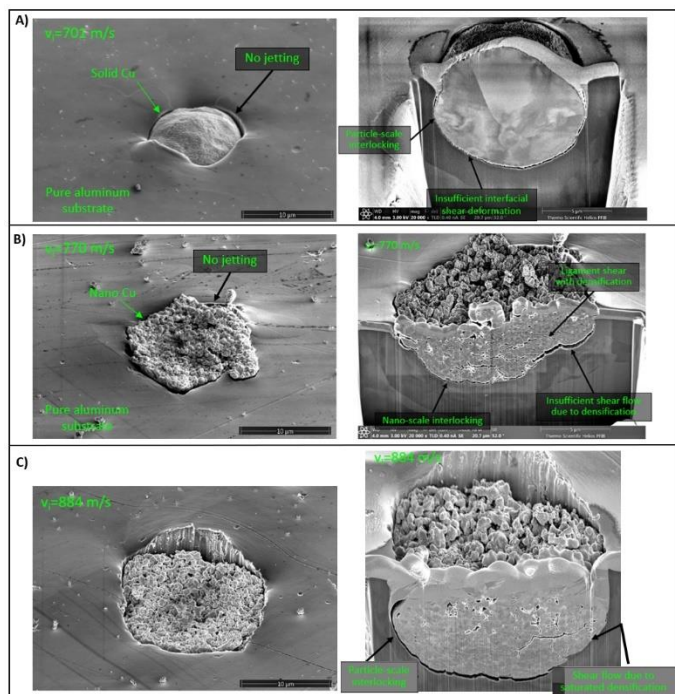


Figure 7: LIPIT of A) conventional Cu powder particle at 701 m/s, and nano-agglomerate Cu powder particle at B) 770 m/s, C) 884 m/s

The impacted conventional Cu powder and nano-agglomerate powder sprayed at 701m/s and 770m/s respectively do not appear to have any jetting. When cross-sectioned, both have some areas at the particle-substrate interface with firm interlocking and other areas where there is a slight gap. In conventional Cu this is due to lack of shear deformation of the particle [7]. For nano-agglomerate Cu powder, the densification of the porous structure away from the substrate causes the lack of shear flow at the particle-substrate interface. There is also a distinct change in grain size and compression, with smaller grains and greater deformation at the base of the particle [23, 13, 11].

A change in porosity is seen in the nano-agglomerate powder as compared to the pre-impact powder. In the 884m/s particle, there is approximately 10% porosity as compared to the 50% porosity of the particle pre-impact. With the higher velocity of 884m/s there is also jetting present and shear flow from densification against the particle-substrate interface. [6]

The nano-agglomerate Cu powder behaves similar to a foam in that energy leaves the pores on impact causing plastic deformation of the porous structures. With higher impact velocity there is greater compressive residual stress and lower porosity [24].

Overall, LIPIT shows that with increased speed there is increased particle-substrate mechanical interlocking and shear flow. Impact velocity causes vertical compression contributing to increased density and strength of the particle [26]. This is followed by lateral flow, which produces a mechanical bond between the two dissimilar metals. While physical interlocking stops the particle movement into the substrate, this does not guarantee good bond formation, as shear flow movement continues. Because of the shear flow that continues from pore densification in the nano-agglomerate powder, a higher critical velocity is needed to form a strong bond. Vertical impact velocity also contributes to the unique gradient microstructure, where material recrystallization from shear stress can be seen at the base of the impacted particle [MOD].

3.3. Coating Microstructure

Consolidated microstructure for nanomaterial and conventional Cu coatings can be seen in Figure 8. Similar to the single-splats, the consolidated coatings are highly recrystallized at the particle-substrate interface (left-side of

the micrograph), followed by a middle region of deformed large particles/grains and a less deformed upper-top region (right-side) [24]. This is most noticeable in the bottom righthand micrograph of etched nanomaterial Cu.

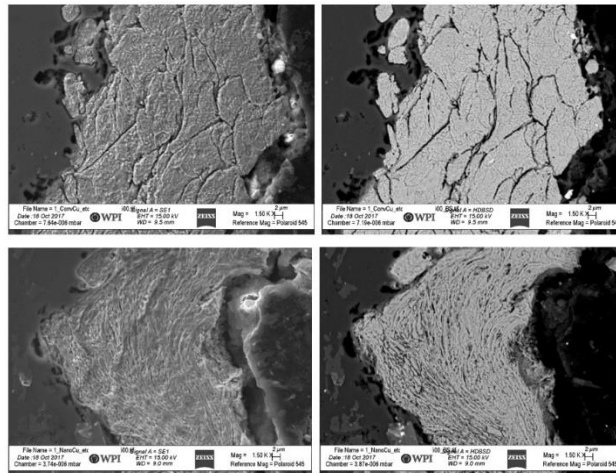


Figure 8: SEM micrographs of cross-sectioned etched consolidated conventional Cu (top), nanomaterial Cu (bottom)

The high recrystallization region is from flow stress which can result from both temperature increase due to kinetic energy transfer on impact and from work hardening causing physical dislocation movement to form sub grains [23, 24, 12].

Flattened, elongated grains in the middle of the coatings show shear deformation. As the powder particles build on one another a peening effect occurs where the prior layers are work hardened and further compressed on impact. This is not as prevalent in the top-most layers of the coating [16]. In the consolidated conventional Cu, the etching is able to highlight some of the jetting and roll-ups at the particle-substrate and particle-particle interfaces [21, 12].

For antimicrobial applications, there is interest in the top-down microstructure of the coatings. Micrographs of the top-down as-made and polished coatings are in Figure 9.

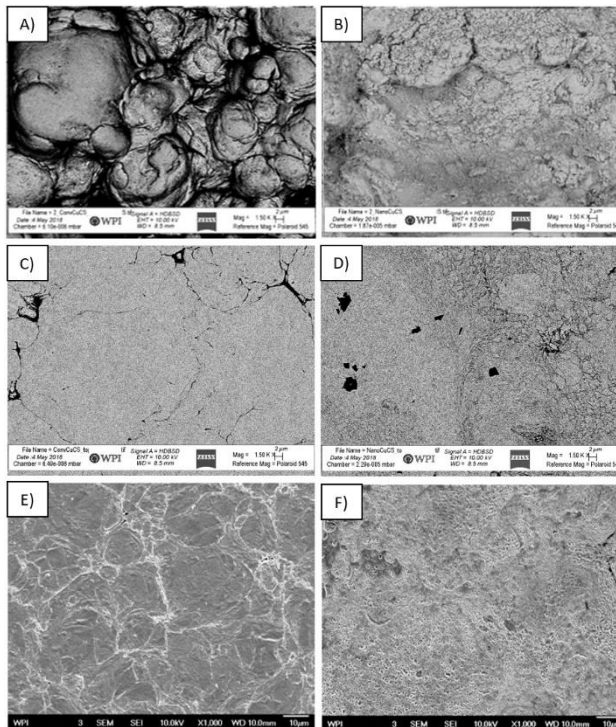


Figure 9: SEM backscatter micrograph of top-down consolidated A) conventional Cu, B) nanomaterial Cu, C) polished conventional Cu, D) polished nanomaterial Cu. FE SEM micrograph of top-down polished etched consolidated E) conventional Cu, F) nanomaterial Cu

There is a clear difference in surface topography between the two as-made coatings. Visually, conventional Cu has much bigger structures with higher peaks and valleys than the nanomaterial Cu. However, this is not the case when viewing surface roughness at the micron and nano scales, which would be the scale where Cu contact killing of microbes would occur ^[20]. The polished surfaces show much larger grains for the conventional than nanomaterial Cu coatings. This difference in grain size is further detailed using EBSD shown in Figure 10.

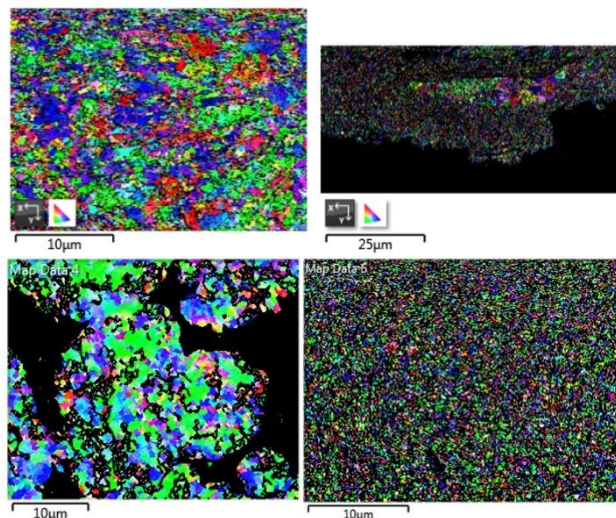


Figure 10: EBSD of polished consolidated cross-section of conventional Cu (top left) and nanomaterial Cu (top right) and top-down conventional Cu (bottom left) and nanomaterial Cu (bottom right)

Visually, both the EBSD top-down and cross-section micrographs show nanomaterial Cu to have a finer microstructure with much smaller grain size than that of conventional Cu. EBSD measured grain size averages for top-down conventional and nanomaterial Cu are 0.9µm and 0.43µm, respectively. EBSD measured grain size averages for the cross-sections of conventional and nanomaterial Cu are 0.57µm and 1.12µm, respectively. The top-down measurement confirms smaller grain size for the nanomaterial Cu than conventional Cu. However, the EBSD results for cross-section coatings show a discrepancy in the micrographs versus the grain-size measurement where the nanomaterial Cu appears to have smaller grain size than that of conventional Cu, but is measured as having a greater average grain size. Since the nanomaterial Cu powder is comprised of both nano particles and conventional Cu binder it is possible that the section measured with EBSD had a large amount of conventional Cu binder which skewed the results. It is also possible that EBSD is measuring the high angle-misorientation (greater than 15%) and is not accounting for low-angle-misorientation (less than 2%) ^[26]. This would explain why these measurements are much higher than prior values taken using TEM data ^[20].

TEM micrographs taken from prior work in the paper “The Effect of Nano-Scale Surface Roughness on Copper Cold Spray Inactivation of Influenza A Virus”, confirm large differences in grain size for nanomaterial Cu cross-sections, showing an average range from 2.0nm-0.1µm. Conventional Cu cross-sections were also measured with an average grain size ranging from 0.2-1.5µm ^[20]. These values show that a large amount of grain refinement has occurred in both samples as a result of the cold spray process ^[20, 1].

3.4. Composition and XRD Analysis

EDS data is referenced in Supplemental Section A. EDS results show Cu with some oxygen present in the powder and only Cu present for the consolidated cross-sections. Some carbon was present as well, but most likely from the mounting material.

XRD data for both powders is referenced in Supplemental Section B. XRD data supports EDS results showing peaks for Cu. Cu₂O was found to be present in the nano-agglomerate powder as well. Both powders correlated well to reference Cu PDF 00-004-0836.

For the nano-agglomerate powder, the nano particles used are amorphous (see supplemental C) and are not easily detectible by the x-rays [5]. It is likely that XRD is detecting the pure Cu binder used to bind the nano particles together and not the nano particles themselves. Further analysis (see supplemental B) of the Bragg angle and calculated d-spacing shows the same values for the powders and the reference PDF, indicating minimal contribution of strain to peak broadening. The nano-agglomerate powder does have greater intensity than the conventional Cu powder. This may be an indicator that the Cu binder used in the nano-agglomerates is well formed and highly crystalline. It is also possible that the intensity value for conventional Cu powder is lower due to preferred orientation. [5]

3.3. Mechanical Data

Nanoindentation measurements taken of the top-down consolidated nanomaterial and conventional Cu surfaces are in Table 1.

Table 1: Nanoindentation of Consolidated Cu CS

| Sample: | Orientation: | Hardness (GPa): |
|-----------------|--------------|-----------------|
| Nanomaterial Cu | Top-down | 2.37+/- 0.19 |
| Conventional Cu | Top-down | 2.01 +/- 0.04 |

Top-down measurements show nanomaterial Cu to have greater hardness and subsequent yeild strength as compared to conventional Cu. Hall-Petch shows an inverse relationship between hardness and grain size [8]. Based on the micrographs in Section 3.1, it is clear that nanomaterial Cu follows the Hall-Petch relation despite the presence of nano-grains. It is possible that the nanomaterial also has a greater degree of particle deformation and work hardening, both contributing factors in the increased material hardness [24].

There is a relationship between hardness and antimicrobial effectiveness [19,3]. Further analysis of the hardness and microstructure data solidifies that grain size is a major factor affecting Cu cold spray hardness and antimicrobial properties, where there is greater antimicrobial effectiveness with decreasing grain size.

4. Conclusion

- 1) Pre-impact, nano-agglomerate Cu powder has smaller grains and greater porosity then conventional Cu powder. This is due to the spray drying process and nano-particles used.
- 2) LIPIT shows critical velocity for 15um sized conventional and nano-agglomerate Cu powder particles to be 610m/s and 740m/s, respectively. LIPIT shows that with increased velocity there is densification. Pre-impact nano-agglomerate powder porosity is 50% and post-impact it is reduced to 10%. Cross-section micrographs show gradient porosity with greater porosity at the top of the particle.
- 3) Consolidated cross-sectioned conventional and nanomaterial Cu support LIPIT results by displaying three main microstructure regions: 1) grain refined/re-crystallized area at the particle-substrate interface 2) elongated/deformed grains in the mid-section of the particle, and 3) more preserved grain structure at the top of the particle.
- 4) All coatings have minimal to no oxides/impurities. XRD and EDS confirm Cu powder and coating composition to be pure Cu. The nano-agglomerate Cu powder did have one CuO₂ diffraction peak, however, the oxide did not appear in the consolidated coating.

5) Both cross-section and top down micrographs show nanomaterial Cu to have smaller grain size than conventional Cu. Nanoindentation measurements of the surface show good correlation between increasing hardness and decreasing grain size with hardness being much greater for nanomaterial than conventional Cu.

6) With smaller grains, nanomaterial Cu has a greater number of grain boundaries. Since Cu's antimicrobial properties are contact-based, it stands to reason that the increase in grain boundaries allows for an increase in ion flow which contributes to the more efficient contact killing of Influenza A Virus by nanomaterial Cu.

Additional work is needed to test LIPI on various substrates, including Cu, with different particle sizes. Work can also be done to also confirm visual findings with hardness testing of top-down and cross-sectioned impacted particles.

Follow-on work is needed to confirm the hypothesized difference in ion release through corrosion testing. And efficacy testing of polished surfaces is needed to uncouple the effects of surface roughness and microstructure on antimicrobial properties of Cu cold spray.

Acknowledgement

Thank you to UMass Department of Mechanical and Industrial Engineering for Laser Induced Projectile Impact Testing.

References

- [1] Borches C, Gartner F, Stoltenhoff T, "Microstructural and Macroscopic Properties of Cold Sprayed Copper Coatings". *Journal of Applied Physics* (2003) 93: 10064-10070.
- [2] Callister W, Rethwisch D, "Materials Science and Engineering: An Introduction, Enhanced" Publisher: Wiley , Print ISBN: 9781119278566, 1119278562, Edition: 10th , Copyright year: 2018
- [3] Champagne, V.; Helfritsch, D. A Demonstration of the Antimicrobial Effectiveness of Various Copper Surfaces, *Journal of Biological Engineering* 2013, 7:8 <https://doi.org/10.1186/1754-1611-7-8>
- [4] Chen, Q., Alizadeh, A., Xie, W., Wang, X., Champagne, V., & Gouldstone, A. et al. (2018). High-Strain-Rate Material Behavior and Adiabatic Material Instability in Impact of Micron-Scale Al-6061 Particles. *Journal Of Thermal Spray Technology*, 27(4), 641-653. doi: 10.1007/s11666-018-0712-4
- [5] Cullity B, Stock S, "Elements of X-Ray Diffraction". Upper Saddle River, NJ: Prentice Hall, 2001. Print.
- [6] Fukumoto M, et al., "Deposition of Copper Fine Particles by Cold Spray Process". *Materials Transactions* (2009) 50: 1482-1488.
- [7] Grujicic M, et al., "Computational analysis of the interfacial bonding between feed-powder particles and the substrate in the cold-gas dynamic-spray process" *Applied Surface Science* (2003) 219: 211-227
- [8] Hansen, Niels. Hall-Petch Relation and Boundary Strengthening. *Scripta Materialia* 51 (2004) 801–806.
- [9] Hassani-Gangaraj M, Veysset D, Nelson K, Schuh C, "In-situ observations of single micro-particle impact bonding". *Scripta Materialia*, 145, 9-13 (2018).
- [10] Kim, K. H., M. Watanabe, J. Karakita, and S. Kuroda. 2008. Grain refinement in a single titanium powder particle impacted at high velocity. *Scripta Materialia* 59:768–771.

- [11] King P, et al., "An Experimental and Finite Element Study of Cold Spray Copper Impact onto Two Aluminum Substrates". *J of Thermal Spray Technology* (2009) 19:629-634.
- [12] Lee C, Kim J. "Microstructure of Kinetic Spray Coatings: A Review". *Journal of Thermal Spray Technology* (2015) 24: 592-610.
- [13] Lee, J., Loya, P., Lou, J., & Thomas, E. (2014). Dynamic mechanical behavior of multilayer graphene via supersonic projectile penetration. *Science*, 346(6213), 1092-1096. doi: 10.1126/science.1258544
- [14] Lee, J., Veysset, D., Singer, J., Retsch, M., Saini, G., Pezeril, T., Nelson, K. and Thomas, E. (2012). High strain rate deformation of layered nanocomposites. *Nature Communications*, 3(1).
- [15] Praxair: surface technologies. Powder Solutions: product brochure. www.praxairsurfacetechologies.com.
- [16] Rokni M, et al., "Review of Relationship Between Particle Deformation-Coating Microstructure and Properties in High Pressure Cold Spray". *Journal of Thermal Spray Technology* (2017) 1-140.
- [17] Rolfe S, (2014) email conversation and Phase I SBIR Final Report, "Advanced Nanostructured Powders for Cold Spray Applications", Eltron Research and Development Inc., 4600 Naytilus Court South Boulder, CO 80301-3241
- [18] Schmidt T., et al. Development of a generalized parameter window for cold spray deposition. *Acta Materialia* 54 (2006) 729–742.
- [19] Sundberg, K., Champagne, V., McNally, B., Helfritsch, B., Sisson, R., "Effectiveness of Nanomaterial Copper Cold Spray Surfaces on Inactivation of Influenza A Virus," *J Biotechnology and Biomaterials*, 5 (4). 2015.
- [20] Sundberg K, Gleason M, Haddad B, Champagne V, Brown C, Sisson R, Cote D. "The Effect of Nano-Scale Surface Roughness on Copper Cold Spray Inactivation of Influenza A Virus". *Journal TBD*.
- [21] Sundberg K, Sousa B, Schreiber J, Walde C, Sisson R, Cote D. "Modeling Copper Cold Spray Single-Particle Impact for Optimized Antimicrobial Coatings". *Journal TBD*.
- [22] Theivasanthi T., ALAGAR M., "X-Ray Diffraction Studies of Copper Nanopowder". *Applied Physics Research* 2010 (1) 112-117.
- [23] Villafuerte J. "Modern Cold Spray: Materials, Processes, Applications". Springer: Ontario, Canada. 2015.
- [24] Viscusi A, et al., "A perspective review on the bonding mechanisms in cold gas dynamic spray". *Surface Engineering* (2018) 1743-2944.
- [25] Xie, W., Alizadeh-Dehkarghani, A., Chen, Q., Champagne, V., Wang, X., Nardi, A., Kooi, S., Müftü, S. and Lee, J. (2017). Dynamics and extreme plasticity of metallic microparticles in supersonic collisions. *Scientific Reports*, 7(1).
- [26] Young-Kyun et al. "Microstructure and Room Temperature Compressive Deformation Behavior of Cold-Sprayed High-Strength Cu Bulk Material". *J Therm Spray Tech* (2017) 26:1498–1508

Supplemental Section A: (EDS Data)

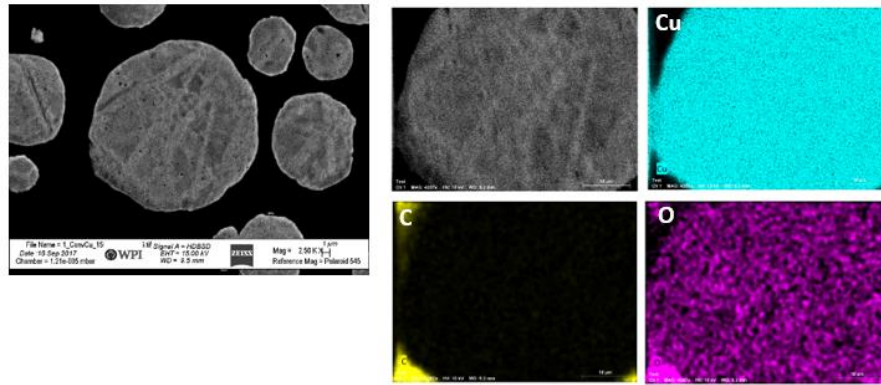


Figure X: EDS of Conventional Cu Powder Particle

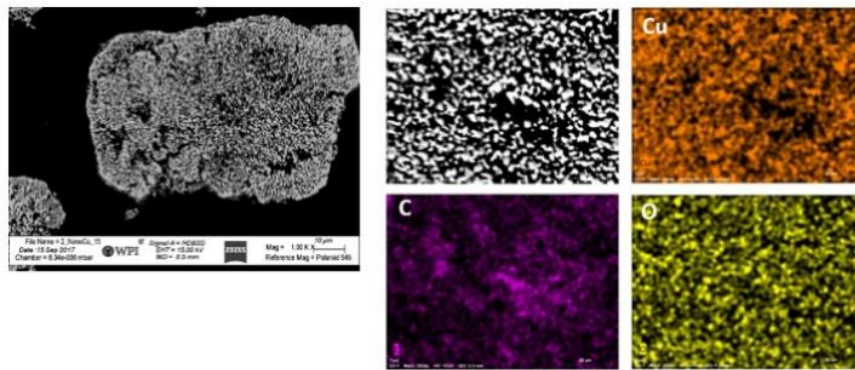


Figure X: EDS of Nano-agglomerate Cu Powder Particle

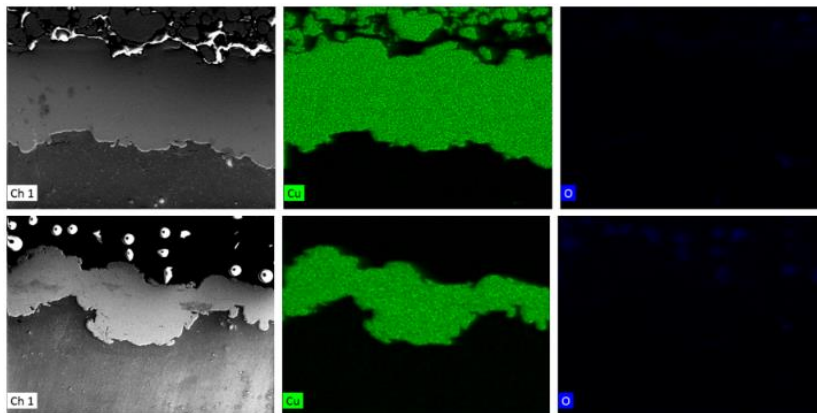


Figure X: EDS of consolidated cross-sectioned conventional Cu (top) and nanomaterial Cu (bottom)

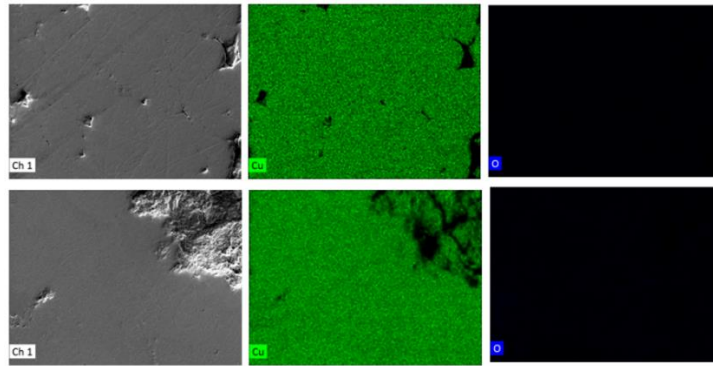


Figure X: EDS of polished consolidated top-down conventional Cu (top) and nanomaterial Cu (bottom)

Supplemental Section B: (XRD Data)

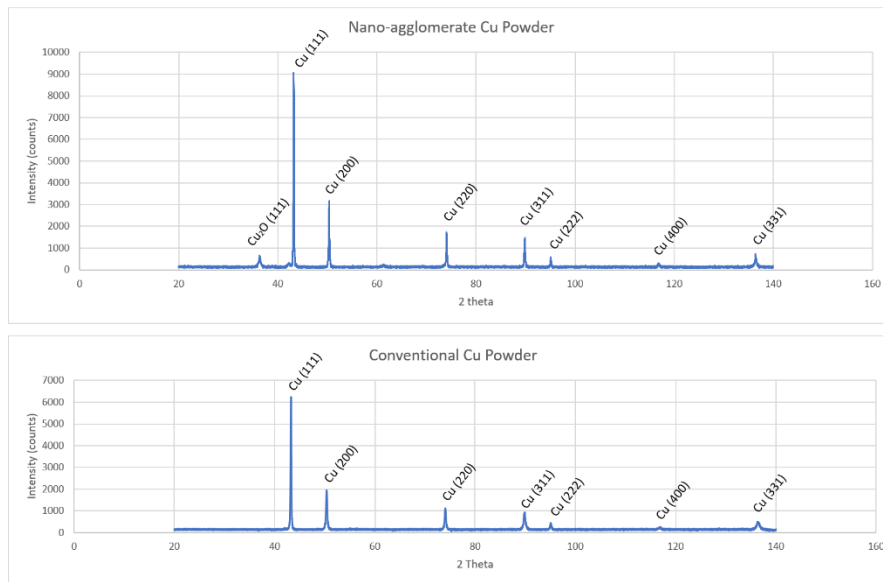


Figure X: XRD peaks of Nano-agglomerate (top) and Conventional (bottom) Cu Powder Particles

Table X: XRD Powder Results and Indexing Using Bragg's Angle (nano-agglomerate pdr-top, conventional powder-bottom)

| Peaks | Peak Match (Cu, CuO, Cu2O) | Nano-Agglom. Pdr Peak Position (2 theta) | Reference Peak Position (2 theta) | Nano-Agglom. Pdr. Intensity | | Reference Intensity (normalized) | Nano-Agglom. Pdr. Indexing | | (hkl) | Remarks |
|-------|-----------------------------|--|-----------------------------------|-----------------------------|------------------------|----------------------------------|-------------------------------|-------------------------------------|-------|--|
| | | | | Intensity (counts) | Intensity (normalized) | | 1000 x Sin ² theta | (1000 x Sin ² theta) /46 | | |
| 1 | Cu2O (pdf card 00-005-0667) | 36.352 | 36.418 | 675 | 74 | 100 | 97.304 | 2.115 | (111) | 1 ² +1 ² +1 ² =3 |
| 2* | Cu (pdf card 00-004-0836) | 43.256 | 43.296 | 9061 | 100 | 100 | 135.850 | 2.953 | (111) | 1 ² +1 ² +1 ² =3 |
| 3* | Cu (pdf card 00-004-0836) | 50.384 | 50.433 | 3172 | 35 | 46 | 181.179 | 3.938 | (200) | 2 ² +0 ² +0 ² =4 |
| 4* | Cu (pdf card 00-004-0836) | 74.064 | 74.130 | 1730 | 19 | 20 | 362.718 | 7.885 | (220) | 2 ² +2 ² +0 ² =8 |
| 5 | Cu (pdf card 00-004-0836) | 89.88 | 89.930 | 1473 | 16 | 17 | 498.951 | 10.846 | (311) | 3 ² +1 ² +1 ² =11 |
| 6 | Cu (pdf card 00-004-0836) | 95.096 | 95.139 | 578 | 6 | 5 | 544.412 | 11.835 | (222) | 2 ² +2 ² +2 ² =12 |
| 7 | Cu (pdf card 00-004-0836) | 116.88 | 116.918 | 291 | 3 | 3 | 645.183 | 14.025 | (400) | 4 ² +0 ² +10=16 |
| 8 | Cu (pdf card 00-004-0836) | 136.448 | 136.506 | 733 | 8 | 9 | 899.881 | 19.56 | (331) | 3 ² +3 ² +1 ² =18 |

| Peaks | Peak Match (Cu, CuO, Cu2O) | Conventional Pdr. Peak Position (2 theta) | Reference Peak Position (2 theta) | Conventional Pdr Intensity | | Reference Intensity (normalized) | Conventional Cu Pdr. Indexing | | (hkl) | Remarks |
|-------|-----------------------------|---|-----------------------------------|----------------------------|------------------------|----------------------------------|-------------------------------|-------------------------------------|-------|--|
| | | | | Intensity (counts) | Intensity (normalized) | | 1000 x Sin ² theta | (1000 x Sin ² theta) /46 | | |
| 1 | Cu2O (pdf card 00-005-0667) | n/a | 36.418 | n/a | n/a | 100 | n/a | n/a | (111) | 1 ² +1 ² +1 ² =3 |
| 2* | Cu (pdf card 00-004-0836) | 43.296 | 43.296 | 6227 | 100 | 100 | 136.089 | 2.958 | (111) | 1 ² +1 ² +1 ² =3 |
| 3* | Cu (pdf card 00-004-0836) | 50.424 | 50.433 | 1856 | 30 | 46 | 181.449 | 3.945 | (200) | 2 ² +0 ² +0 ² =4 |
| 4* | Cu (pdf card 00-004-0836) | 74.072 | 74.130 | 1113 | 18 | 20 | 362.785 | 7.886 | (220) | 2 ² +2 ² +0 ² =8 |
| 5 | Cu (pdf card 00-004-0836) | 89.896 | 89.930 | 926 | 15 | 17 | 499.092 | 10.849 | (311) | 3 ² +1 ² +1 ² =11 |
| 6 | Cu (pdf card 00-004-0836) | 95.096 | 95.139 | 444 | 7 | 5 | 544.412 | 11.835 | (222) | 2 ² +2 ² +2 ² =12 |
| 7 | Cu (pdf card 00-004-0836) | 116.904 | 116.918 | 253 | 4 | 3 | 726.248 | 15.788 | (400) | 4 ² +0 ² +10=16 |
| 8 | Cu (pdf card 00-004-0836) | 136.36 | 136.506 | 489 | 8 | 9 | 861.845 | 18.375 | (331) | 3 ² +3 ² +1 ² =18 |

*= top three intense peaks

Table X: Determining D-Spacing using Bragg's Law:

| Peak | Nano-Agglomerate Cu Powder | | | | Conventional Cu powder | | | | PDF Reference D-Spacing |
|------|----------------------------|----------|---------------|---|------------------------|----------|---------------|---|-------------------------|
| | λ | θ | 2Sin θ | $d = \frac{\lambda}{2\text{Sin}\theta}$ | λ | θ | 2Sin θ | $d = \frac{\lambda}{2\text{Sin}\theta}$ | |
| 1 | 1.541 | 18.176 | 0.624 | 2.469 | 0.1541 | n/a | n/a | n/a | 2.465 |
| 2* | 1.541 | 21.628 | 0.737 | 2.091 | 0.1541 | 21.628 | 0.737 | 2.090 | 2.088 |
| 3* | 1.541 | 25.192 | 0.851 | 1.811 | 0.1541 | 25.212 | 0.852 | 1.808 | 1.808 |
| 4* | 1.541 | 37.032 | 1.205 | 1.279 | 0.1541 | 37.036 | 1.205 | 1.279 | 1.278 |
| 5 | 1.541 | 44.94 | 1.413 | 1.091 | 0.1541 | 44.948 | 1.413 | 1.091 | 1.090 |
| 6 | 1.541 | 47.548 | 1.476 | 1.044 | 0.1541 | 47.548 | 1.476 | 1.044 | 1.044 |
| 7 | 1.541 | 58.44 | 1.704 | 0.904 | 0.1541 | 58.452 | 1.704 | 0.904 | 0.904 |
| 8 | 1.541 | 68.224 | 1.857 | 0.829 | 0.1541 | 68.18 | 1.857 | 0.829 | 0.829 |

*= top three intense peaks

Table X: Indexing Using D-Spacing:

| Peaks | Nano-Agglomerate Powder D-spacing | | | | Conventional Powder D-spacing | | | | PDF Reference D-spacing | | | |
|-------|-----------------------------------|---------------------|------------------------------|---------|-------------------------------|---------------------|------------------------------|---------|-------------------------|---------------------|------------------------------|---------|
| | d | 1000/d ² | (1000/d ²)/77.32 | Rounded | d | 1000/d ² | (1000/d ²)/77.32 | Rounded | d | 1000/d ² | (1000/d ²)/77.32 | Rounded |
| 1 | 2.469 | 164.043 | 2.123 | 2 | n/a | n/a | n/a | n/a | 2.465 | 164.582 | 2.128 | 2 |
| 2* | 2.091 | 228.713 | 2.958 | 3 | 2.090 | 228.932 | 2.961 | 3 | 2.088 | 229.371 | 2.967 | 3 |
| 3* | 1.811 | 304.904 | 3.943 | 4 | 1.808 | 305.640 | 3.953 | 4 | 1.808 | 305.916 | 3.956 | 4 |
| 4* | 1.279 | 611.306 | 7.906 | 8 | 1.279 | 611.306 | 7.906 | 8 | 1.278 | 612.263 | 7.918 | 8 |
| 5 | 1.091 | 840.137 | 10.865 | 11 | 1.091 | 840.137 | 10.865 | 11 | 1.090 | 841.679 | 10.885 | 11 |
| 6 | 1.044 | 917.485 | 11.866 | 12 | 1.044 | 917.485 | 11.866 | 12 | 1.044 | 917.485 | 11.866 | 12 |
| 7 | 0.904 | 1223.666 | 15.825 | 16 | 0.904 | 1223.666 | 15.825 | 16 | 0.904 | 1223.666 | 15.825 | 16 |
| 8 | 0.829 | 1455.094 | 18.819 | 18 | 0.829 | 1455.094 | 18.819 | 18 | 0.829 | 1455.094 | 18.819 | 18 |

*= top three intense peaks

Supplemental Section C: (Microstructure Data)

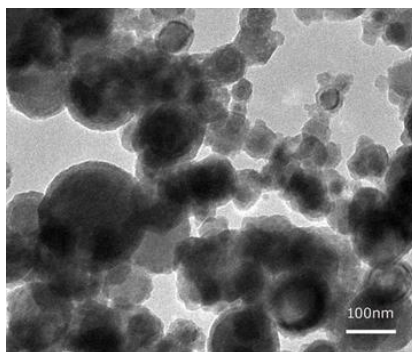


Figure X: Nanoparticle Micrograph (courtesy of skyspring nanomaterials) showing 60-80nm particles.

6. Paper #4: The Effect of Corrosion on Conventional and Nanomaterial Copper Cold Spray Surfaces for Antimicrobial Applications

The Effect of Corrosion on Conventional and Nanomaterial Copper Cold Spray Surfaces for Antimicrobial Applications

Kristin Sundberg^{1,*}, Yanggang Wang², Brajendra Mishra³, Alexander Carl, Ronald Grimm, Alino Te, Lindsay Lozeau, Richard Sisson, Danielle Cote

^{1,2,3} Materials Science and Engineering, Worcester Polytechnic Institute, Worcester, MA, USA

*Corresponding author: kristinsundberg7@yahoo.com

Received Month X, XXXX; revised Month X, XXXX; accepted Month X, XXXX

Abstract Cold spray has been identified as having Cu coatings with greater antimicrobial properties than that of other additive manufacturing techniques ^[13]. The addition of nano-agglomerate Cu powder to the cold spray process to form nanomaterial coatings has shown an increase in antimicrobial efficiency, as compared to conventional Cu, in the contact killing of Influenza A Virus ^[39]. Corrosion testing, microstructural analysis, and composition measurement can help explain why cold sprayed nanomaterial Cu coatings performed better than conventional Cu coatings. Corrosion tests including electrochemical impedance (EIS), Linear Polarization (LP), and an Ion Release Assay all show nanomaterial Cu to have a greater corrosion rate than that of conventional Cu. Micrographs support corrosion results showing nanomaterial Cu to have much smaller grains than conventional Cu, indicating a greater percentage of grain boundaries available for Cu ion release into the environment ^[8]. Composition testing through X-Ray Diffraction and X-Ray Photoelectron Spectroscopy (XPS) confirm sample surfaces to be comprised of pure Cu and Cu oxide, with the main oxide species present as Cu(i) or Cu₂O. More research is needed to determine how the dominant Cu species develops based on environmental factors and how the presence of different species affect material antimicrobial properties.

Keywords: *Corrosion, Nanomaterial Cu, Cold Spray, Ion Release, Linear Polarization, Electrochemical Impedance*

1. Background

The U.S. spends over \$125 billion a year in prevention of touch surface infections ^[2,11]. Copper cold spray coatings have been identified as having greater antimicrobial effectiveness than other additive methods ^[13]. This paper builds off of prior work from the paper “Effectiveness of Nanomaterial Copper Cold Spray Surfaces on Inactivation of Influenza A Virus”, where copper cold spray antimicrobial properties are improved with the use of nano-agglomerate Cu powder ^[39]. There is a need to further qualify consolidated nanomaterial Cu material properties in relation to conventional Cu to better understand Cu kill-mechanisms.

The primary killing mechanism of copper is contact killing through deformation of microbe membranes by copper ions leading to cell cytoplasm release and subsequent internal damage to the cell ^[22, 29, 12]. Further research is needed to determine the main mechanisms for copper ion uptake into the cell ^[2,44,23, 6]. Research is being performed in the biology field to better understand microbial copper ion defense and uptake mechanisms, including mapping of internal signal pathways and external cell interactions that lead to selective ligand favorability ^[2,19,23,15,43]. Factors affecting copper ion release from the consolidated Cu surface include material microstructure, surface roughness, and surface chemistry ^[29, 44, 20, 13, 34, 35, 39, 19]. This paper focuses on measurement of the differences in Cu ion release between conventional and nanomaterial Cu cold sprayed surfaces through corrosion testing, with supplemental surface chemistry and microstructure characterization.

Grain boundaries have a more open structure than that of atomic grains, making the barrier for diffusion much less in grain boundaries than in the material lattice ^[8]. In nanomaterial Cu, smaller grain size allows for a greater number of grain boundaries and an increase in ion diffusion as compared to conventional Cu, making microstructure a key factor in nanomaterial Cu’s increased antimicrobial effectiveness ^[41, 42, 27]. Nanomaterial Cu also has a much greater surface roughness than that of conventional Cu at the nano-scale, which is the same scale for Influenza A Virus. This may also be a contributing factor in Cu ion release ^[40].

Environmental factors also affect corrosion rate, including changes in temperature, pH, and humidity. Water can become de-aerated with increasing temperature, where this decrease in oxygen may decrease corrosion rate [10]. This is not a concern for this work since testing is performed at room temperature. As pH decreases, Cu-alloys and protective films are unable to develop, causing an increase in corrosion rate [10, 21]. In a study performed by Feng et al, copper oxide thickness in relation to H₂O pH was measured where pH below 4 caused oxide dissolution, pH higher than 4 formed Cu₂O, and pH above 10 formed CuO [17]. For this paper 3% (weight) NaCl solution is used in corrosion testing. NaCl is formed from HCl and NaOH, which are a strong acid and base, respectively. Salts comprised of both a strong acid and base do not hydrolyze, instead they dissociate in water into Na⁺ and Cl⁻ ions [24]. The dipole nature of H₂O allows for this to occur, where Na⁺ is attracted to the electronegative oxygen and Cl⁻ is attracted to the electropositive hydrogen [20, 1]. The result is a neutral pH solution. It follows that the predominant oxide to form at this pH is Cu₂O. However, humidity also plays a role in oxide species presence, where Cu(i), also known as Cu₂O, is more stable in dry environments and Cu(ii), also known as CuO, is more stable in aqueous environments [32].

Other factors determining the favorability of copper oxide state include Cu geometry, bonding, and hard-soft acid-base (HSAB) theory [32, 35, 36, 43, 7, 23]. Cu(i) prefers a tetrahedral geometry, favors back-bonding, and is a soft acid that associates with soft bases, whereas Cu(ii) prefers octahedral geometry, has a low degree of back bond donation, and is a borderline hard acid that associates with harder bases. All of the above listed factors may be affected by the environment and the microbes in it. Microbes can select for certain kinds of geometries and bonds using specific ligands and bonding sites, they can also excrete material that changes local pH, and can change their own internal pH [23, 43, 20, 2, 19, 32, 30]. So even if a certain kind of Cu species manifests on the surface of a consolidated Cu coating as a result of environmental factors, this does not mean that the same species will be received or internalized by the microbe.

When considering lifecycle and maintenance of Cu coatings, it is important to note that oxides/tarnishing of the Cu surface does not affect the antimicrobial efficacy of the coating [45, 28]. Post-processing heat treatment is not recommended for this application as it could negate the antimicrobial effects of the nano-particles used in the nanomaterial Cu cold spray coating [8]. It is possible that for other applications the need for residual stress relief outweighs the need for antimicrobial efficiency, in those cases heat treatment may be used. Heat treatment work is included in this paper, but most data is placed in the supplemental section as this work is out of scope for the given antimicrobial application.

The Pourbaix diagram, Figure 1, can provide important background information on the movement of Cu ions with changing potential and pH. The Pourbaix diagram assumes that the movement of ions flows passively from high to low concentration. The region in between the two blue dashed lines indicates the thermodynamic stability region of H₂O at 1atm. [21]

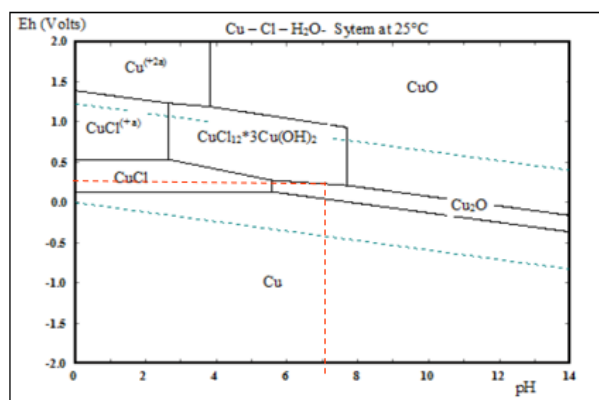


Figure 1: Pourbaix Diagram for Cu in 3%NaCl solution (in water) at 25°C [modified from- 25]

Cu corrosion has an anodic and cathodic reaction. The anodic reaction dissociates Cu into electrons and Cu ions, which can form oxides like Cu₂O and CuO or hydroxides like Cu(OH)₂. The cathodic reaction consumes the electrons released from the anodic reaction. Since NaCl solution in water is neutral, the cathodic reaction would be: O₂+2H₂O+4e⁻ = 4OH⁻. Considering that neutral pH is 7 and that standard electron potential of Cu is 0.34, the pourbaix diagram can be used to plot these values, as indicated by the red dashed lines in Figure 1. An estimate

of the resulting corrosion products is determined to be right on the line between $\text{CuCl}_2 \cdot 3 \text{Cu}(\text{OH})_2$, and Cu_2O . However, the Pourbaix diagram serves only as an estimate, since it does not take into consideration corrosion rate which can be changed with voltage. [21, 25, 46]

The pourbaix estimate can be confirmed through X-Ray Diffraction (XRD) and X-Ray Photoelectron Spectroscopy (XPS). Both methods can determine the Cu species present on the sample post-corrosion testing, however, XPS is able to more accurately measure the top-most atomic layers (~5nm depth) of the sample.

Linear polarization (LP) and electrochemical impedance (EIS) corrosion tests can be performed using an electrochemical cell. LP measures corrosion rate and EIS measures impedance response at a fixed frequency [21]. Ion concentration can also be measured through an ion release assay using an inductively coupled plasma mass spectrometer (ICP-MS). Corrosion results are comparable to efficacy of nanomaterial vs. conventional Cu, where an increase in corrosion rate or ion concentration in the environment indicates an increase in Cu ion release from the substrate [21]. Since Cu's kill mechanism is through Cu ion release through contact with the surface, it follows that an increase in Cu ion release will be proportional to the material's antimicrobial effectiveness. Measuring changes in corrosion and composition will allow for a better understanding of why nanomaterial Cu is more efficient in the contact killing of Influenza A Virus than conventional Cu and will aid future research in better understanding the contact killing mechanism.

2. Test Procedure

2.1. Materials

2.1.1. Cold Spray

Cold spray samples from the first paper, "Effectiveness of Nanomaterial Copper Cold Spray Surfaces on Inactivation of Influenza A Virus" [39], were used. The pure Cu cold spray coatings on aluminum substrates are approximately 0.05 mm thick. The nano copper (Eltron) was produced by spray drying and the conventional copper (Praxair Cu-159) through gas atomization. Due to the low mass of the nano-particles, they are bound into agglomerates using conventional Cu as the binder and spray dried [31, 37]. For more information on the materials and cold spray process parameters see reference 39. Cold spray samples are compared to bulk wrought pure Cu.

2.1.2. Heat Treated Cu

Worcester Polytechnic Institute (WPI) performed oxidation treatment on 99% Pure Bulk Cu, heated in a furnace at 250C for 2 hours. The furnace was then turned off and the samples were allowed to cool inside for 20 hours.

Heat treatment (annealing) of bulk, conventional, and nanomaterial Cu surface was performed by Surface Combustion. Samples were cleaned using acetone and placed in a molybdenum lined, high temperature lab furnace. The chamber was evacuated with a vacuum pump and heated to 100F, then backfilled to 1atm nitrogen and heated to 400C for two hours. The samples were then cooled under nitrogen with an internal fan.

2.2. Corrosion Testing

2.2.1 Electrochemical Testing

A ParaCell Electrochemical Cell Kit by Gamry Instruments was used with 3% (weight) NaCl solution and a Mercury Chloride (G0115 LOT 2516) reference electrode. Figure 2 shows a detailed diagram of the test set-up; the Paracell Manual (988-00017) was used to set up the test.

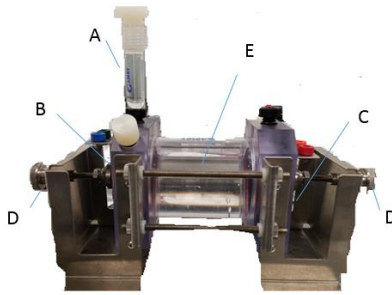


Figure 2: Diagram of corrosion cell including A) reference electrode in solid bridge filled with NaCl, B) Cu sample pressed between electrode (anode) plate and cell opening, C) Carbon pressed between electrode (cathode) plate and cell opening, D) clamps used to secure B + C, E) corrosion cell filled with NaCl Solution.

The corrosion cell is attached to the EC Lab software using electrical cables. The cable attachments are labeled in Figure 3.

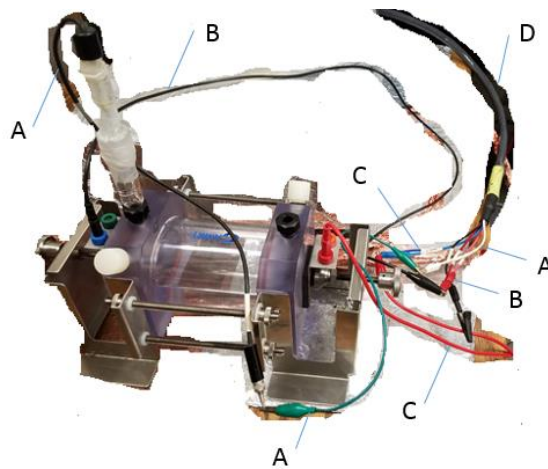


Figure 3: Corrosion Cell Attachment to EC Lab System includes A) Connection of Reference Electrode B) Connection of Anode, C) Connection of Cathode, D) Main line connecting to system.

Corrosion test data is collected on EC Lab software for Electrochemical Impedance (EIS) and Linear Polarization (LP). Prior to running corrosion tests, open circuit voltage (OCV) is confirmed to reach steady state. The system inputs are listed in Figure 4.

| | | | |
|---|-------------|------------------------------|---------------|
| General: | | Open Circuit Voltage: | |
| EC-Lab for windows v10.40 | | tR (h:m:s) | 1:10:0.0000 |
| CE vs. WE compliance -10 V to 10 V | | dtR (s) | 0.5000 |
| Ewe ctrl range:min -1.50 V, max 1.00 V | | E range min (V) | -1.500 |
| Electrode SA : 0.001 cm ² | | E range max (V) | 1.000 |
| Characteristic mass : 0.001 g | | | |
| Potential Electrochemical Impedance: | | Linear Polarization: | |
| fi | 100.000 kHz | dE/dt | 1.000 mV/s |
| ff | 10.000 mHz | Ei (V) | -1.100 |
| Sel Nd | 1 | EL (V) | 0.600 |
| Nd | 100 | record | I |
| Nt | 51 | dI | 0.000 μ A |
| Log | 1 | tI (s) | 0.5000 |
| Va (mV) | 10.0 | step percent | 100 |
| Na | 1 | N | 1 |
| E range min (V) | -1.500 | E range min (V) | -1.500 |
| E range max (V) | 1.000 | E range max (V) | 1.000 |
| I Range | Auto | I Range | Auto |
| Bandwidth | 5 | Bandwidth | 5 |

Figure 4: Inputs for Corrosion Testing

Materials tested include: 1) As made: bulk Cu, conventional Cu cold spray, nanomaterial Cu cold spray, and bulk CuO, 2) Annealed: bulk Cu, conventional Cu cold spray, nanomaterial Cu cold spray. For each test, the corrosion cell was washed with DI water before and after testing. Samples were sterilized in ethanol prior to testing. During testing 350mL of 3% (weight) NaCl solution was used. Corroded material samples were air dried and saved for further materials characterization. The cold sprayed samples were not thick enough to polish to eliminate oxides affecting the EIS test. EIS testing was only performed for the non-heat treated (non-HT) samples.

Data is collected and analyzed using EC Lab software. For EIS data, conventional and nanomaterial Cu cold spray samples were fitted to the equation: $R1+R2/C2+Q1$, which correspond to the diagram in Figure 5.

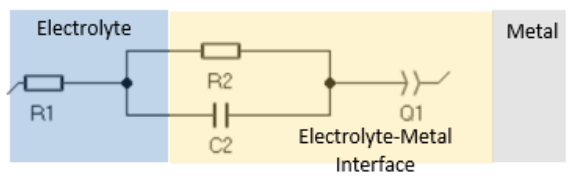


Figure 5: Equivalent Circuit for an Electrochemical Cell where R1 is solution resistance, R2 is charge transfer resistance, C2 is double layer capacitance, and Q1 is constant phase element [38].

The above diagram can be broken into three sections to consider what is happening in the electrolyte, at the electrolyte-metal interface, and at the metal. For the electrolyte, the solution resistance between the reference and working electrode must be considered. At the electrolyte-metal interface, the charge transfer resistance from metal ions diffusing into the electrolyte and the double layer capacitance from ions in solution adsorbing onto the electrode surface are both considered. Since capacitors in EIS experiments often do not behave in an ideal manner due to various factors, including sample surface roughness, a constant phase element is added to account for the variation. [18]

Bulk Cu samples were fitted to the equation: $R1+R2/C2+R3/C3+Q1$, where $R3/C3$ accounts for the passivation effect, as indicated by the semi-circle present on the Bulk Cu line in Figure 6. See the description in Figure 5 for further definition/explanation of equation components.

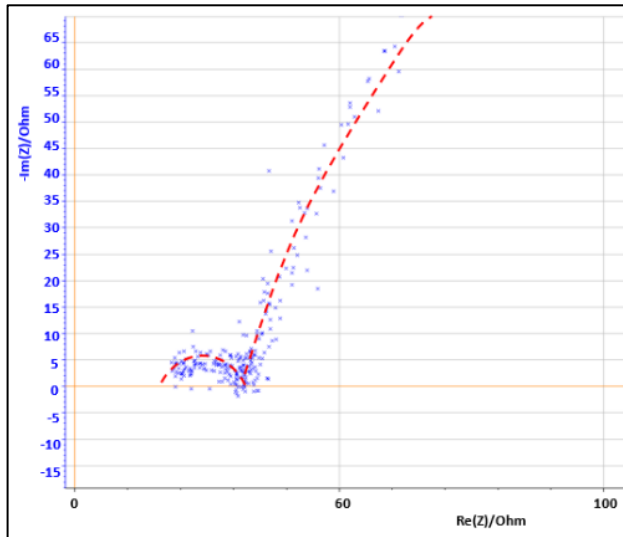


Figure 6: Magnified EIS data of Impedance vs. Resistance for Bulk Cu

Magnifying the EIS data for Bulk Cu shows that there is a small semi-circle followed by the beginning of a much larger semi-circle, with the first one representing the passivation zone for the material and the second being the beginning of the Nyquist plot. An expanded view of a notional Nyquist plot can be seen in Figure 7.

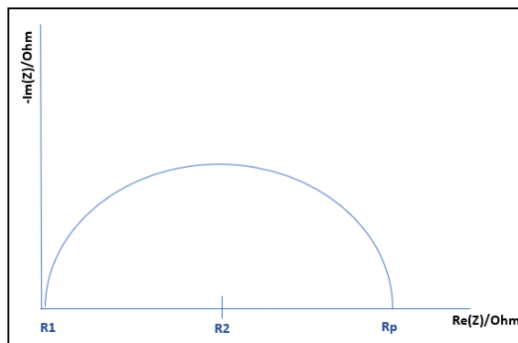


Figure 7: Nyquist Plot Diagram

Where R_1 and R_2 correspond to solution resistance and charge transfer resistance, respectively. And R_p represents the polarization resistance of the material undergoing corrosion. The smaller the diameter or R_p value, the higher the corrosion rate of the material. Ohm's law states that resistance is the ratio between voltage and current. Capacitance is the ratio between charge stored on the capacitor and electrical potential, making capacitance inversely proportional to resistance and directly proportional to corrosion rate. ^[4, 38, 26]

For LP data, all samples fit to a graph of electron potential vs. current density, as seen in Figure 8.

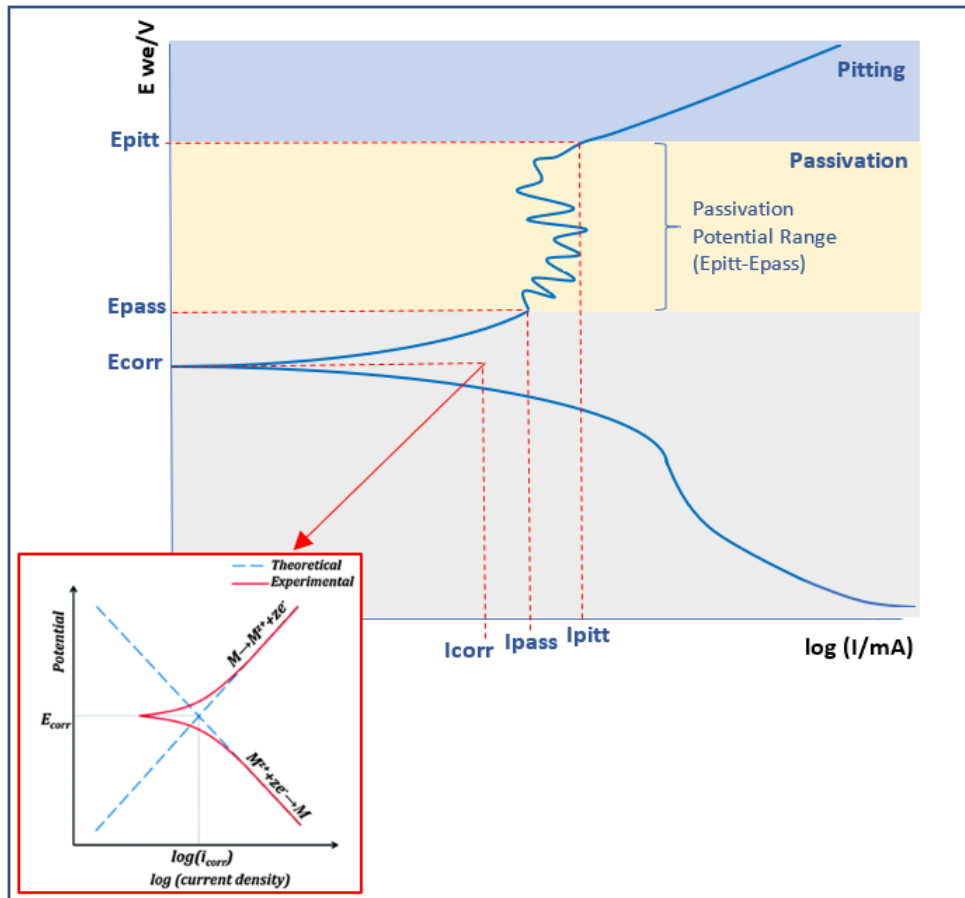


Figure 8: Linear Polarization Diagram [Modified from 33]

From the linear polarization plot the potential and current at the point of corrosion (E_{corr} and I_{corr}), passivation (E_{pass} and I_{pass}), and pitting (E_{pitt} and I_{pitt}) can be determined. Where, E_{corr} and I_{corr} are based on extrapolation of the slopes of the anode and cathode, as seen in the red box in Figure 8. [21, 33]

2.2.2 Cu Ion Release Assay

The release of soluble copper from cold sprayed samples was measured over 7 days. The release of copper ions (ppb) from Aluminum (Al), conventional Cu (CC) and nanomaterial Cu (nC) surfaces versus time (days) from 30min to 7 days, determined using inductively coupled plasma mass spectroscopy (ICP-MS) in samples diluted 100-fold in water. Points represent mean standard deviation of $n=3$ sample at a single time point; one way ANOVA ($p < 0.05$). Significance for copper release was found for nC samples between 1 hour and 7 days and for CC samples.

2.3. Composition + Microstructure Analysis

2.3.1. SEM

SEM was used to analyze the microstructure of consolidated conventional and nanomaterial cold spray coatings. Two orientations were studied – cross-section as well as top-down. Cross-sections are mounted in metallurgical epoxy mounts, then mechanically polished to a $0.05 \mu\text{m}$ finish for analysis. For cross-sections SEM analysis was performed in a Zeiss EVO MA-10 and for top-down samples the Joel JSM-7000F FE SEM at an accelerating voltage of 10 and 15 kV with both backscatter (BSE) and secondary (SE) electron detection. Cross-section samples were etched at 50/50 NI/DI H₂O for 10 seconds and 25/75 NI/DI H₂O for 5 seconds for conventional and nanomaterial Cu respectively and re-imaged. All bulk Cu cross-sections were etched using the same parameters as the conventional Cu.

EDS was performed using ESPRIT software with the Zeiss SEM for cross-sectioned samples. Oxford Instruments software was used with the JEOL 7000 FE SEM for top-down samples. Software ran for 5 minutes prior to data collection, and dead time ranged from 2-5%. A rate of 20 kilocounts was used for the SEM and ~3000 counts per second for the FE SEM.

2.3.1. XRD

WPI's PANalytical Empyrean X-ray Diffraction machine was used with a Cu tube and Ni filter from 20 to 140 2theta at 45Kv and 40Ma, with a ½ degree divergence slit, 1 degree anti-scatter slit, 0.04 radian soller slit, and 10mm mask. Due to the thin Cu cold spray coating thickness (50um or less), the time per step was increased to 100 seconds per step. Prior to running, the depth was checked with a goniometer and a depth of 1 was confirmed.

Results were collected and analyzed using DataViewer and HighScore Plus software. Results were compared against reference PDF4database, with PDFs 00-004-0836, 00-005-0061, 00-005-0667 for Cu, CuO, and Cu₂O, respectively. Data was collected for top-down measurement of the corroded area of the samples.

2.3.3. XPS

Due to the high amounts of carbon contamination, left by cutting fluids and corrosion testing, attempts were made to delicately clean the copper surfaces. Prior to analysis by XPS, all samples were sequentially sonicated in acetone then isopropanol for 5 minutes each. Cleaning with water and detergents was avoided as to not affect the surface chemistry being probed.

A PHI5600 XPS system with a third-party data acquisition system (RBD Instruments, Bend Oregon) acquired all photoelectron spectra as detailed previously ^[9]. Analysis chamber base pressures were $<1 \times 10^{-9}$ Torr. A hemispherical energy analyzer that was positioned at 90° with respect to the incoming monochromated Al K α X-ray flux and 45° with respect to standard sample positioning collected the photoelectrons. Survey spectra utilized a 117 eV pass energy, a 0.5 eV step size, and a 50-ms-per-step dwell time. High-resolution XP spectra employed a 23.5 eV pass energy, 0.025 eV step size, and a 50 ms dwell time per step. Spectra were acquired for the Al 2s, Al 2p, C 1s, Cu 2p, N 1s, and O 1s photoelectron regions as well as the Cu LMM Auger region. Post-acquisition data fitting employed Shirley-style baselines to all spectra based on a qualitative visual assessment of baseline shape. For a given oxidation state, fits that employ multiple peaks within a spectral region utilized identical fwhm (full width and half max) values for each peak to minimize mathematically optimized but possibly chemically unrealistic fits ^[16]. All areas were fit with GL(30) pseudo-Voigt peak functions except for features in the Cu 2p region that employed GL(70) functions. Lastly, Cu 2p features ascribed to Cu⁰ and to Cu¹⁺ utilized an asymmetric tail function.

3. Results and Discussion

3.1. Corrosion

EIS data, in Figure 9, shows that nanomaterial Cu cold spray has a greater corrosion rate than that of conventional Cu cold spray. And that bulk Cu has a corrosion rate that is greater than both conventional and nanomaterial Cu cold spray.

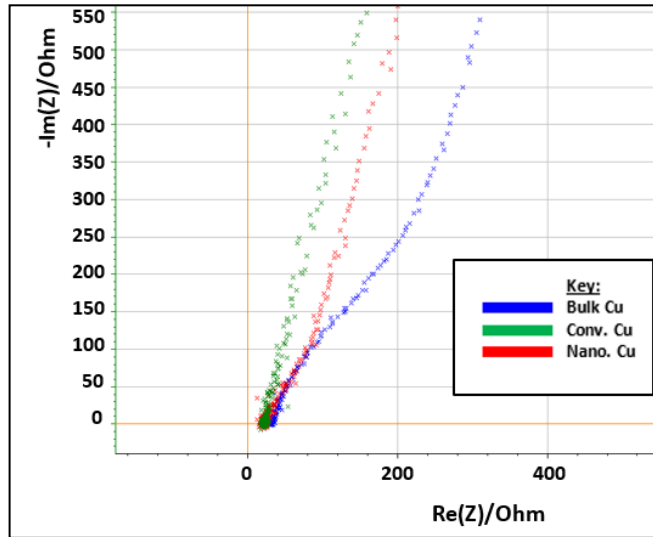


Figure 9: EIS Data in impedance vs. resistance

EC Lab Software is able to find a line of best fit for each data set with values for charge transfer resistance (R_2) and double layer capacitance (C_2) in Table 1.

Table 1: EIS Data Outputs

| Sample: | R_2 (Ohms) | C_2 (F) |
|-----------------|--------------|-----------|
| Conventional Cu | 467.5 | 0.0164 |
| Nanomaterial Cu | 382.5 | 0.1057 |
| Bulk Cu | 325 | 0.124 |

As resistance decreases there is an increase in capacitance, where capacitance is directly proportional to corrosion rate. [4, 38, 26] Bulk Cu has the lowest resistance and highest capacitance, followed by nanomaterial Cu and conventional Cu, respectively. LP data, in Figure 10, supports EIS results.

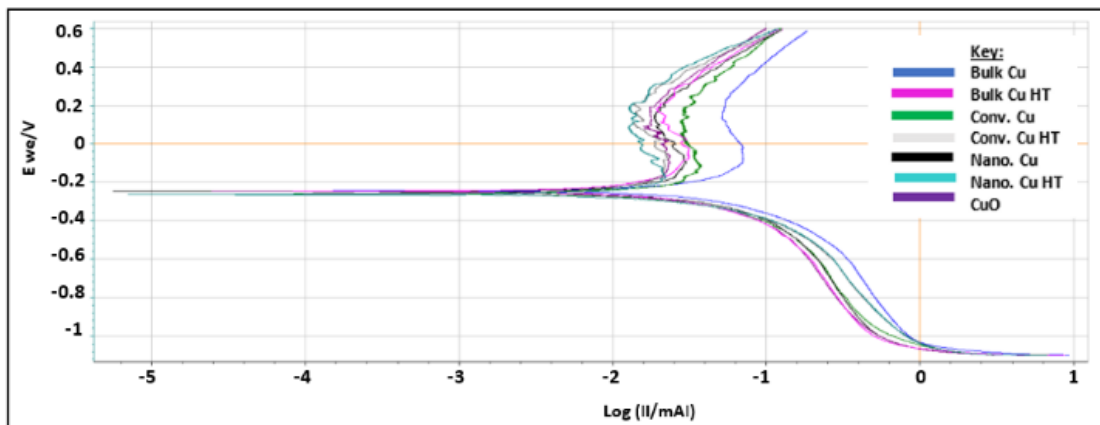


Figure 10: Linear Polarization Data

At first glance, the above data appears, with the exception of Bulk Cu as an outlier to the right (blue line on the graph). Upon further analysis, differences are seen between the samples as detailed in Table 2.

Table X: Linear Polarization Data Analysis

| Samples: | E_{corr} (we/V) | I_{corr} (I/mA) | E_{pass} (we/V) | I_{pass} (I/mA) | E_{pitt} (we/V) | I_{pitt} (I/mA) | Passivation Potential Range ($E_{pitt}-E_{pass}$) |
|------------|----------------------|----------------------|----------------------|----------------------|----------------------|----------------------|--|
| Bulk Cu | -0.25 | $10^{-1.7}$ | -0.14 | $10^{-1.3}$ | 0.26 | $10^{-1.22}$ | 0.40 |
| Conv Cu CS | -0.25 | $10^{-2.3}$ | -0.2 | $10^{-1.6}$ | 0.27 | $10^{-1.42}$ | 0.47 |
| Nano Cu CS | -0.25 | $10^{-2.1}$ | -0.18 | $10^{-1.59}$ | 0.28 | $10^{-1.3}$ | 0.46 |
| CuO | -0.25 | $10^{-2.35}$ | -0.18 | $10^{-1.77}$ | 0.28 | $10^{-1.6}$ | 0.46 |
| Bulk Cu HT | -0.25 | $10^{-2.95}$ | -0.19 | $10^{-1.75}$ | 0.29 | $10^{-1.59}$ | 0.48 |
| Conv Cu HT | -0.25 | $10^{-2.8}$ | -0.18 | $10^{-1.7}$ | 0.30 | $10^{-1.5}$ | 0.48 |
| Nano Cu HT | -0.25 | $10^{-2.78}$ | -0.19 | $10^{-1.69}$ | 0.31 | $10^{-1.63}$ | 0.50 |

The I_{corr} , I_{pass} , and I_{pitt} values vary from highest to lowest with the sample order being: bulk Cu, nanomaterial Cu, conventional Cu, and heat treated samples. This supports the EIS data showing bulk Cu to be the least corrosion resistant, as it has the highest current density, and passivation values. It also has the lowest passivation potential range. Nanomaterial Cu also has a higher corrosion rate than conventional Cu, which is expected as the nanoparticles present in the coating provide a greater percentage of grain boundaries for ion diffusion [39]. Bulk Cu performed worse than nanomaterial Cu, in that it had a higher corrosion rate. This may be due to bulk Cu not being manufactured using cold spray technology, which provides denser coatings with minimal oxides and inclusions [39]. Microstructure and hardness analysis in the following section can confirm this. Additionally, it is possible that the nanomaterial Cu was able to form a passive layer more rapidly than that of bulk Cu, for which the I_{pass} values show this to be true. [3]

Ion release assay data supports both EIS and LP test results, as seen in Figure 11.

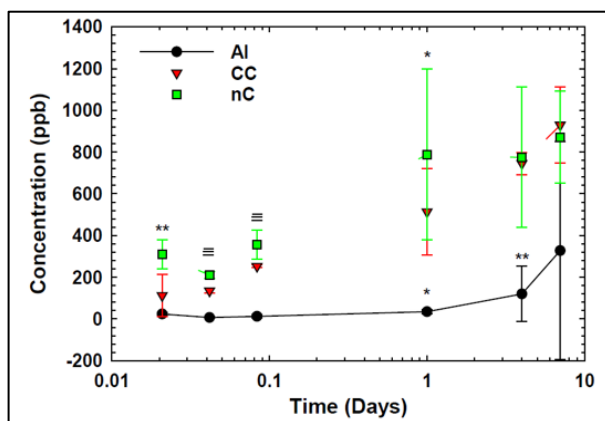


Figure 11: Cu Ion Release Assay for nanomaterial Cu (nC) and Conventional Cu (CC) with aluminum (Al) control

Results show Nanomaterial Cu to have greater ion concentration in solution than conventional Cu. The timepoint of greatest interest is the 2hour mark, as this is the timepoint used in the EPA approved efficacy protocol. While both Cu materials released significant ($p < 0.05$) amounts of ions into solution over aluminum controls, nanomaterial Cu demonstrated greater cumulative ion release at all time points tested through 1 day, including at the 2 hour timepoint.

Corrosion testing shows nanomaterial Cu to have a greater corrosion rate, and subsequently greater ion release than conventional Cu. This supports prior work done with nanomaterial Cu performing better than conventional Cu in the contact killing of Influenza A Virus [39]. The next section will look at the differences in microstructure between the two coatings to further explain why nanomaterial Cu is able to have a faster ion release rate.

3.3. Microstructure

Micrographs of top-down as made and corroded conventional, nanomaterial, and bulk Cu are in Figure 12.

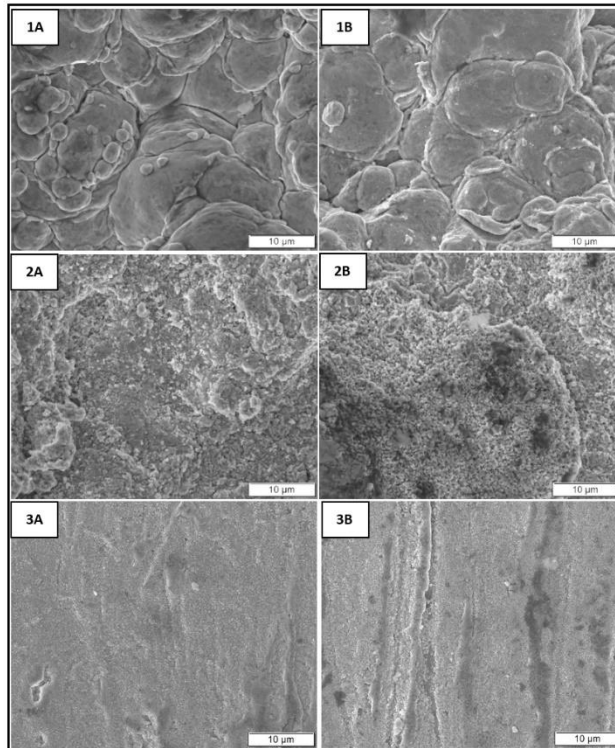


Figure 12: FE SEM top-down micrographs of as made (A) and corroded (B) conventional (1), nanomaterial (2), and bulk (3) Cu.

Conventional Cu micrographs show larger grains compared to nanomaterial Cu. Both appear to have smaller, more defined grain structure as compared to bulk Cu. The corroded samples show pitting in the nanomaterial and bulk Cu samples, with the later having larger corroded areas. The heat treated samples (see supplemental A) show similar differences in microstructure and corrosion patterns.

Cross-sections of the conventional, nanomaterial, and bulk Cu are show in Figure 13. The conventional Cu appears to have the largest grains, followed by bulk Cu, and then nanomaterial Cu. While nanomaterial Cu has the smallest grains, it also appears to have the most diverse distribution of grain size with grains ranging in nanometers to microns in size. This is characteristic of the powder production process where nano-particles are spray dried into agglomerate structures using conventional Cu binder.

Cold spray produces high density coatings with little to no oxides and inclusions ^[13]. Compared to the conventional and nanomaterial Cu cold spray coatings, bulk Cu shows much greater porosity. There is no visible corrosion in these micrographs, confirming that the electrochemical testing assayed only the near surface region.

The heat treated samples (supplemental A) show similar differences on microstructure as the non-heat treated samples. They also show no difference between as-made and corroded samples.

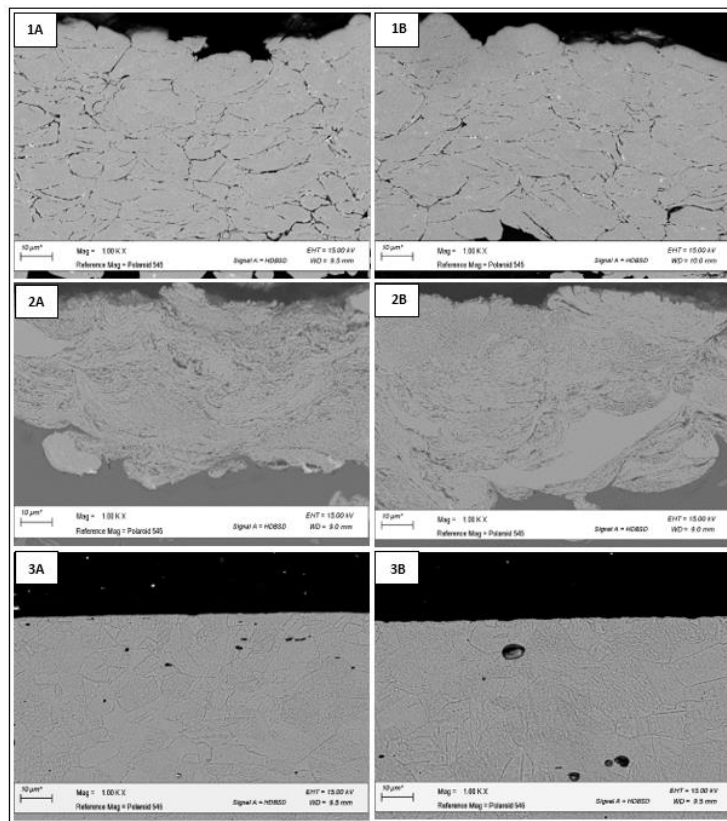


Figure 13: SEM cross-section micrographs of as made (A) and corroded (B) conventional (1), nanomaterial (2), and bulk (3) Cu.

3.3. Composition

3.3.1. EDS

See Supplemental Section B for top-down EDS data. All data shows that both as made and corroded samples have Cu and Oxygen present. Some samples have remnants of NaCl from the liquid used in the electrochemical cell during testing.

For cross-sections, all results showed predominantly Cu with minimal oxygen content. No differentiation was able to be made between the corroded and non-corroded areas of the sample. This is most likely do to the fact that the electrochemical testing only affected the topmost atomic layers of the samples.

3.3.2. XRD

Diffraction peaks for all the corroded samples are seen in Figure 14. All peaks matched to Cu (pdf 00-004-0836) with the exception of the 1st peak, which matched to Cu₂O (pdf 00-005-0667).

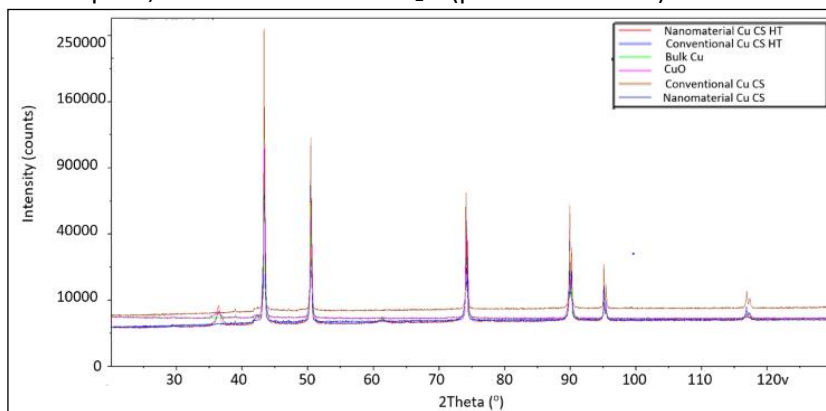


Figure 14: XRD of corroded samples.

3.3.3. XPS

XPS data for as made and corroded conventional, nanomaterial, and bulk Cu is in Figure 15. The as made bulk Cu sample spectra was limited due to sample contamination.

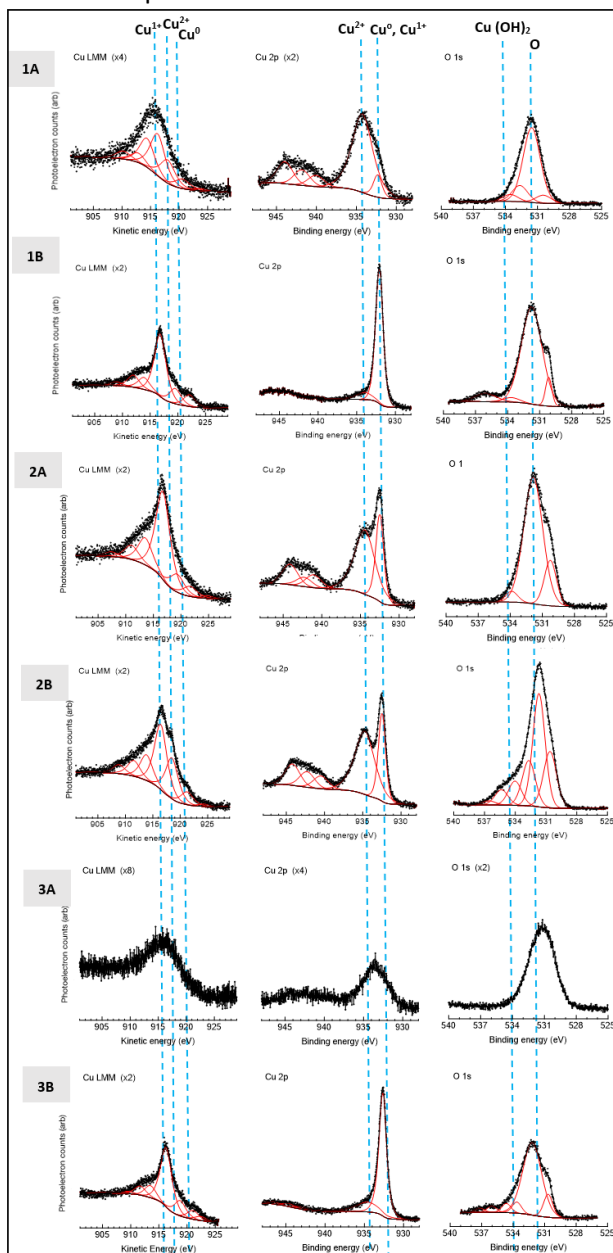


Figure 15. XPS from left to right: Auger electron spectra of the Cu LMM region, XP spectra of the Cu 2p_{3/2} region, XP spectra of O. For as-made (1A) and corroded (1B) conventional Cu. For as-made (2A) and corroded (2B) nanomaterial Cu. For as made (3A) and corroded (3B) bulk Cu. The dashed lines represent the location of each species.

Figure 15 represents spectra for the Auger Cu LMM and XP Cu 2p regions for both conventional and nanomaterial copper surfaces. The photoelectron features ascribed to Cu⁰ and Cu¹⁺ occur at overlapping binding energies, which necessitates the combination of Auger and photoelectron spectra to elucidate oxidation state information. For XP, Cu²⁺ dominates the photoelectron spectra for as made conventional copper, but Cu⁰ and Cu¹⁺, dominate for all other samples. The Auger spectra deconvolve the contribution of Cu⁰ and Cu¹⁺. The dashed lines in the Auger graphs represent peak energy locations of each oxidation state of copper in oxides. This shows all surfaces to be dominated by Cu¹⁺ but contain significant quantities of Cu²⁺ rather than Cu⁰. For all corroded samples, it appears that there is a greater presence of Cu¹⁺ vs. Cu²⁺ as compared to the non-corroded samples. The XP spectra for O

shows strong presence of oxygen, as well as some Cu hydroxide, with greater amounts of the later in the corroded samples. XPD results for heat treated samples are in supplemental section C, with similar results to the above.

The Cu LMM spectra of corroded and textured copper surfaces can contain many peaks which can make quantitative interpretation increasingly difficult. The auger spectra helped in the identification but it was hard to get much more detail as there was a lot of carbon present on the samples. No attempt was made to sputter clean the samples as this may have reduced the copper on surface. Consequently, this contamination attenuates photoelectron signals from the underlying substrate causing the relevant peaks in the Cu LMM spectra to broaden and decrease overall resolution. Additionally the nanoparticles can cause peak broadening in the sample which may decrease resolution. So while comparison can be made between samples for the type of species present, comparison has not been made between the differences in intensity between the samples. ^[5, 14]

XPS data provides interesting insight into the kind of Cu oxide species present, Cu₂O, and confirms pourbaix diagram predictions. It also raises the question of how Cu₂O came to be the dominant species based on environmental factors and how the presence of different species may affect material antimicrobial properties. Follow-on work is needed to uncouple the effects of different Cu species on the contact killing of various microbes.

4. Conclusion

In conclusion,

- 1) Nanomaterial Cu has a higher corrosion rate than conventional Cu.
- 2) Nanomaterial Cu has smaller grain size and consequently greater percent grain boundaries than conventional Cu, expected to lead to increased ion release which contributes to increased corrosion rate.
- 3) Since the main antimicrobial mechanism of Cu is through contact killing, it follows that increased ion release and corrosion rate of nanomaterial Cu contributes directly to its increased antimicrobial effectiveness in the contact killing of Influenza A Virus as compared to conventional Cu ^[39].
- 4) XRD and XPS show sample composition to be of pure Cu and Cu oxides, with XPS determining the dominant Cu oxide present to be Cu₂O.
- 5) Follow-on work is needed to determine if the presence of different oxide species varies Cu kill-rate.
- 6) Additional work should also be done to quantify the energetics of nanomaterial versus conventional Cu cold spray for grains, grain boundaries, and subsequent transport phenomena.

Acknowledgement

A special thanks to WPI Department of Chemistry and Biochemistry for X-ray Photoelectron Spectroscopy testing. Thank you to Surface Combustion for the heat treated samples and WPI's Chemical Engineering Department for the Cu Ion Release Assay.

References

- [1] Askeland D, Fulay P, Wright W. "The Science and Engineering of Materials". United States: Cengage Learning. 2011. 6th ed.
- [2] Balasubramanian, R., and A. C. Rosenzweig. 2008. Copper Methanobactin: A Molecule Whose Time has Come. *Curr. Opin. Chem. Biol.* 12:245–249.
- [3] Balyanov A, et al., "Corrosion resistance of ultra fine-grained Ti", *Scripta Materialia* 51 (2004) 225–229.
- [4] Bard A, Faulkner L. "Electrochemical Methods: Fundamentals and Applications". United States: Wiley. 2001.
- [5] Biesinger M. "Advanced analysis of copper X-ray photoelectron spectra". *Surf. Interface Anal.* 2017, 49, 1325–1334.
- [6] Boone SA, Gerba CP (2007) Significance of fomites in the spread of respiratory and enteric viral disease. *Appl Environ Microbiol* 73: 1687-1696.

- [7] Bott R., Bowmaker G., and Davis C..1997.Crystal Structure of $[Cu_4(tu)_7](SO_4)_2 \cdot H_2O$ and Vibrational Spectroscopic Studies of Some Copper(I) Thiourea Complexes. *Inorg. Chem.* 37: 651-657
- [8] Callister W, Rethwisch D. "Materials Science and Engineering: An Introduction". United States:Wiley.10th ed. 2018
- [9] Carl, A. D.; Kalan, R. E.; Obayemi, J. D.; Zebaze Kana, M. G.; Soboyejo, W. O.; Grimm, R. L., Synthesis and Characterization of Alkylamine-Functionalized Si (111) for Perovskite Adhesion With Minimal Interfacial Oxidation or Electronic Defects. *ACS Appl. Mater. Interfaces* 2017, 9 (39), 34377-34388.
- [10] Carvalho M. "Corrosion of copper alloys in natural seawater : effects of hydrodynamics and pH. Analytical chemistry". Université Pierre et Marie Curie - Paris VI, 2014.
- [11] Casey, A. L., et al. 2010. Role of copper in reducing hospital environment contamination. *J. Hosp. Infect.* 74:72–77.
- [12] Center for Disease Control Prevention. Electron Micrograph of Methicillin-Resistant *Staphylococcus aureus*(MRSA).http://faculty.ccbcmd.edu/courses/bio141/lecguide/unit1/shape/EM_MRSA_staph.html
- [13] Champagne V, Helfritch D (2013) A demonstration of the antimicrobial effectiveness of various copper surfaces. *Journal of Biological Engineering* 7:8.
- [14] Dabera G, et al., "Retarding oxidation of copper nanoparticles without electrical isolation and the size dependence of work function" *Nature Communications* volume 8, Article number: 1894 (2017)
- [15] Espirito Santo, C., N. Taudte, D. H. Nies, and G. Grass. 2008. Contribution of copper ion resistance to survival of *Escherichia coli* on metallic copper surfaces. *Appl. Environ. Microbiol.* 74:977–986.
- [16] Fairley, N. Peak Fitting in XPS. (accessed May 18 2017)http://www.casaxps.com/help_manual/manual_updates/peak_fitting_in_xps.pdf
- [17] Feng Y, Siow K, Teo W, Tan K, Hsieh A, "Corrosion Mechanisms and Products of Copper in Aqueous Solutions at Various pH Values", *Corrosion* 53 (1997) 389-398.
- [18] Gamry Instruments. "Basics of Electrochemical Impedance Spectroscopy". 2019. Access 04/03/19.<https://www.gamry.com/application-notes/EIS/basics-of-electrochemical-impedance-spectroscopy/>
- [19] Grass G., Rensing C., and Solioz M. 2011. Metallic Copper as an Antimicrobial Surface. *Applied and Environmental Microbiology.* 77: 1541–1547.
- [20] Johnson G., Cook W., Fracture Characteristics of Three Metals Subjected to Various Strains, Strain Rates, Temperatures, and Pressures". *Engineering Fracture Mechanics* Vol. 21, No. 1, pp. 3148. 1985
- [21] Jones D. "Principles and Prevention of Corrosion". New Jersey: Prentice Hall. 1996. 2nd ed.
- [22] Lee F, Wang D, Chen L, Kung C, Wu Y, et al. (2013) Antibacterial nanostructured composite films for biomedical applications: microstructural characteristics, biocompatibility, and antibacterial mechanisms. *Biofouling* 29: 295-305.
- [23] Lemire J., Harrison J., and Turner R.. 2013. Antimicrobial activity of metals: mechanisms, molecular targets and applications. *Microbiology.* 11:371-384
- [24] Libre Texts, "Chemistry: Aqueous Solution of Salts" Department of Education. Accessed 04/01/19. [https://chem.libretexts.org/Bookshelves/Physical_and_Theoretical_Chemistry_Textbook_Maps/Supplemental_Modules_\(Physical_and_Theoretical_Chemistry\)/Acids_and_Bases/Acids_and_Bases_in_Aqueous_Solutions/Aqueous_Solutions_Of_Salts](https://chem.libretexts.org/Bookshelves/Physical_and_Theoretical_Chemistry_Textbook_Maps/Supplemental_Modules_(Physical_and_Theoretical_Chemistry)/Acids_and_Bases/Acids_and_Bases_in_Aqueous_Solutions/Aqueous_Solutions_Of_Salts)
- [25] Liptakova T, et al., "Assessment of Corrosion Behavior of Copper Pipelines System under

- Flowing Condition". International Conference on Computer Design and Engineering (ICCDE 2012). 2012.V49.24
- [26] Li W, Hu L, Zhang S, Hou B. "Effects of two fungicides on the corrosion resistance of copper in 3.5% NaCl solution under various conditions". *Corrosion Science* 53 (2011) 735–745
- [27] Malik R, Burch D, Bazant M, Ceder G, " Particle Size Dependence of the Ionic Diffusivity". *Nano Lett.* 2010, 10, 4123–4127
- [28] Murthy P, Venugopalan V, " Antibiofilm Activity of Nano sized CuO". *IEEE.* 2011. 580-583.
- [29] Noyce JO, Michels H, Keevil CW (2007) Inactivation of influenza A virus on copper versus stainless steel surfaces. *Appl Environ Microbiol* 73: 2748-2750.
- [30] Pereda-Ayo B., Torre U. , and Josellian-Gomez M. 2013. Role of the different copper species on the activity of Cu/zeolite catalysts for SCR of NO_x with NH₃. *Applied Catalysis B: Environmental.* 147(5) : 420-428.
- [31] Praxair: surface technologies. Powder Solutions: product brochure. www.praxairsurfacetechologies.com.
- [32] Principles of General Chemistry. Chapter 23: "The d-Block Elements". 2012. [online]. Available:<https://2012books.lardbucket.org/books/principles-of-general-chemistry-v1.0/s27-the-d-block-elements.html>. Assessed October 2017.
- [33] Ramachandran R, Nosonovsky M. " Coupling of surface energy with electric potential makes superhydrophobic surfaces corrosion-resistant". *Phys. Chem. Chem. Phys.*, 2015, 17, 24988-24997.
- [34] Rapid reference to influenza. *The influenza virus: structure and replication.* Elsevier Ltd.
- [35] Rizvi M., Akhoun S., Maqsood S. 2013. Synergistic Effect of Perchlorate Ions and Acetonitrile Medium Explored for Extension in Copper Redoximetry. *Journal of Analytical Chemistry.* 70(5):633–638.
- [36] Rizvi M. "Complexation Modulated Redox Behavior of Transition Metal Systems (Review)". *Russian Journal of General Chemistry.* 85(4):959–973
- [37] Rolfe S, (2014) email conversation and Phase I SBIR Final Report, "Advanced Nanostructured Powders for Cold Spray Applications", Eltron Research and Development Inc., 4600 Naytilus Court South Boulder, CO 80301-3241
- [38] Scully J, Silverman D, Kendig M. "Electrochemical Impedance: Analysis and Interpretation". Philadelphia: ASTM, 1993, p37-53.
- [39] Sundberg, K., Champagne, V., McNally, B., Helfritsch, B., Sisson, R., "Effectiveness of Nanomaterial Copper Cold Spray Surfaces on Inactivation of Influenza A Virus," *J Biotechnology and Biomaterials*, 5 (4). 2015.
- [40] Sundberg K, Gleason M, Haddad B, Champagne V, Brown C, Sisson R, Cote D. " The Effect of Nano-Scale Surface Roughness on Copper Cold Spray Inactivation of Influenza A Virus". *Journal TBD.*
- [41] Sundberg K, Sousa B, Schreiber J, Walde C, Sisson R, Cote D. "Modeling Copper Cold Spray Single-Particle Impact for Optimized Antimicrobial Coatings". *Journal TBD.*
- [42] Sundberg K, Wald C, Sousa B, et al., "Microstructural Characterization of Conventional and Nanomaterial Copper Cold Spray Coatings". *Journal TBD.*
- [43] Varadwaj P., Varadwaj A., and Jin B. 2015. Ligand(s)-to-metal charge transfer as a factor controlling the equilibrium constants of late first-row transition metal complexes: revealing the Irving–Williams thermodynamical series. *Phys.Chem.Chem.Phys.* 17: 805-811.

[44] Verran J, Boyd R (2000) The Relationship Between Substratum Surface Roughness and Microbiological and Organic Soiling: a Review. *Biofouling* 17: 59-71.

[45] Walkowicz M, et al., "Impact of oxidation of copper and its alloys in laboratory-simulated conditions on their antimicrobial efficiency". *Corrosion Science* 140 (2018) 321–332

[46] Wang D, Xiang B, Liang Y, Song S, Liu C. "Corrosion control of copper in 3.5 wt.% NaCl Solution by Domperidone: Experimental and Theoretical Study". *Corrosion Science* 85 (2014) 77–86

Supplemental Section A: Heat Treat Micrographs

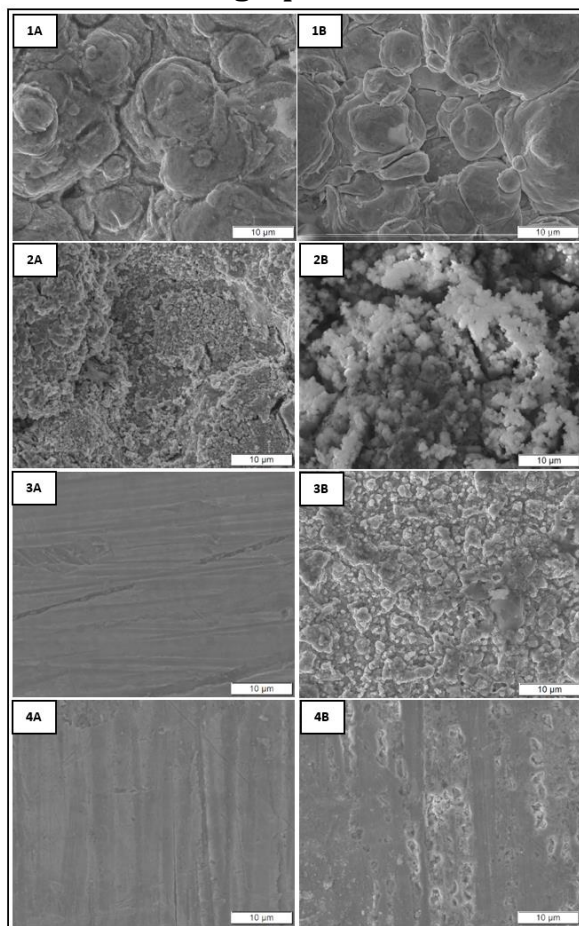


Figure X: FE SEM top-down images of as made (A) and corroded (B) heat treated conventional Cu (1), heat treated nanomaterial Cu (2), heat treated bulk Cu (3), and CuO (4).

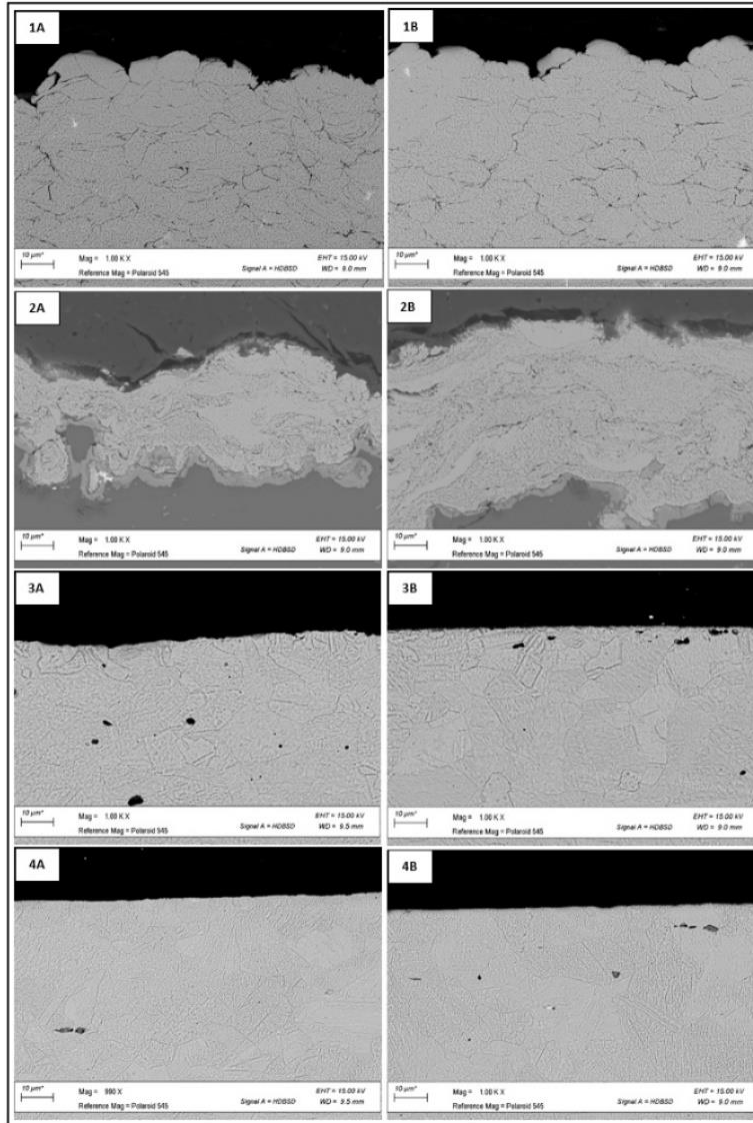


Figure X: SEM cross-section micrographs of as made (A) and corroded (B) heat treated conventional Cu (1), heat treated nanomaterial Cu (2), heat treated bulk Cu (3), and CuO.

Supplemental Section B: top-down EDS for all Samples

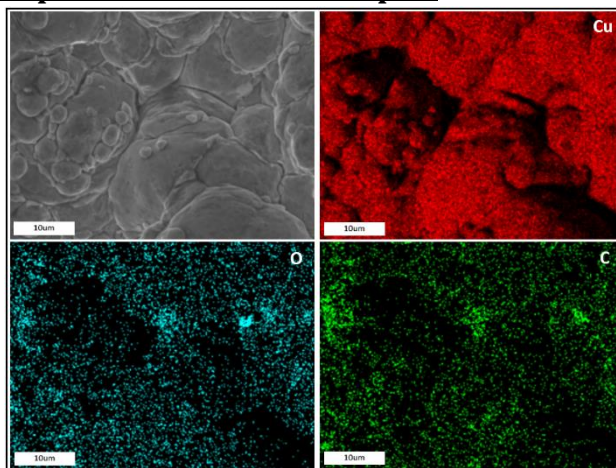


Figure X: EDS top-down As Made Conventional Cu

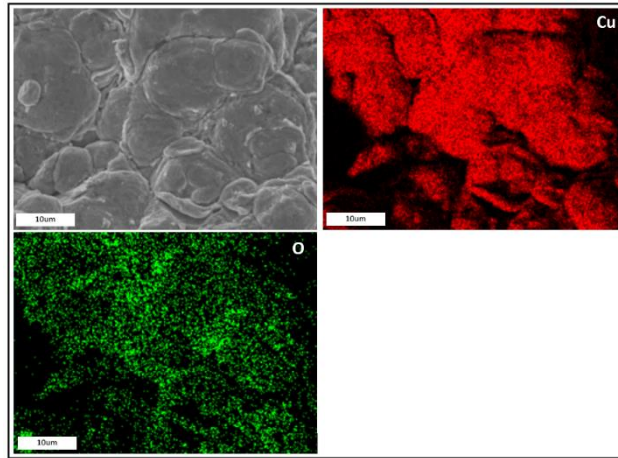


Figure X: EDS top-down Corroded Conventional Cu

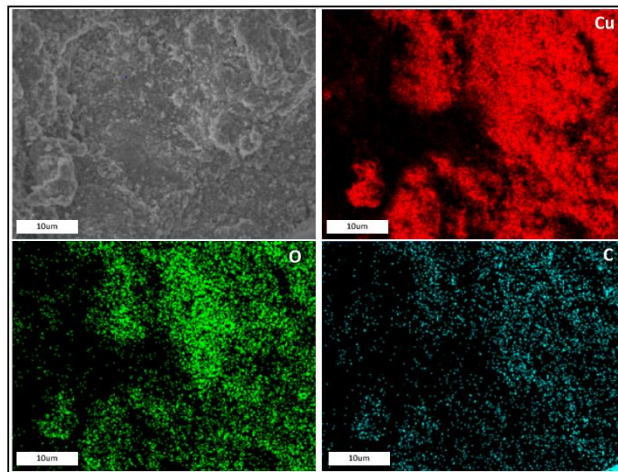


Figure X: EDS top-down As Made Nanomaterial Cu

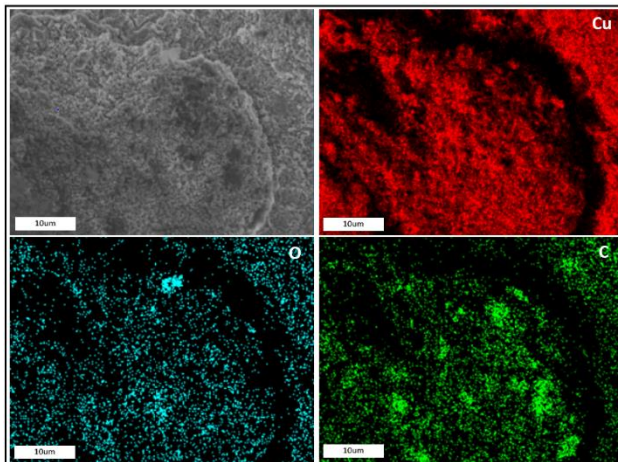


Figure X: EDS top-down Corroded Nanomaterial Cu

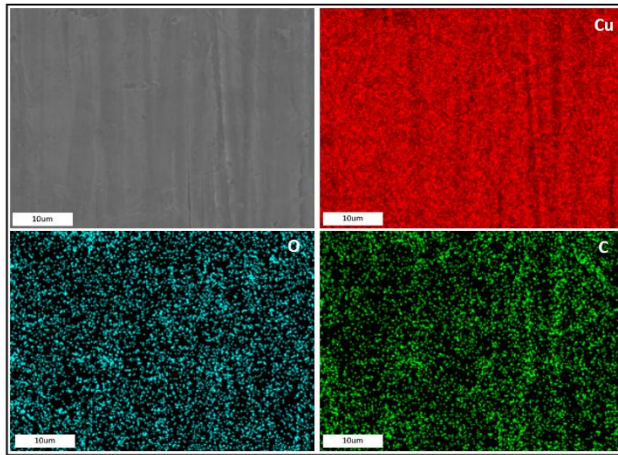


Figure X: EDS top-down As Made Bulk Cu

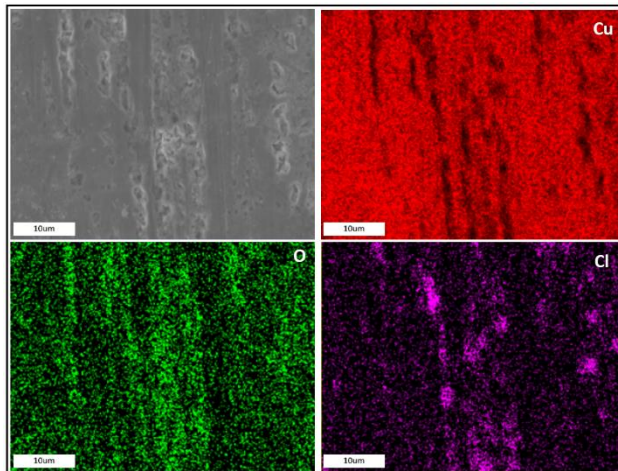


Figure X: EDS top-down Corroded Bulk Cu

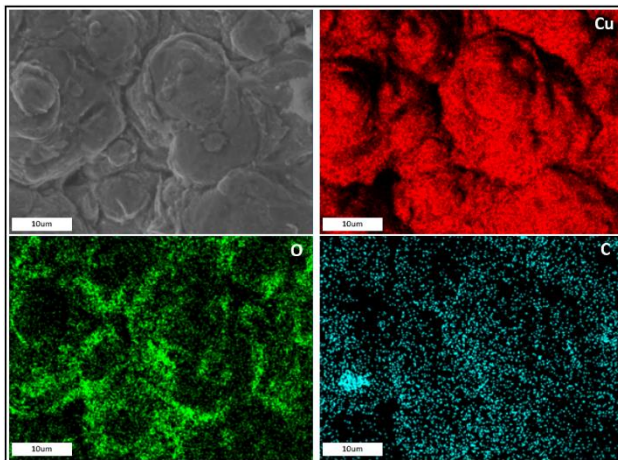


Figure X: EDS top-down As Made Heat Treated Conventional Cu

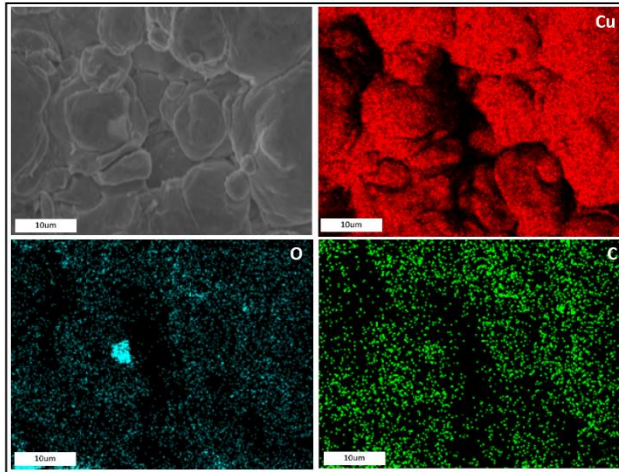


Figure X: EDS top-down Corroded Heat Treated Conventional Cu

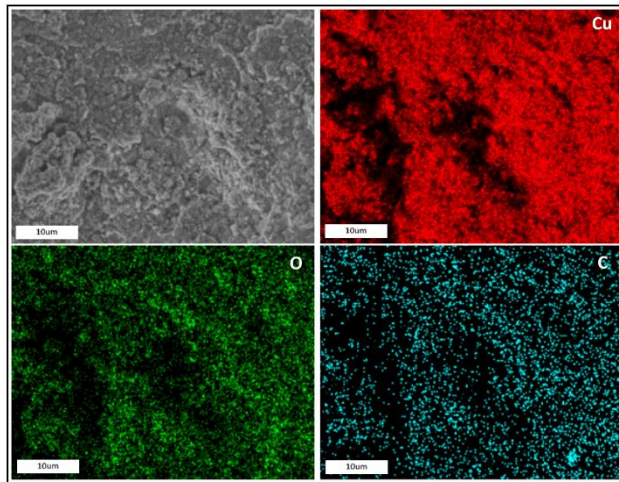


Figure X: EDS top-down As Made Heat Treated Nanomaterial Cu

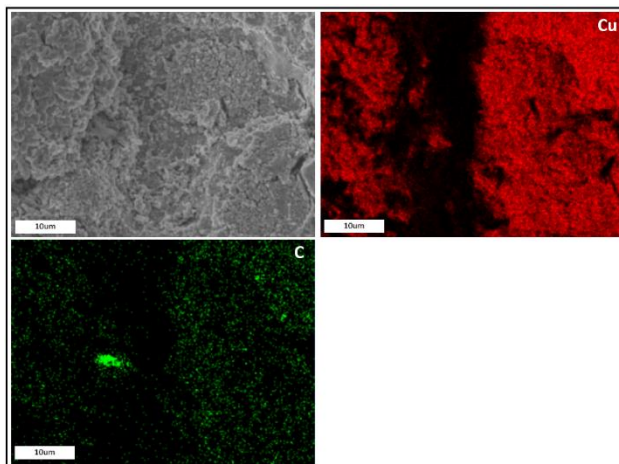


Figure X: EDS top-down Corroded Heat Treated Nanomaterial Cu

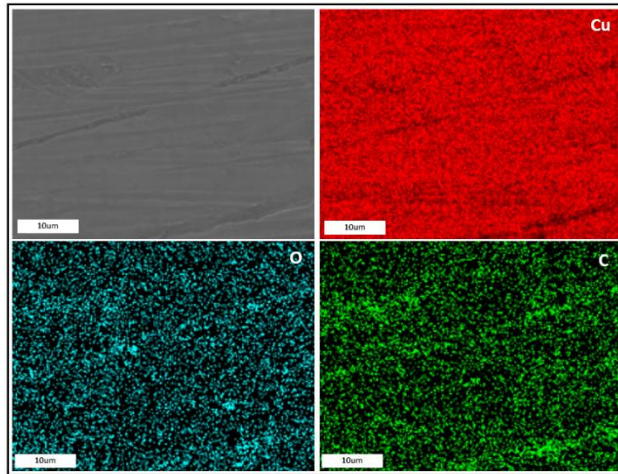


Figure X: EDS top-down As Made Heat Treated Bulk Cu

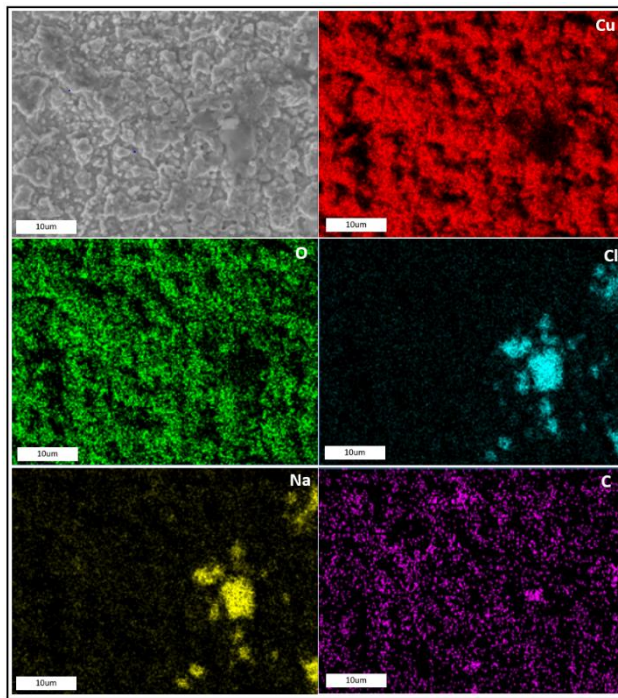


Figure X: EDS top-down Corroded Heat Treated Bulk Cu

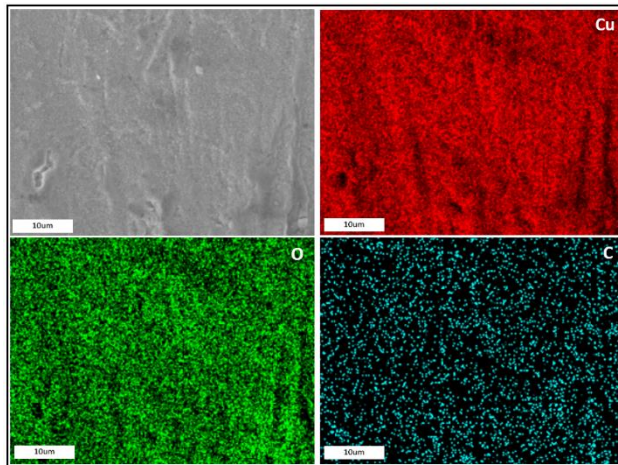


Figure X: EDS top-down As Made CuO

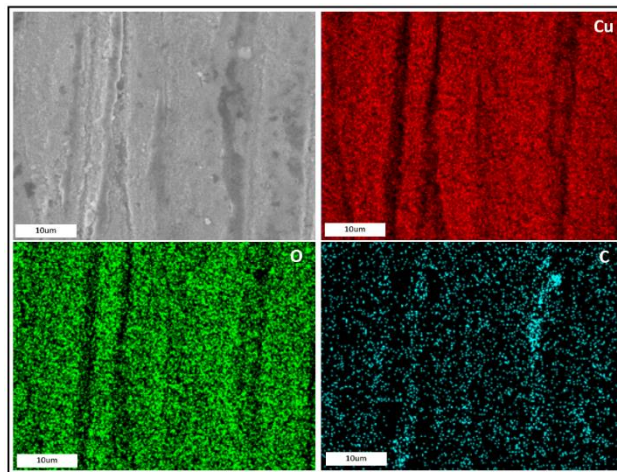


Figure X: EDS top-down Corroded CuO

Supplemental Section C: XPS Data for Heat Treated Samples

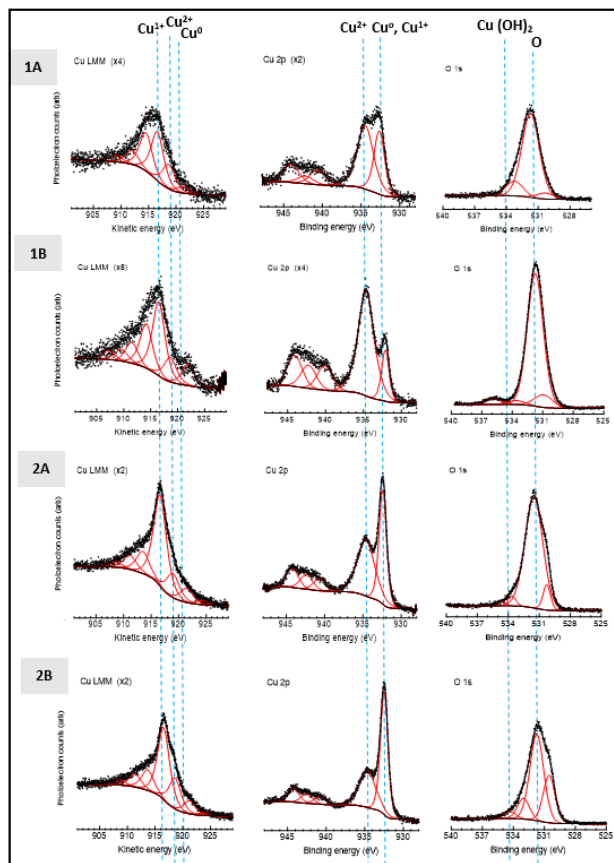


Figure X. XPS from left to right: Auger electron spectra of the Cu LMM region, XP spectra of the Cu 2p_{3/2} region, XP spectra of O. For as-made (1A) and corroded (1B) heat treated conventional Cu. For as-made (2A) and corroded (2B) heat treated nanomaterial Cu. The dashed lines represent the location of each species.

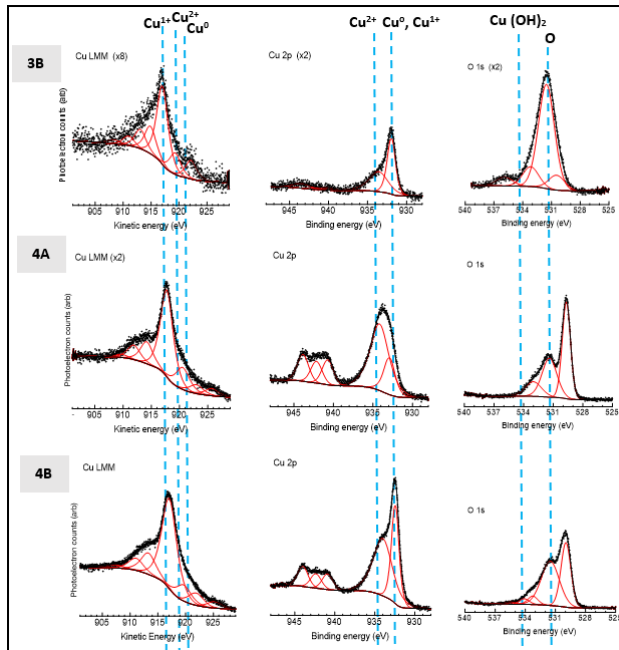


Figure X. XPS from left to right: Auger electron spectra of the Cu LMM region, XP spectra of the Cu 2p_{3/2} region, XP spectra of O. There is no 3A for as made since the sample had too much carbon on it, corroded (3B) for heat treated Bulk Cu. For as-made (4A) and corroded (4B) CuO. The dashed lines represent the location of each species.

7. Conclusion

1] Nanomaterial Cu cold spray has greater surface roughness at the scale of Influenza A Virus than that of conventional Cu cold spray.

2] Preliminary models show cold spray powder particle impact for conventional Cu. Follow-on work is needed to perfect the model for nanomaterial Cu. Single-splat and laser induce projectile impact testing support morphology and impact predictions from the models.

3] Microstructure shows nanomaterial Cu to have smaller grain size than conventional Cu. Hardness measurement supports this, showing nanomaterial Cu to have greater hardness values for both top-down and cross-section measurements.

4] Nanomaterial Cu has greater corrosion rate and Cu ion release rate than conventional Cu. Follow-on work is needed to quantify surface energetics at grains and boundaries to support conclusions on ion release.

5] Nanomaterial Cu's increased antimicrobial effectiveness as compared to conventional Cu in the contact-killing of Influenza A Virus is shown to be affected by both surface roughness and microstructure. Follow-on antimicrobial efficacy testing of as made and polished coatings is needed to further uncouple the effects of surface roughness and microstructure.



Effectiveness of Nanomaterial Copper Cold Spray Surfaces on Inactivation of Influenza A Virus

Sundberg K*, Champagne V, McNally B, Helfritsch D and Sisson R

Materials Science and Engineering, Worcester Polytechnic Institute, Worcester, MA, USA

Abstract

Bacterial and viral contamination of touch surfaces allows for transmission of pathogens leading to increased risk of infection. Previous work has demonstrated the antimicrobial properties of copper for contact-killing of microbes for use in hospitals. Less research exists on copper as an antiviral surface and on the effects of nanomaterial copper surfaces in the contact-killing of viruses. Nano agglomerate and conventional copper powder feedstock is used in the cold spray process to form copper coatings on aluminum substrates. The nano and conventional copper surfaces formed are tested for antiviral contact-killing of influenza A virus. After a two hour exposure to the surfaces, the surviving influenza A virus was assayed and the results compared. The differences in the powder feedstock used to produce the test surfaces were examined in order to explain the mechanism that caused the observed differences in influenza A virus killing efficiency. Results showed that the nano copper surface was antiviral, but less effective than a study on antimicrobial killing of MRSA on copper surfaces. The nano copper surface was more effective at percent reduction of influenza A virus than that of conventional copper. It was determined that the work hardening caused by the cold spray process in combination with the high number of grain boundaries results in a copper microstructure that enhances ionic diffusion. Copper ion diffusion is the principle mechanism for microbial and viral destruction on copper surfaces. Testing determined significant microbiologic differences between nano- and conventional Cu surfaces and demonstrates the importance of nano copper surfaces as an antiviral agent. The nano agglomerate powder shows superior antiviral effectiveness to that of conventional Cu due to an increase in grain boundaries at the nano level. Further research is needed to determine the effects of nano and conventional copper surface roughness on the contact-killing rate of viruses versus microbes on both a micro and nano-scale.

Keywords: Cold spray; Influenza A virus; Nanomaterial; Copper; Antiviral

Background

The epidemiology of nosocomial pathogens is a cause of concern in hospitals due to the possibility of increased risk of infection [1,2]. Influenza A, a viral pathogen, is one of the leading causes of infection and mortality of young children and the elderly (>65) [3]. During the 2012 and 2013 influenza seasons, the percentage of deaths attributed to pneumonia and influenza in the United States peaked at 9.9%, exceeding the epidemic threshold for 13 consecutive weeks [4].

It is indicated by the Center for Disease Control and Prevention (CDC), that the three main mechanisms of influenza virus transmission are the spread of infectious droplets through: airborne, person to person, or surface contact [5]. Research shows, influenza that is distributed by airborne nuclei can contaminate objects in the environment, leading to easy transfer at the hand-surface contact interface [6-8]. The spread of bacteria and viruses via hospital surfaces, including medical equipment, work stations, and patient rooms is well documented [2,6,9,10]. The addition of self-disinfecting surfaces in conjunction with required cleaning practices further prevents the spread of infectious diseases [11].

Research exists supporting the role of copper surfaces as an antimicrobial material [12-15]. A correlation is shown between the increase in copper content and the increased contact-killing of *E. coli*, *Listeria monocytogenes*, and Methicillin-Resistant *Staphylococcus aureus* [12]. Two hypothesized mechanisms for contact killing of microbes is the interaction of copper ions with the cellular membrane causing an influx of ions in the intracellular matrix, and copper induced DNA fragmentation, both resulting in cell death [16]. Testing of *S. aureus* and *E. coli* on nano Cu-incorporated diamond-like carbon films shows post-incubation TEM images of cytoplasm leakage from cell

membranes and data from Transmission electron microscopy- Energy dispersive X-ray spectroscopy (TEM-EDS) indicating copper ion presence in the membranes of both microbes. This shows the primary contact-killing mechanism to be membrane deformation by copper ions [17].

Research also exists supporting the role of antimicrobial copper surfaces in the contact-killing of influenza A virus [18]. It is shown that Cu(II) ions added in solution to influenza A virus result in morphological abnormalities [19]. Similar studies with copper ion solutions show the increased sensitivity of enveloped viruses to Cu(II) ions as compared to non-enveloped viruses, suggesting that the virus's lipid membrane becomes overwhelmed by intracellular copper, similar to the microbial kill mechanism [20].

The Copper Development Association (CDA) currently lists more than 450 wrought and cast copper alloys under the unified numbering system (UNS) that are registered with the U.S. Environmental Protection Agency (EPA) as antimicrobial [21]. All EPA approved surfaces contain a copper content of at least 60%. EPA-approved laboratory studies show that copper kills 99.9% of disease-causing bacteria including, *Staphylococcus aureus*, *Enterobacter aerogenes*, *Escherichia coli*

*Corresponding author: Kristin Sundberg, Materials Science and Engineering, Worcester Polytechnic Institute, Worcester, MA 01609, USA, Tel: 978-844-4511; E-mail: kristinsundberg7@yahoo.com

Received September 10, 2015; Accepted October 14, 2015; Published October 21, 2015

Citation: Sundberg K, Champagne V, McNally B, Helfritsch D, Sisson R (2015) Effectiveness of Nanomaterial Copper Cold Spray Surfaces on Inactivation of Influenza A Virus. J Biotechnol Biomater 5: 205. doi:10.4172/2155-952X.1000205

Copyright: © 2015 Sundberg K, et al. This is an open-access article distributed under the terms of the Creative Commons Attribution License, which permits unrestricted use, distribution, and reproduction in any medium, provided the original author and source are credited.

O157:H7, *Pseudomonas aeruginosa*, Vancomycin-resistant *Enterococcus faecalis* (VRE) and MRSA, within 2 hours of contact. All EPA registered materials can be used for frequently touched surfaces, such as hospitals, for control and inactivation of microbes [22]. While there are specific guidelines for testing the efficacy of antimicrobial surfaces against microbes, there are no EPA approved protocols for testing their efficacy against viruses.

Increasing the kill rate of influenza A virus is important, as the survival of infectious influenza on fomites can last up to 72 hours [6]. Research shows that processing of copper material does affect the ability of copper to inactivate microbes [23]. Copper surface coatings can be created using various metal spray techniques including plasma, arc, and cold spray processes. During the cold spray process, a heated carrier gas brings copper powder to supersonic velocities, causing them to plastically deform and adhere to a metal substrate, forming a thin solid copper coating. A schematic of the cold spray process is shown in Figure 1. Powder particles are fed into a converging-diverging nozzle filled with a stream of heated helium or nitrogen gas and then blasted at the substrate, forming a mechanical bond with the surface upon impact. In general, the cold spray process operates at a temperature between 100-500°C and at a velocity range of 600-1000 m/s, resulting in <1% porosity and <1% of oxides.

Champagne et al. [23] indicates that of the plasma, arc, and cold spray processes, the later has the higher velocity impact of copper particles, resulting in increased material hardness and higher kill rate of *Staphylococcus aureus*. The aim of this research is to increase copper material hardness through the use of nano copper cold spray particles, which will create a harder copper coating that will show a higher kill rate towards Influenza A Virus.

Test Procedure

The cold spray surface coating technique was used to produce copper coatings approximately 0.05 mm thick on aluminum substrates. The nano and conventional copper powder feedstock used for cold sprays is shown in Figures 2 and 3. The particle size distribution for the nano copper (Eltron) and conventional copper (Praxair Cu-159) is an average of 25 microns and a range of -31/+5 microns, respectively [24,25]. To confirm powder particle size as reported by the powder producer, a particle size distribution analysis was performed on the Horiba LA-910 Laser Scattering Particle Size Distribution Analyzer, in a 10 g/L solution of Sodium Hexametaphosphate in DI Water. The nano and conventional powder are both pure copper. The conventional powder is produced by gas atomization. For the nano powder, nanosized particles were dispersed in a solvent with a pure copper binder precursor and spray dried under controlled atmosphere to form perfectly spheroidized micron sized particles (~ 20 um in diameter) by Eltron Research and

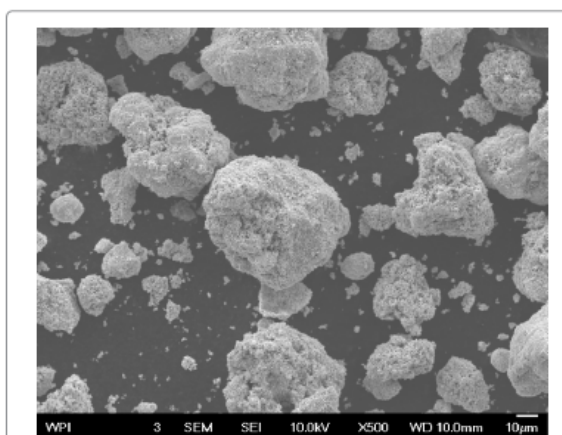
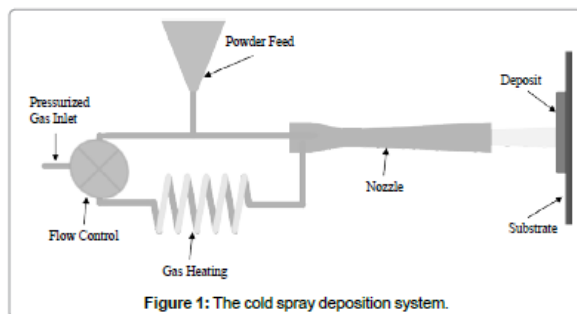


Figure 2 : Feedstock copper nano powder.

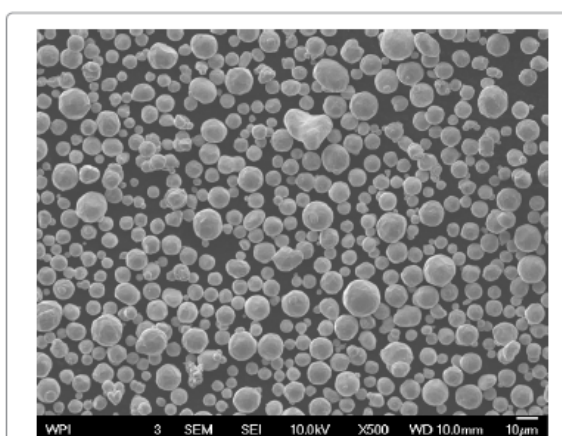


Figure 3 : Feedstock copper conventional powder.

Development Inc. [24,26] Copper nanoparticles offer many benefits over convention copper powders in terms of strength, hardness, wear and reactivity but cannot be used in the cold spray process due to insufficient mass. During the cold spray process, particles less than 5 microns in diameter can have insufficient momentum to penetrate the “bow shock” region next to the substrate [27]. Eltron utilizes spray drying to achieve strong, nanoparticle agglomerates with tight control of particle shape, size, distribution, and porosity with an ultra-fine grained (UFG) inorganic metallic binder that can match the nanoparticles in composition and that have sufficient mass and momentum to be used as a feedstock for the cold spray process [26]. Cross sections of the nano and conventional copper coupons produced are shown in Figures 4 and 5. Both deposits formed dense coatings with low porosity. Unlike the conventional Cu coating, the nano-structured deposit has areas of nano-Cu agglomerates surrounded by conventional Cu, which serves as a binder, as indicated by the darker colored regions of Figure 4. The clear difference in microstructure suggests a change in biological activity from conventional to nano copper surfaces.

The copper coated coupons were inoculated with influenza A virus, held at room temperature for two hours, and then survivors were



Figure 4 : Cross sectional view of the cold sprayed copper nano powder deposit.



Figure 5 : Cross sectional view of the cold sprayed copper conventional powder deposit.

resuspended and cultured. There are no EPA approved test procedures for copper alloy surfaces as a sanitizer of viruses.

The EPA antimicrobial procedure, "Test Method for Efficacy of Copper Alloy Surfaces as a Sanitizer", was used with some changes [27]. The full details of the modified procedure are given below.

Carrier surfaces and preparation

Carrier surfaces and preparation: The surfaces of the nano and conventional copper coupons were the test carriers. The surfaces of the stainless steel squares were the control carriers. The carriers were sterilized with ethanol and allowed to dry prior to use in the test. Post sterilization, carriers were placed into Petri dishes.

Inoculation of carriers: A 100 μ L aliquot of influenza A virus, ATCC VR-544, strain Hong Kong was inoculated into the test and control carriers. The inoculum was spread within 1/8 inch of the carrier edge. The virus was then air-dried at room temperature (20°C) in a relative humidity of 23.5% until visibly dry (30 minutes). This temperature and humidity was selected to maximize virus survival while drying. Exposure time began at the 30 minute drying mark.

Neutralization of subculture: Following the two hour exposure time, a 1.00 μ L aliquot of neutralizing test medium was inoculated onto the carriers and the carriers were scraped with a sterile cell scraper. The

test medium is comprised of minimum essential medium (MEM) and 100 μ g/mL penicillin, 10 μ g/mL gentamicin, 2.5 μ g/mL amphotericin B, 2 μ g/mL TPCK-Trypsin, 0.2% bovine serum albumin (BSA), and 25 mM HEPES. Post scraping, 10-fold serial dilutions were performed in the test medium. An 100 μ L aliquot from each dilution was inoculated into the indicator cell cultures in quadruplicate. Indicator cell cultures were MDCK (canine kidney) cells.

Incubation and observation: The cell cultures were incubated at 36-38°C in 5-7% CO₂ for seven days. Following incubation, for each test the average TCID₅₀ was calculated. The average log and percent reduction in viral titer of each test substance were calculated using the corresponding average TCID₅₀ of the control carriers (stainless steel).

Results and Discussion

The ability to increase the contact-killing rate of influenza A virus on copper coatings is suggested to relate to the increase in Cu ion diffusion through the virus's lipid membrane [20]. Champagne et al. shows that diffusion of copper ions from conventional copper surfaces is increased by copper surface hardness, resulting in increased microbial destruction [23]. Surface hardness of copper coatings can be increased further by using nano copper powder as opposed to the conventional powder typically used, as detailed in the below research results.

The percent reduction of influenza A virus after two hours on the surface of nano and conventional copper cold spray surfaces is shown in Figure 6. Also included in Figure 6 is data provided by the Army Research Laboratories on testing of copper cold spray surfaces for percent reduction of MRSA [28]. The results show that nano copper and conventional copper have a 99.3% and 97.7% reduction in influenza A virus, respectively. The use of copper as an antimicrobial material shows >99.9% reduction of MRSA after 2 hours. Copper is antiviral, but less effective at contact-killing of viruses than microbes.

The contact-killing of viruses by nano copper surfaces is more efficient than that of conventional copper. This difference in antiviral effectiveness between nano and conventional copper requires an examination of how the powder feedstock for the cold spray deposition process affects the nature of a copper coating.

The cold spray process operates at temperatures between 100-500°C and velocities between 600-1000 m/s. Due to the unique cold spray process conditions, two specific properties can be attributed to the copper cold spray coating. The first, high velocity impact of the powder particles creates a low porosity coating. Generally, cold spray coatings result in <1% porosity and <1% of oxides. Second, by blasting the powder particles at a high velocity and relatively low temperature, work hardening is induced. Work hardening results in high material

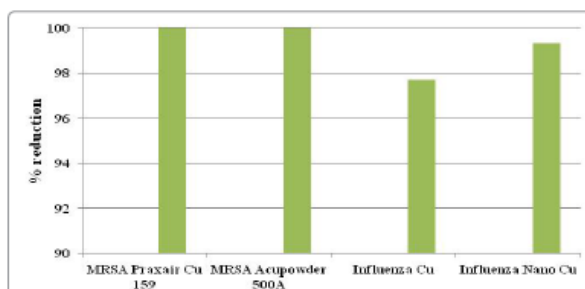


Figure 6: Percent reduction of MRSA (data taken from experiments [28]. and influenza A virus after 2 hour exposure to various copper deposits.

dislocation density cause by the plastic deformation of particles' as they hit the substrate and neighboring particles. Champagne et al. has shown that work hardening by cold spray increases dislocation density within copper [29]. By increasing the number of particles that collide with each other, the work hardening increases. This in turn will increase dislocation density and ultimately material hardness.

Particle size distribution analysis shows that the average particle size for nano and conventional copper powder was 37.8 microns and 10.4 microns, respectively. While the cold spray nano powder feedstock is larger, it contains many nano sized particles on the scale of 60-80 nm (Sky Spring Nanomaterials) [26]. Post agglomeration, the micron sized nano powder is heat treated using a proprietary process developed by Eltron to form micron sized particles with a nano grained structure [26]. The increase in nano grained boundaries in the nano powder cold spray feedstock allows for increased dislocation density post-processing. The relationship between dislocation density and diffusivity is $D_p \propto \rho$ [30]. The diffusion of copper ions is increased with the hardness increase produced by nano grain boundaries, which enhances copper ion flow for viral destruction.

As illustrated in Figure 7, nano hardness testing was completed, with the resulting values for the nano copper and conventional copper surfaces as 2.44 and 1.45, respectively. The relationship between hardness and dislocation density is $H_2 \propto \rho$ [31]. It follows that the nano copper surface has higher nano hardness, meaning a higher dislocation density from work hardening. Due to the reduced size of nano copper powder in comparison to the conventional powder, there are a greater number of particles present in the nano copper powder when sprayed. This means that there are a greater number of grain boundaries too. The more grain boundaries present upon impact with the substrate, the greater the work hardening resulting in higher dislocation density.

Dislocations at grain boundaries of metals increase ion diffusion, also known as pipe diffusion [32]. The increase in dislocation on the nano copper coating led to higher ion diffusivity reflected in a greater reduction in influenza A virus than conventional copper surfaces.

Conclusion

The effectiveness of copper as antimicrobial for contact-killing on touch surfaces has been well documented [12-15]. Less research exists on the effectiveness of copper as an antiviral agent and on the effects



Figure 7: Nano hardness indents on the cross sectional of a cold sprayed nano powder deposit.



Figure 8: Copper cold sprayed hospital table.

of nano grained copper surfaces on contact-killing rate of viruses. The significant differences between nano and conventional copper surfaces produced by cold spray technique, as shown here, demonstrate the importance of the copper powder processing and of the resulting deposition structure. The nano copper surface showed antiviral effectiveness caused by high dislocation density imparted to the sprayed particles by a combination of cold spray velocity and pre-processing heat treatment of nano particle agglomerates. The high dislocation density, measured by an increase in material hardness, allowed for higher copper ion diffusivity.

Cold spray technology is currently in use to produce metal copper coatings for hospital applications. Touch surfaces such as the copper coated hospital tray in Figure 8; show the current use of copper as an antimicrobial surface. Data collected on virus contact-killing properties of copper supports the potential future use of copper in hospitals and other industries for antiviral applications.

Both the nano and conventional copper for influenza A virus reduction have lower % reduction values than that of the copper surfaces used for contact-killing of MRSA. Surface roughness is documented to effect microbe retention [33]. Roughness of the copper surface could be a contributing factor to the higher contact-killing levels of influenza A virus by nano copper. Microbes, like MRSA, range in size from 0.5-1.0 μm in diameter, whereas viruses like influenza A, are on a 80-120 nm scale [34,35]. The size difference may affect the ability of microbes and viruses to form reservoirs of survivors in microscopic pockets and crevices on copper surfaces. Further analysis of surface metrology on a micron and nano scale is needed to determine the effect of conventional and nano copper surface structures on the contact-killing of influenza A virus.

Acknowledgement

The sanitizer testing conducted against influenza A virus and reported in this paper was carried out under contract by ATS Labs at Eagan MN. The experiments were performed by Shanen Conway.

References

1. Page K, Wilson M, Parkin I (2009) Antimicrobial surfaces and their potential in reducing the role of the inanimate environment in the incidence of hospital-acquired infections. *J Mater Chem* 19: 3819-3831.
2. Hota B (2004) Contamination, Disinfection, and Cross-Colonization: Are Hospital Surfaces Reservoirs for Nosocomial Infection? *Clinical Infectious Diseases* 39:1182-1189.

3. Monto AS, Ansaldi F, Aspinall R, McElhanev JE, Montañó LF, et al. (2009) Influenza control in the 21st century: Optimizing protection of older adults. *Vaccine* 27: 5043-5053.
4. Centers for Disease Control and Prevention (CDC) (2013) Influenza activity-United States, 2012-13 season and composition of the 2013-14 influenza vaccine. *MMWR Morb Mortal Wkly Rep* 62: 473-479.
5. CDC (2005) Infection control measures for preventing and controlling influenza transmission in long-term care facilities.
6. Boone SA, Gerba CP (2007) Significance of fomites in the spread of respiratory and enteric viral disease. *Appl Environ Microbiol* 73: 1687-1696.
7. Goldmann DA (2000) Transmission of viral respiratory infections in the home. *Pediatr Infect Dis J* 19: S97-102.
8. Weber TP, Stilianakis NI (2008) Inactivation of influenza A viruses in the environment and modes of transmission: A critical review. *J Infect* 57: 361-373.
9. Neely AN, Maley MP (2000) Survival of enterococci and staphylococci on hospital fabrics and plastic. *J Clin Microbiol* 38: 724-726.
10. Bergen LK, Meyer M, Høg M, Rubenhagen B, Andersen LP (2009) Spread of bacteria on surfaces when cleaning with microfibre cloths. *J Hosp Infect* 71: 132-137.
11. Tamimi AH, Carlino S, Gerba CP (2014) Long-term efficacy of a self-disinfecting coating in an intensive care unit. *Am J Infect Control* 42: 1178-1181.
12. Michels H, Wilks S, Noyce J, Keevil C (2005) Copper Alloys for Human Infectious Disease Control. Proceedings of the Materials Science and Technology Conference, Pittsburgh, PA Copper for the 21st Century Symposium.
13. Copper Development Association (2007) Copper Clinical Trial: Investigating the antimicrobial properties of copper alloys in healthcare facilities.
14. Noyce J, Michels H, Keevil C (2006) Potential use of copper surfaces to reduce survival of epidemic methicillin-resistant *Staphylococcus aureus* in the healthcare environment. *Journal of Hospital Infection* 63: 289-297.
15. Weaver L, Michels HT, Keevil CW (2008) Survival of *Clostridium difficile* on copper and steel: Futuristic options for hospital hygiene. *J Hosp Infect* 68: 145-151.
16. Grass G, Rensing C, Solioz M (2011) Metallic copper as an antimicrobial surface. *Appl Environ Microbiol* 77: 1541-1547.
17. Lee F, Wang D, Chen L, Kung C, Wu Y, et al. (2013) Antibacterial nanostructured composite films for biomedical applications: microstructural characteristics, biocompatibility, and antibacterial mechanisms. *Biofouling* 29: 295-305.
18. Noyce JO, Michels H, Keevil CW (2007) Inactivation of influenza A virus on copper versus stainless steel surfaces. *Appl Environ Microbiol* 73: 2748-2750.
19. Horie M, Ogawa H, Yoshida Y, Yamada K, Hara A, et al. (2008) Inactivation and morphological changes of avian influenza virus by copper ions. *Arch Virol* 153: 1467-1472.
20. Sagripanti JL, Routson LB, Lytle CD (1993) Virus inactivation by copper or iron ions alone and in the presence of peroxide. *Appl Environ Microbiol* 59: 4374-4376.
21. Copper Development Association (2015) Properties of Wrought and Cast Copper Alloys.
22. Copper Development Association. The Copper Advantage: A Guide to Working with Copper and Copper Alloys.
23. Champagne VK, Helfrich DJ (2013) A demonstration of the antimicrobial effectiveness of various copper surfaces. *J Biol Eng* 7: 8.
24. Praxair: Surface technologies. Powder Solutions, product brochure.
25. Test method for efficacy of copper alloy surfaces as a sanitizer.
26. Rolfe S (2014) email conversation and Phase I SBIR Final Report, "Advanced Nanostructured Powders for Cold Spray Applications", Eltron Research and Development Inc., 4600 Nautilus Court South Boulder, CO 80301-3241.
27. Liu J (2006) Cold spray formation of thin metal coatings. US Patent Application US 2006/0090593.
28. Eltron: Research and development. Copper Nanograined Agglomerates.
29. Helfrich D (2014) Email conversation.
30. Mittemeijer E (2010) Fundamentals of Materials Science. Springer, Verlag, Berlin, Heidelberg.
31. Mehrer H (2007) Diffusion in solids: Fundamentals, methods, materials, diffusion-controlled processes. Springer, Berlin, Heidelberg, New York.
32. Champagne V, Helfrich D, Trexler M (2007) Some Material Characteristics of Cold-Sprayed Structures. *Res Lett Mater Sci*.
33. Center for Disease Control Prevention. Electron Micrograph of Methicillin-Resistant *Staphylococcus aureus* (MRSA).
34. Hart E (1957) On the role of dislocations in bulk diffusion. *Acta Metall* 5: 597.
35. Rapid reference to influenza. The influenza virus: structure and replication. Elsevier Ltd.

Supplemental Paper B: Anti-bacterial and anti-viral performance of kinetically deposited copper surfaces

Anti-bacterial and anti-viral performance of kinetically deposited copper surfaces

Victor Champagne¹, Kristin Sundberg² and Dennis Helfritsch³

1. Army Research Laboratory, Aberdeen Proving Ground, MD
2. Worcester Polytechnic Institute, Worcester, MA
3. Service Engineering, Aberdeen, MD Dennis.j.helfritsch.ctr@mail.mil

Abstract

Bacterial and viral contamination on touch surfaces results in increased risk of infection. In the last few decades, work has been done on the antimicrobial properties of copper and its alloys against a range of micro-organisms threatening public health in food processing, healthcare and air conditioning applications; however, the optimum microstructural characteristic of the copper surface is not well defined.

The disinfection effectiveness of three copper surfaces and two copper feedstocks are examined. The surfaces are inoculated with methicillin-resistant *Staphylococcus aureus* (MRSA) and influenza A virus. After a two hour exposure to the surfaces, the surviving micro-organisms were assayed and the results compared.

These tests show significant anti-microbial differences between coatings produced by different spray techniques and by different feedstock powders, and the importance of the copper application technique is demonstrated.

Keywords: antimicrobial, surface, copper, powder, spray

Introduction

Microbial growth on surfaces is a cause of concern in many hospitals and food processing industries due to the possibility of increased risk of infection [1]. The bacterial contamination of hospital surfaces, including patient rooms, nurse stations and kitchens has been extensively documented [2,3,4,5]. Research shows that influenza, distributed by airborne nuclei, can contaminate objects in the environment, leading to easy transfer at the hand-surface contact interface [6,7,8]. The addition of self-disinfecting surfaces in conjunction with required cleaning practices would further prevent the spread of infectious disease.

The use of copper and copper alloys for frequently touched surfaces such as door and furniture hardware, bed rails, light switches and food preparation surfaces can help limit microbial infections in hospitals and food dispensing organizations. Laboratory studies conducted under EPA-approved protocols have proven copper's ability to kill, within 2 hours of contact time, more than 99.9% of the following disease-causing bacteria: *Staphylococcus aureus*, *Enterobacter aerogenes*, *Escherichia coli* O157:H7, *Pseudomonas aeruginosa*, Vancomycin-resistant *Enterococcus faecalis* (VRE) and MRSA. Michels, et al. [9] show that increasing the copper content of alloys increases antimicrobial effectiveness. The contact killing is so rapid that the production of protective biofilms is not possible [10].

The hypothesized mechanisms for contact killing of microbes is the interaction of copper ions with the cellular membrane causing an influx of ions in the intracellular matrix [11]. Testing of *S. aureus* and *E. coli* on nano Cu-incorporated diamond-like carbon films shows post-incubation TEM images of cytoplasm leakage from cell membranes and data from TEM-EDS indicating copper ion presence in the membranes of both microbes. This shows the primary contact-killing mechanism to be membrane deformation by copper ions [12].

Viruses, as well as bacteria, have been shown to be killed by contact with copper. The Center for Disease Control and Prevention denotes the influenza transmission mechanisms as the spread of infectious droplets through airborne, person to person, or surface contact [13]. Influenza A, a viral pathogen, is one of the leading causes of infection and mortality of young children and the elderly (>65) [14]. During the 2012 and 2013 influenza seasons, the percentage of deaths attributed to pneumonia and influenza in the United States peaked at 9.9%, exceeding the epidemic threshold for 13 consecutive weeks [15].

The Copper Development Association currently lists more than 450 wrought and cast copper alloys that are registered with the U.S. EPA as antimicrobial [16]. All EPA approved surfaces contain a copper content of at least 60%. All EPA registered materials can be used for frequently touched surfaces, such as hospitals, for control and inactivation of microbes. [17] While there are specific guidelines for testing the efficacy of antimicrobial surfaces against bacteria, there are no EPA approved protocols for testing their efficacy against viruses.

Methods

In order to make use of the antimicrobial ability of copper, surfaces that contact skin and foods should be composed of copper or copper alloy. This can be accomplished with solid copper equipment or by means of copper surface coating. In general, cost considerations favor copper coatings over solid structural copper. Various metal spray techniques are available for the purpose of depositing a copper surface onto implements that can transmit microorganisms, and it is desired to identify an optimal deposition method. Three metal spray techniques were evaluated with respect to the anti-microbial activity of the copper surfaces produced by each. The commercial metal spray techniques evaluated were cold spray (high speed, kinetically deposited solid state powder particles), plasma spray and wire arc spray (moderate speed, kinetically deposited molten particles), and each produces significantly different microstructures.

The cold spray process shoots copper powder at supersonic velocities onto a metal substrate, forming a thin, solid copper coating. The high velocity impact of the powder particles creates a low porosity coating high in grain dislocations and work hardening. Plasma and wire arc sprays deposit slower, molten particles. The particle impact regimes of the three methods are shown in Figure 1.

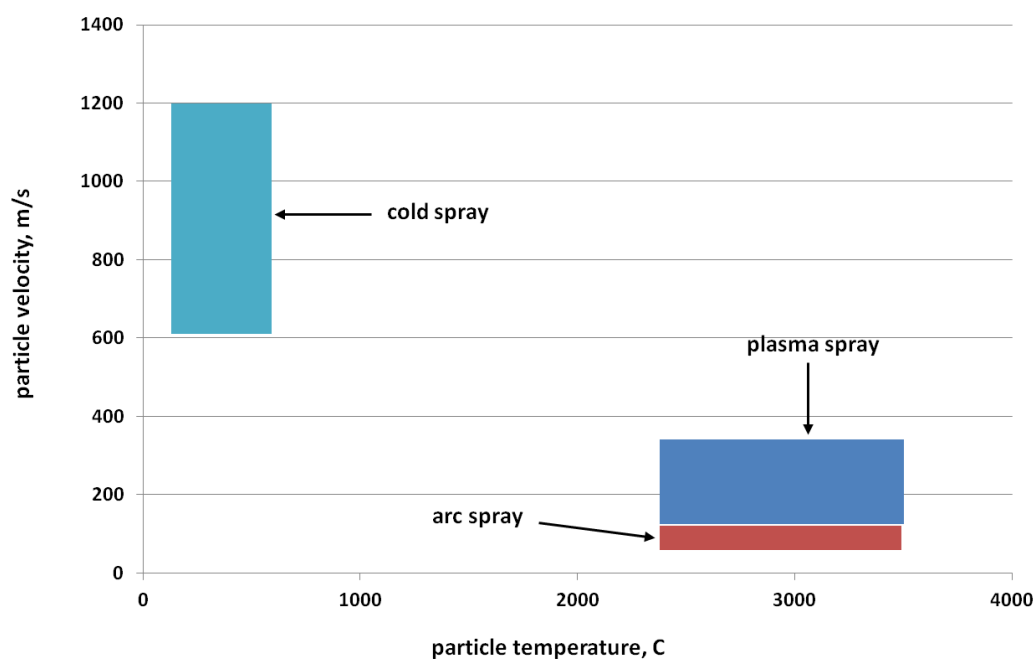


Figure 1. Particle impact conditions for different spray technologies.

Anti-viral effectiveness were compared for cold sprayed conventional copper powder feedstock and nanometer particle diameter feedstock powder. The nano copper powder is composed of micron sized agglomerates of nano-scale particles.

The copper powder used for the antibacterial tests was Praxair Cu-159 with cold spray. The plasma arc and wire arc sprays use C110 and copper wire, respectively, as feedstock. The conventional (Praxair Cu-159) and nano (Eltron Research and Development Inc.) copper powder feedstocks used for cold sprays are shown in Figures 2.

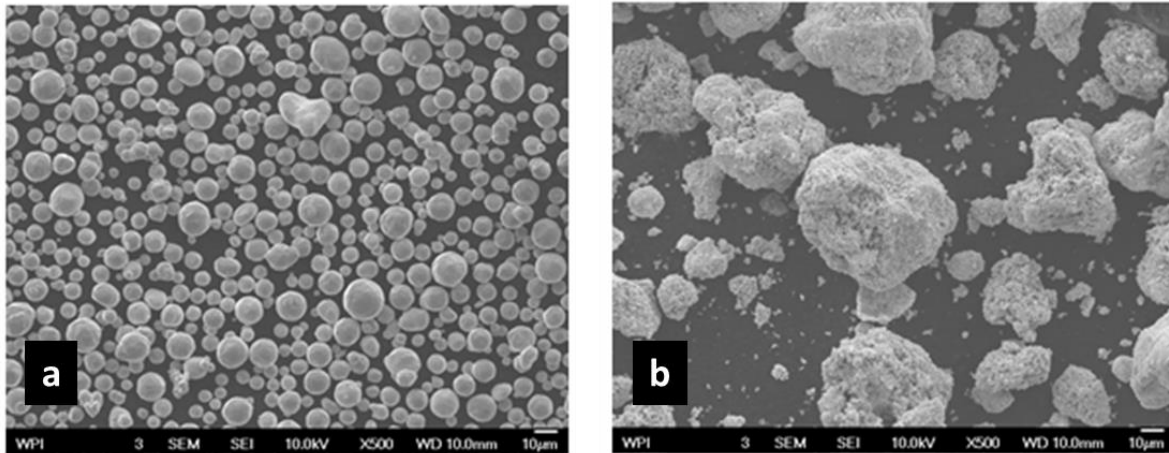


Figure 2. Conventional (a) and nano-scale (b) copper powders.

Approximately 0.1 mm thick coatings were applied to stainless steel substrates. The coatings completely covered the metal substrates with an impervious seal. Cross sections of the coupons produced by the three spray techniques for antibacterial tests are shown in Figures 3. The differences in microstructures can be expected based on the large differences experienced by impacting particles for the three methods. These differences in microstructure suggest that differences in biological activity may also occur. Evidence of particle melting is clear for the high-temperature plasma and wire arc processes. The incidence of large voids is seen in the wire arc process cross section.

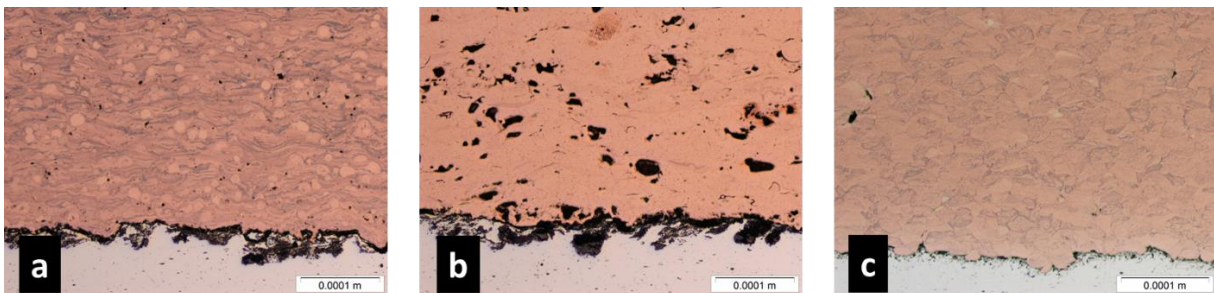


Figure 3. Deposited copper cross sections. Plasma (a), Arc (b), Cold (c) Sprays. Stainless steel substrates can be seen at the bottom.

Cross sections of the coupons produced by cold spray for antiviral tests are shown in Figures 4. Both deposits formed dense coatings with low porosity. Unlike the conventional Cu coating, the nano-structured deposit has areas of nano-Cu agglomerates surrounded by conventional Cu, which serves as a binder, as indicated by the darker colored regions of Figure 4. The clear difference in microstructure suggests a change in biological activity from conventional to nano copper surfaces.

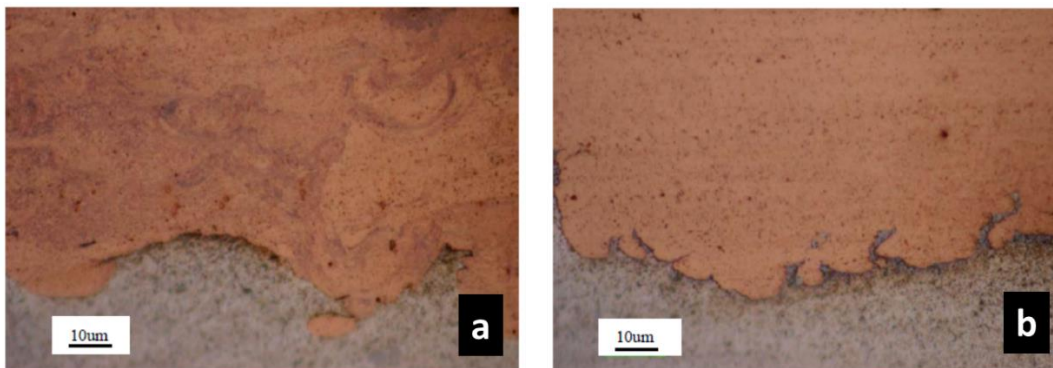


Figure 4. Cross sectional views of the nano-scale powder (a) and the conventional powder (b) cold sprayed deposits.

The copper coated coupons produced by the three thermal spray devices were inoculated with MRSA. The copper coated coupons produced by cold spray for the conventional and nano-scale feedstock powders were inoculated with influenza A virus. Stainless steel coupons were used as control substrates for both the bacterial and viral tests. The inoculated samples were then held at room temperature for two hours, after which survivors were re-suspended and cultured. This procedure followed the EPA Protocol [18] “Test Method for Efficacy of Copper Alloy Surfaces as a Sanitizer”. There are no EPA approved test procedures for copper alloy surfaces as a sanitizer of viruses, and the EPA antimicrobial procedure was used with some changes for the influenza A tests. The reduction of inoculated microbes was normalized by the results of the control exposure to a stainless steel surface for the bacterial test results. The bacterial measurements were taken after a two hour continuous exposure to the surfaces. The viral measurements were taken after several intermediate exposures up to 2 hours. The full details of the procedures are given in references 19 and 20.

Results

The results in terms of the percent of surviving *S. aureus* after two hours are shown in Figure 5. The result for cold spray was below minimal measurement thresholds and is thus reported as “less than”. The results show a greater than three order of magnitude difference in kill efficiency between the plasma and wire arc methods and the cold spray method of copper deposition.

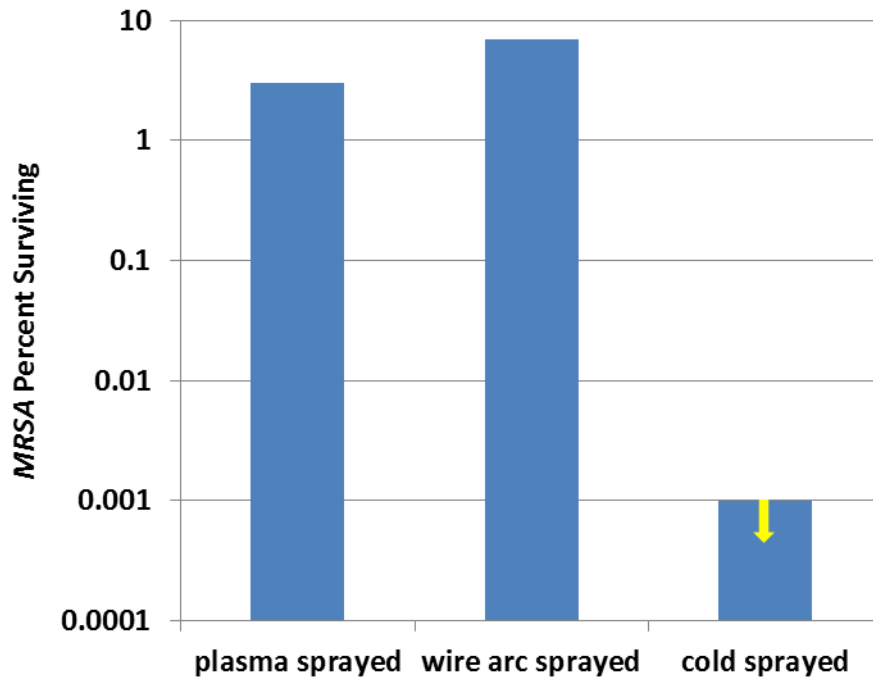


Figure 5. Percent MRSA surviving after a two hour exposure to copper surfaces.

The results for viral killing is shown in Figure 6. The result for the conventional copper cold sprayed surface was very similar to the nano-copper cold sprayed surface, so it is not shown. The results obtained for inactivation of Influenza A on wrought copper (C1100) [21] have been added to the graph for comparison. The difference in procedure between this current work and that of Noyce, et al, are that this work utilized the TCID₅₀ Assay Protocol, while Noyce, et al uses a fluorescent dye that illuminates viral particles that are still infectious and counts virus particles recovered from the coupons under a microscope. In addition, measurements were taken after 10, 30, 45, 60, 90 and 120 minute exposures for the current work, while measurements were made after 60 and 360 minutes exposure for wrought copper. In both cases, the percent survivors on stainless steel controls were orders of magnitude higher than on the copper surfaces. For clarity, the end points of the cold-sprayed, nano-Cu data and the wrought copper are 0.13% and 0.03% respectively.

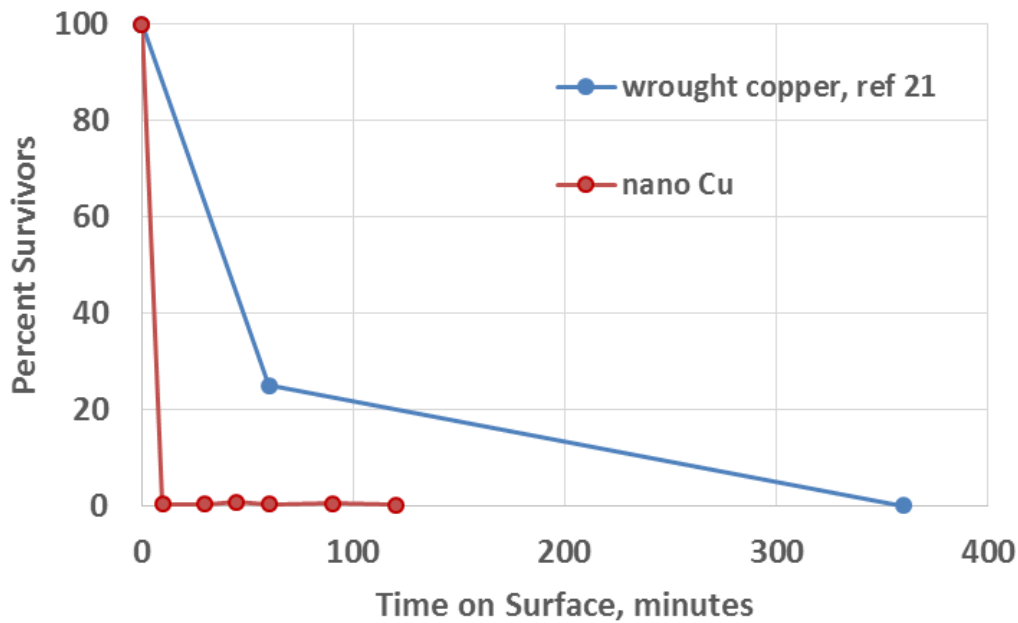


Figure 6. Percent Influenza A surviving as a function of exposure time to copper surfaces.

Discussion

The differences in anti-microbial and anti-viral effectiveness between copper deposition methods and feedstocks requires an examination of how the powder feedstock and deposition process affects the nature of the copper surface. In order to do this we need to know the mechanism by which contact-killing occurs.

Recent studies show that large amounts of copper ions, Cu(II), were taken up by *E. coli* over 90 min, when cells were applied to copper coupons via an aqueous suspension (a standing drop). When cells were plated on copper using minimum liquid and a drying time of 5 seconds, the accumulation of copper ions by cells was even more dramatic, reaching a high concentration in a fraction of the time. The copper ion level of cells remained high throughout the killing phase, suggesting that cells become overwhelmed by their intracellular copper [22].

Research shows that copper ions added in solution to influenza A virus results in morphological abnormalities [23]. Similar studies with copper ion solutions show the increased sensitivity of enveloped viruses to copper ions as compared to non-enveloped viruses, suggesting that the virus's lipid membrane becomes overwhelmed by intracellular copper, similar to the microbial kill mechanism [24].

Thus the presence of ionic copper is the likely bacterial and viral kill mechanism. Copper layers that maximize ionic copper diffusion to the surface are therefore the best antimicrobials. Ion diffusion in metals is augmented by the presence of grain dislocations. Known as "pipe diffusion", significant ionic diffusion occurs through these dislocations. The relationship between dislocation density and ionic diffusivity is given by [25]

$$D_{\text{eff}} = D_0 \left[1 + \pi a^2 \rho_d \left(\frac{D_d}{D_0} - 1 \right) \right]$$

Where

D_{eff} is the effective ionic diffusivity

D_0 is the lattice diffusivity

D_d is the pipe diffusivity

ρ_d is the dislocation density

a is the average dislocation radius

In addition to dislocations, increased grain boundaries caused by impact breakup serve a similar augmentation of diffusion. The generation of ultra-fine-grained structures, including dislocations, dislocation cells and twinning, caused by the high velocity impact of cold spray particles has been extensively documented [26, 27]. Figure 7 shows the extreme plastic deformation of a copper particle after impact by cold spray [28]. A jet of plasticized material is typically ejected at the particle/substrate interface. Figure 8 shows a TEM micrograph of an inter-particle triple point in a cold sprayed copper coating showing typical microstructural features [29]. Particle-particle boundaries are marked with arrows. Identified areas are: (A) high dislocation density with dislocations arranged in walls, grain size above 1 μm ; (B) aligned elongated grains, featuring grain boundaries characterized by ultrahigh dislocation densities adjacent to the grain boundaries; (C) ultrafine grains about 100 nm in diameter exhibiting heavily deformed zones around the grain boundaries with extremely high dislocation densities; (D) Dislocation-free region, grain size above 1 μm .

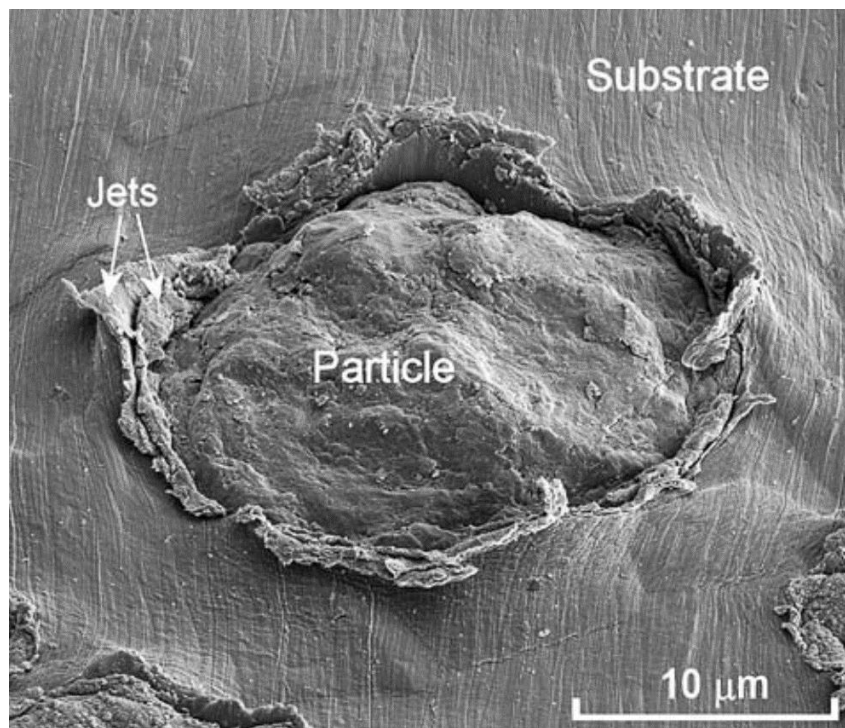


Figure 7. Example of cold sprayed copper particle impact.

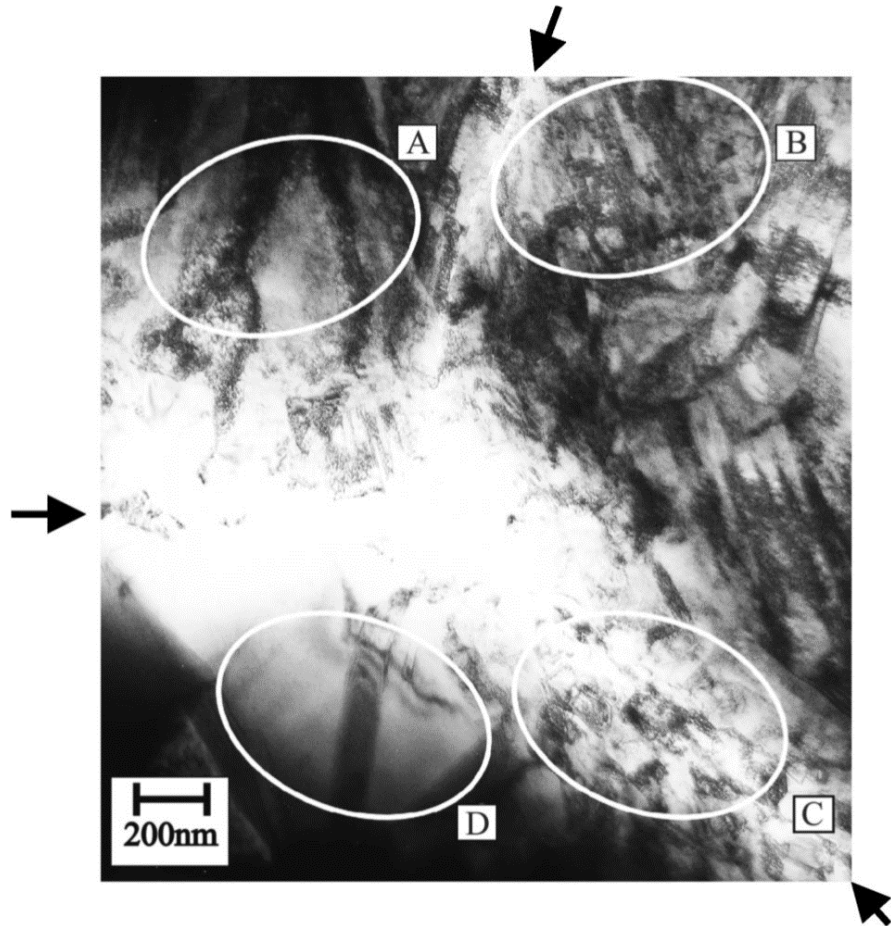


Figure 8. Ultra fine grained structure of an impacted copper particle.

Clearly, bacterial inactivation by cold-sprayed copper surfaces was much more complete than viral inactivation. Hardier viral defenses may be one explanation. Roughness of the copper surface could be a contributing factor to the higher contact-killing levels of influenza A virus by cold-sprayed nano-copper as opposed to wrought copper. Bacteria, like MRSA, range in size from 0.5-1.0 μ m in diameter, whereas viruses like influenza A, are on a 80-120 nm scale [30, 31]. The size difference may affect the ability of bacteria and viruses to form reservoirs of survivors in microscopic pockets and crevices on copper surfaces.

Conclusions

The effectiveness of copper and copper alloys as anti-microbial coatings on touch-surfaces has been well documented by many researchers as previously cited. Except for the copper content of alloys, the effects of the metallurgical properties of the copper coatings have not been investigated by these efforts. The significant antimicrobiologic differences between coatings originating as powders or wrought material and the differences between powder application techniques demonstrate the importance of the resulting deposition structure. The cold spray technique showed superior anti-microbial effectiveness caused by the high impact velocity imparted to the sprayed particles which results in high dislocation density and high ionic copper diffusivity.

The cold spray process is a mature technology which is currently in use for a variety of applications requiring metal coatings. The cold spray process can readily apply copper coatings onto touch surfaces. Figure 9 is an example of copper coating by cold spray. The hospital tray and the entire metal support structure of the hospital table have been coated with cold-sprayed pure copper. In addition to providing highly efficient antimicrobial surfaces, the cold spray technique will not damage heat sensitive substrates.



Figure 9. Hospital table coated with cold sprayed copper.

Acknowledgement

The sanitizer testing conducted against MRSA and influenza A virus and reported in this paper was carried out under contract by ATS Labs at Eagan MN. The experiments were performed by Amy Jeske and Shanen Conway

References

1. Page, K.; Wilson, M.; Parkin, I. Antimicrobial surfaces and their potential in reducing the role of the inanimate environment in the incidence of hospital-acquired infections. *J Mater Chem.* 2009, 19, pp 3819–3831.
2. Aycicek, H.; Oguz U.; Karci K. Comparison of results of ATP bioluminescence and traditional hygiene swabbing methods for the determination of surface cleanliness at a hospital kitchen. *Int. J. of Hygiene and Environmental Health* 2006, 209, pp 203–206.
3. Bernard, L.; Kereveur, A.; Durand, D.; Gonot, J.; Goldstein, F.; Mainardi, J.; Acar, J.; Carlet, J. Bacterial Contamination of Hospital Physicians' Stethoscopes. *Infection Control and Hospital Epidemiology* 1999, 20, pp 626–628.
4. Rutala, W.; Katz, E.; Sherertz, R.; Sarubbi, F. Environmental-Study of a Methicillin-Resistant Staphylococcus -Aureus Epidemic in a Burn Unit. *J of Clinical Microbiology* 1983, 18, pp 683–688.

5. White, L.; Dancer, S.; Robertson, C. A microbiological evaluation of hospital cleaning methods. *Int. J. of Environmental Health Research* 2007, 17, pp. 285–295.
6. Boone, S.; Gerba, C. Significance of Fomites in the Spread of Respiratory and Enteric Viral Disease. *Applied and Environmental Microbiology* 2007, 73, pp. 1687–1696.
7. Goldmann, D. Transmission of viral respiratory infections in the home. *J. Pediatr. Infect. Dis.* 2000, 19, pp. S97–S102.
8. Weber, T.; Stilianakis, N. Inactivation of influenza A viruses in the environment and modes of transmission: A critical review. *Journal of Infection* 2008, 57, pp. 361-373.
9. Michels, H.; Wilks, S.; Noyce, J.; Keevil, C. Copper Alloys for Human Infectious Disease Control. Proceedings of the Materials Science and Technology Conference, 2005 Pittsburgh, PA.
10. Nie, Y.; Kalapos, C.; Nie, X.; Murphy, M.; Hussein, R.; Zhang, J. Superhydrophilicity and antibacterial property of a Cu-dotted oxide coating surface. *Annals of Clinical Microbiology and Antimicrobials* 2010, 9, p. 25.
11. Grass, G.; Rensing, C.; Solioz, M. Metallic Copper as an Antimicrobial Surface. *Applied and Environmental Microbiology* 2011, 77, pp. 1141-1547.
12. Lee, F.; Wang, D.; Chen, L.; Kung, C.; Wu, Y. Antibacterial nanostructured composite films for biomedical applications: microstructural characteristics, biocompatibility, and antibacterial mechanisms. *Biofouling* 2013, 29, pp. 295–305.
13. CDC. Infection control measures for preventing and controlling influenza transmission in long-term care facilities. 2005, https://phpa.health.maryland.gov/OIDEOR/IMMUN/Shared%20Documents/LTCF_FluPrevention_Dec-2005.pdf
14. Monto, A.; Ansaldi, F.; Aspinall, R.; McElhaney, J.; Montano, L. Influenza control in the 21st century: Optimizing protection of older adults. *Vaccine* 2009, 27, pp. 5043–5053.
15. CDC. Influenza Activity — United States, 2012–13 Season and Composition of the 2013–14 Influenza Vaccine. *Morb. Mortal. Wkly.* 2006, 62, pp. 473-479.
16. Copper Development Association. Properties of Wrought and Cast Copper Alloys. 2017, <http://www.copper.org/resources/properties/db/basic-search.php>.
17. Copper Development Association. THE COPPER ADVANTAGE: A Guide to Working With Copper and Copper Alloys. 2010, https://www.copper.org/publications/pub_list/pdf/a1360.pdf
18. Test method for efficacy of copper alloy surfaces as a sanitizer. 2, http://www.antimicrobialcopper.org/sites/default/files/upload/media-library/files/pdfs/us/epa_sanitizer_test_method_copper_alloy_surfaces.pdf.
19. Champagne, V.; Helfritsch, D. A demonstration of the antimicrobial effectiveness of various copper surfaces, *Journal of Biological Engineering* 2013, 7:8 <https://doi.org/10.1186/1754-1611-7-8>.
20. Sundberg, K.; Champagne, V.; McNally, B.; Helfritsch, D.; and Sisson, R. Effectiveness of Nanomaterial Copper Cold Spray Surfaces on Inactivation of Influenza A Virus, *J Biotechnol Biomater* 2015, 5:4 <http://dx.doi.org/10.4172/2155-952X.1000205>.
21. Noyce, J.; Michels, H, and Keevill, C. Inactivation of Influenza A Virus on Copper versus Stainless Steel Surfaces, *Applied and Environmental Microbiology*, Vol. 73, No. 8 Apr. 2007, p. 2748–2750
22. Santo, C.; Lam, E.; Elowsky, C.; Quaranta, D.; Domaille, D.; Chang, C.; Grass, G. Bacterial killing by dry metallic copper surfaces. *Appl. Environ. Microbiol.* 2011, 77, pp. 794–802.
23. Horie, M.; Ogawa, H.; Yoshida, Y.; Yamada, K.; Hara, A. Inactivation and morphological changes of avian influenza virus by copper ions. *Arch Virol* 2008, 153, pp.1467–1472.

24. Sagripanti, J.; Routson, L.; Lytle, C. Virus Inactivation by Copper or Iron Ions Alone and in the Presence of Peroxide. *Applied and Environmental Microbiology* 1993, *59*, pp. 4374-4376.
25. H. Mehrer, *Diffusion in Solids*, Springer Series in Solid-State Sciences, 155, 2007, pp 583-591.
26. Zhang, Y.; Brodusch, N.; Descartes, S.; Chromik, R.; Gauvin, R. Microstructure Refinement of Cold-Sprayed Copper Investigated by Electron Channeling Contrast Imaging, *Microsc. Microanal.* 2014, *20*, pp. 1499–1506,
27. Rokni, M.; Widener, C.; Champagne, V. Microstructural Evolution of 6061 Aluminum Gas-Atomized Powder and High-Pressure Cold-Sprayed Deposition, *J. of Thermal Spray Technology* 2014, *23*, pp 514 – 524.
28. King, P.; Zahiri, S.; Jahedi, M., Microstructural Refinement within a Cold-Sprayed Copper, *Metallurgical and Materials Transactions A*, 2009, *40A*, pp. 2115 – 2123.
29. Borchers, C.; Gärtner, F.; Stoltenhoff, T.; Kreye, H. Microstructural bonding features of cold sprayed face centered cubic metals, *Journal of Applied Physics*, 2004, *96*, pp 4288 – 4292.
30. Center for Disease Control Prevention. Electron Micrograph of Methicillin-Resistant *Staphylococcus aureus* (MRSA). 2008, http://faculty.ccbcmd.edu/courses/bio141/lecguide/unit1/shape/EM_MRSA_staph.html
31. Verran, J.; Boyd, R. The Relationship between Substratum Surface Roughness and Microbiological and Organic Soiling: a Review. *Biofouling* .2000, *17*, pp 59-71.